DEVELOPMENT AND EVALUATION OF A
STATIONARY HEAD COMPUTED TOMOGRAPHY SCANNER

Derrek W. Spronk

A dissertation submitted to the faculty at the University of North Carolina Chapel Hill in partial
fulfillment of the requirements for the degree of Doctor of Philosophy in Materials Science in the
Department of Applied Physical Sciences.

Chapel Hill
2021

Approved by:

Otto Zhou

Jianping Lu

Yueh Z. Lee

David Lalush

Jinsong Huang

ABSTRACT

Derrek W. Spronk: Development and Evaluation of a Stationary Head CT Scanner
(Under the direction of Otto Zhou)

X-Ray Computed Tomography (CT) is a widely used 3D imaging technique, proving indispensable in the diagnosis of medical conditions and pathologies. However, virtually all of today's state-of-the-art CT systems rely on a rotating gantry to acquire projections spanning up to 360 degrees around the head and/or body. By replacing the rotating source and detector with a stationary array of x-ray sources and line detectors, a CT scanner could be potentially constructed with a smaller footprint and faster scanning speed. The subject of this dissertation is the design, construction, and evaluation of a stationary head CT (s-HCT) scanner capable of diagnosis of stroke and head trauma patients in limited resource areas such as forward operating bases. By bringing the diagnostic CT scanning capability to the patient, survival rates could potentially be greatly improved through quicker delivery of appropriate treatments.

The scanner is made possible by recent advances in technologies related to CT, including x-ray sensor technology, iterative reconstruction methods, and distributed x-ray sources. Recently, carbon nanotube (CNT) x-ray source arrays have been utilized in a number of medical and security applications. The unique electronic scanning ability afforded by these systems can removes the need for a rotating gantry, producing a stationary system which potentially is more mechanically robust and could provide diagnostic CT images in a smaller footprint, with little to no loss in image quality.

The use of 3 linear x-ray source arrays naturally results in a triangular shape, representing a radical departure from a traditional (circular) source ring. The final construction of the prototype proves that circular objects can still be reconstructed accurately even though the geometry of the system is triangular. Furthermore, the prototype has been able to acquire all of the projection data in scan times comparable to

those of commercial scanners (< 1min), indicating the CNT x-ray and s-HCT technologies are developed enough for clinical trials. As part of an initial evaluation, several objects are imaged in a phantom imaging study, with results demonstrating the temporal and spatial resolution, as well as the accuracy and noise associated with the 3D reconstruction output.

For my daughter, Camilla, and the rest of my devoted and supportive family

ACKNOWLEDGEMENTS

PREFACE

This work is a collection of experiences in the design, construction, and characterization of a stationary CT scanner using multiple x-ray sources. The research is generally focused on the hardware components of such a device, their specifications or geometry, and the effect on image quality. Some evaluation of the hardware components and configuration has been performed in previous publications; the reference to the reproduced writing will be included at the beginning of each chapter.

Of course, the project would not have been possible without an accompanying software package. This critical aspect of the research has been investigated in parallel by my colleague Yueting Luo. For more details on the image processing, please consult her dissertation entitled "Image Reconstruction for Stationary Head CT System with Carbon Nanotube Source Arrays", published in the same year.

TABLE OF CONTENTS

LIST OF TABLES

LIST OF FIGURES

LIST OF ABBREVIATIONS

CBCT   Cone Beam CT

CNT   Carbon Nanotube

CT   Computed Tomography

DBT   Digital Breast Tomosynthesis

DSR   Dynamic Spatial Reconstructor

FOV   Field of View

FSS   Focal Spot Size

IGCT   Inverse Geometry Computed Tomography

HU   Hounsfield Units

HV   High Voltage

HVL   Half Value Layer

MSU   Mobile Stroke Unit

s-CT   Stationary Computed Tomography

s-HCT   Stationary Head Computed Tomography

SDD   Source-Detector Distance

SID   Source-Isocenter Distance

SIRT   Simultaneous Iterative Reconstruction Technique

SNR   Signal-Noise Ratio

TBI   Traumatic Brain Injury

CHAPTER 1: INTRODUCTION

1.1 BACKGROUND

Today's state-of-the-art Computed Tomography (CT) systems rely on a rotating gantry to produce a 360 degree view of the object[1]. Since the third-generation principle was invented in 1976[2], a spinning single source and detector array has persisted in most modern designs. The mechanical stability required for such a design limits its mobility, and the scanning speed will ultimately be limited by the rotation. Modern scanners, which typically rotate at 2-3 Hz, have reached a limit in terms of the sustainable g-force associated with the rotation frequency (Figure 1).
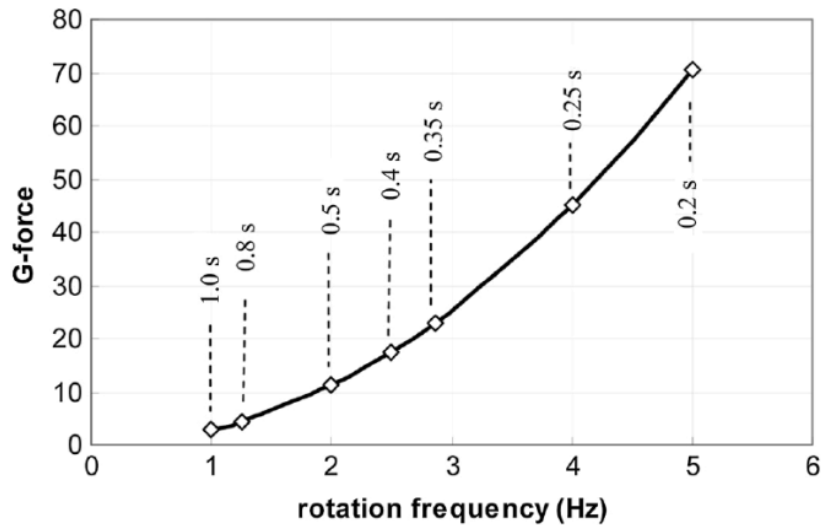
Figure 1: G-force as a function of gantry rotation frequency[1]

Furthermore, the rotating gantry adds a high degree of complexity to the overall system design, and could be eliminated in favor of a configuration of stationary x-ray sources and detectors. While stationary CT systems have yet to see any clinical use, the potential advantages and disadvantages have been weighed for decades[2,3].

Recently, carbon nanotube (CNT) x-ray source arrays have been used in various stationary imaging configurations to generate diagnostic quality tomosynthesis images in the fields of mammography[4], dentistry[5], pulmonology[6], and orthopedics[7]. Featuring source-to-source distances < 1cm, it becomes possible to meet the angular density of views required for CT with distributed CNT sources.

1.2   STATEMENT OF RESEARCH OBJECTIVES

This work describes the concentrated efforts to design, construct, and evaluate a prototype stationary CT system intended for 3D imaging of human heads. The feasibility of such a device was previously demonstrated through simulation[8,9] and experiments[10,11] in a benchtop stationary head CT (s-HCT) configuration utilizing a single CNT source array with 45 focal spots. Based on these results, a system design concept has been generated[12] which collects projection data from 3 identical source-detector imaging planes separated in *z* by only a few cm and rotated by 120° about the *z* axis (Figure 2).
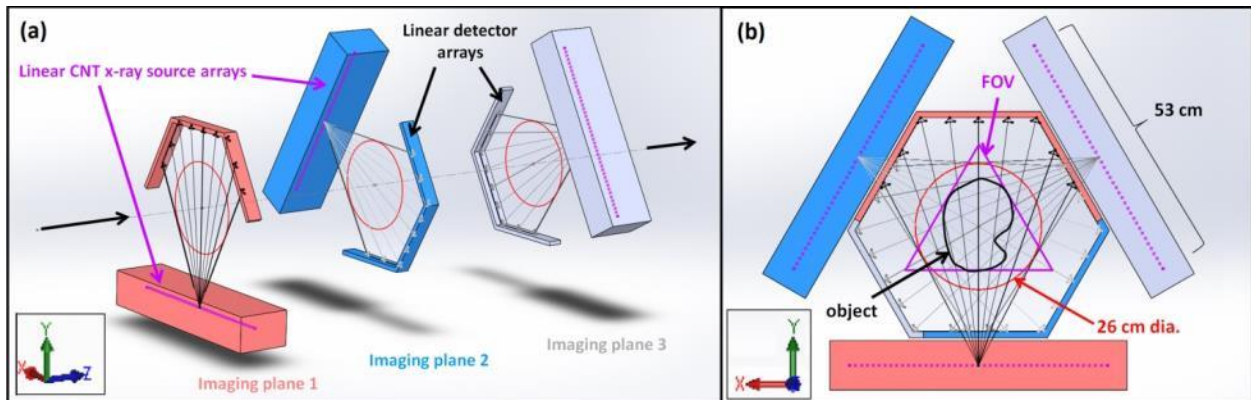
Figure 2: (a) s-HCT system architecture concept. Drawing not to scale in z-axis. (b) Axial view with a triangular field of view (FOV) and the 26 cm diameter head CT requirement superimposed. [12]

The main objective is to construct this system for real-time scanning with no rotation of the object required. This allows for volumetric CT data to be acquired through axial translation of the object in a similar way to that of clinical scanners. Such a system will provide a platform for further experiments in s-CT, including human trials.

1.3 METHODOLOGY

Initial considerations for the design and development of the s-HCT prototype are taken from a review of the literature in the field of medical CT. Specific examples of s-CT have also been identified in the review, identifying the frontier of the research. Once the requirements for the specific application are understood, an evaluation of the components and configuration is presented as a proof-of concept.

The s-HCT concept (Figure 2) is then realized in a laboratory setting using commercially available components. Volumetric object scanning is made possible by translating the object along the z-axis. The resulting 2D projection data are then processed and used as input for simultaneous iterative reconstruction technique (SIRT) in MATLAB. The output 3D image quality is then analyzed and compared to that of a commercial head CT scanner. Finally, various imaging objects (phantoms) are scanned for a few basic measurements of the intrinsic system capabilities in terms of temporal and spatial resolution, as well as CT number accuracy and signal-noise ratio (SNR).

1.4 SCIENTIFIC CONTRIBUTION

This work is a part of the greater effort to realize stationary CT in a clinical setting. While many stationary CT geometries have been simulated and/or emulated, few have been constructed due to the considerable engineering efforts required. Using the results of this research, the fundamental advantages of s-CT can be exploited in future designs to improve temporal resolution as well as system portability. Finally, the design can be refined in numerous ways to fit applications other than head scanning, potentially extending to cardiac CT, image guided radiation therapy, baggage scanning, industrial inspection, or any other 3D imaging scenario.

1.5 DISSERTATION STRUCTURE

This dissertation is organized as follows: Chapter 1 outlines the background and objectives of the research. Chapter 2 gives a literature review of relevant publications to understand the history of CT and CNT distributed x-ray sources, and the fundamental advantages of s-CT. Section 3 presents the feasibility studies performed before construction of the system occurred. Section 4 introduces the

prototype s-HCT system and all of the components. Section 5 contains the experimental results from imaging of various phantoms in an initial attempt to characterize and evaluate the system performance. Section 6 provides some general conclusions from the results, and sets the stage for future research. At the end of the dissertation is a list of references used.

CHAPTER 2: LITERATURE REVIEW

Stationary Computed Tomography (s-CT) is by no means a novel concept. Although many s-CT system designs have been considered, few have been constructed due to the large number of views required and the given size of existing x-ray sources. However, the advent and improvement of related imaging technologies over the last several years has sparked renewed interest in the potential of s-CT. For example, advances in distributed x-ray sources and flat panel detectors have driven the compactness and reliability of the necessary hardware. From the software side, iterative reconstruction methods and general increases in computational speed have made it possible to obtain 3D images with significantly fewer views than before. Because the subject of this dissertation is hardware-oriented, the details of the reconstruction software are kept to a minimum, but the importance of these software advances is not overlooked.

As new technologies emerge, they must be evaluated for use in the intended application. This chapter summarizes the developmental timelines for the CT imaging modality as well as for CNT x-ray source arrays in general. Also some previous examples of s-CT are described. Finally, the clinical motivation for a head-specific s-HCT scanner is presented along with the current state-of-the-art.

Parts of this this chapter have been reproduced from previously published work[12].

2.1 A Brief History of CT

The mathematical basis for CT was first formulated over 100 years ago. Johann Radon is credited with the concept of calculating an object's material distribution using integral values along any number of lines passing through it[13]. While initial applications of Radon theory lied in astronomy[14-16], these efforts led to the first successful implementation by Godfrey Hounsfield[17]. This section provides an introduction to the fundamental CT system architectures.

2.1.1 First-generation

The first CT scanner was invented by Sir Godfrey Hounsfield at EMI Central Research Laboratories in 1971[18]. Two years later, the first CT scanners were installed in the United States. These 'first-generation' machines acquired parallel projection data in a sequential manner (Figure 3), with translation of the x-ray source in addition to rotation. While the image acquisition was tedious, these machines drew heavy attention from the medical field due to the 3D imaging capabilities.
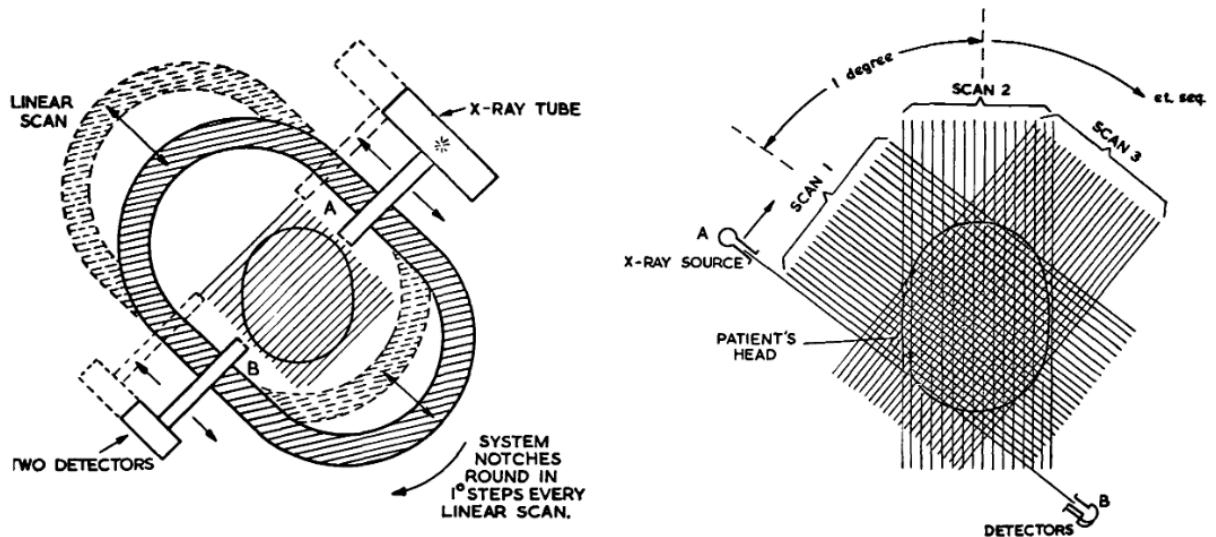
Figure 3: Schematic of the first-generation CT scanner invented by Hounsfield[19].

2.1.2 Second- and Third-generation

First- and second- generation CT architectures required scanning times of roughly 5 minutes for a single slice, requiring an equal amount of time for the patient to be still. After the initial invention of CT scanning, systems were rapidly developed to improve the temporal resolution (Figure 4). This research was driven by a need for shorter scan times. The 'second-generation' machines were improved by increasing the size of the detector to capture more projection data from one x-ray exposure. By 1976, clinical systems featured a fan-beam CT architecture, often referred to as 'third-generation'. By 1980 there were over 10,000 such systems in operation[2].
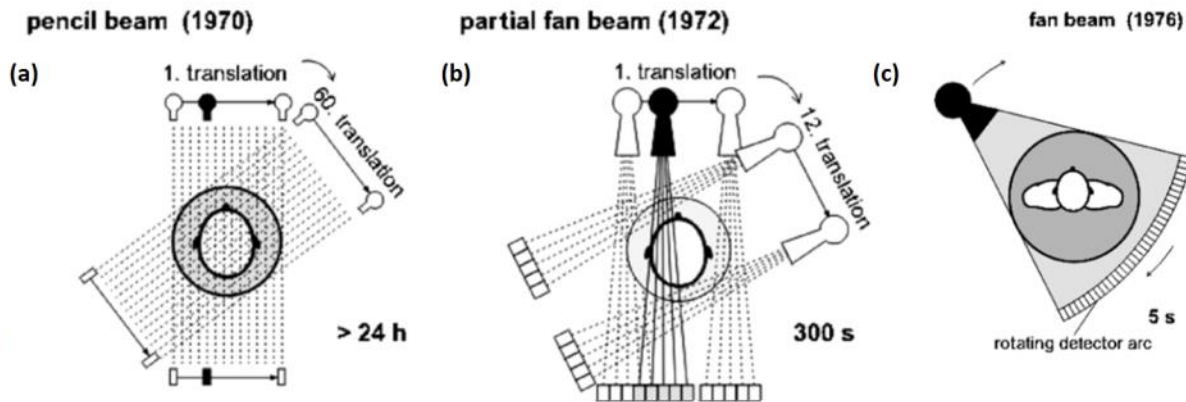
Figure 4: The rapid evolution of CT system design and their temporal resolutions in the early 1970's[2], often referred to as (a) first-, (b) second-, and (c) third- generation architectures.

Many further developments took place to improve upon the third-generation configuration in the following decades. Again, these efforts were driven primarily by a need for faster scanning speeds. For example, slip ring technology was adapted for the unique combination of high voltage and fast data transmission required by CT[20]. Previously the length of the electrical cabling limited scanners to only 1-2 rotations before they needed to reverse direction. The slip ring allowed continuous rotation and helical scanning; by 1992 scanners could acquire full volumes through translation of the patient[2].

X-ray detector technology also progressed significantly in the 1990's, largely thanks to the digital revolution and improved semi-conductor manufacturing[21]. Pixel size eventually became small enough to compete with images on analog material such as film or phosphor screen. Additionally, digital detectors could be tiled or customized to any size, and thus more rows could be acquired from a single x-ray exposure, increasing temporal resolution even more by requiring fewer rotations for a given 3D image volume. At this point, many systems were designed with a cone-shaped x-ray beam to illuminate the whole 2D detector area.

The engineering of CT scanners has also led to the development of some of the most advanced x-ray sources. While scan speed can be increased by adding more detector rows and faster rotation, the temporal resolution eventually becomes limited by the total x-ray dose emitted by the source in one cycle. This presents a need for very high x-ray power which was solved with the introduction of rotating anode technology in 2004[22]. With the improved heat management, modern x-ray tubes can operate at 100 kW or higher. This important advancement brought the temporal resolution to < 1 second.

2.1.3 Next-generation: Multi-source CT

Despite the previously mentioned hardware improvements, it is interesting to note that the third-generation architecture persists since its introduction, and a majority of clinical scanners still operate using a single rotating source. While detector technology evolved to gather more pixels with one exposure, the source became more sophisticated to increase the quality of that one exposure. As a result, x-ray sources are so large that it is not very practical to use more than one of them on a spinning system. Nevertheless, dual-source CT was first implemented in 2006 with a gantry speed of 3 Hz[23] and a temporal resolution of 83 ms when both tubes are operated at the same kVp. This type of scanner is also capable of spectral CT when the tubes are set to two different kVp values. Dual-source scanners are in use today in many hospitals, and are considered state-of-the-art when it comes to the most demanding CT imaging tasks.
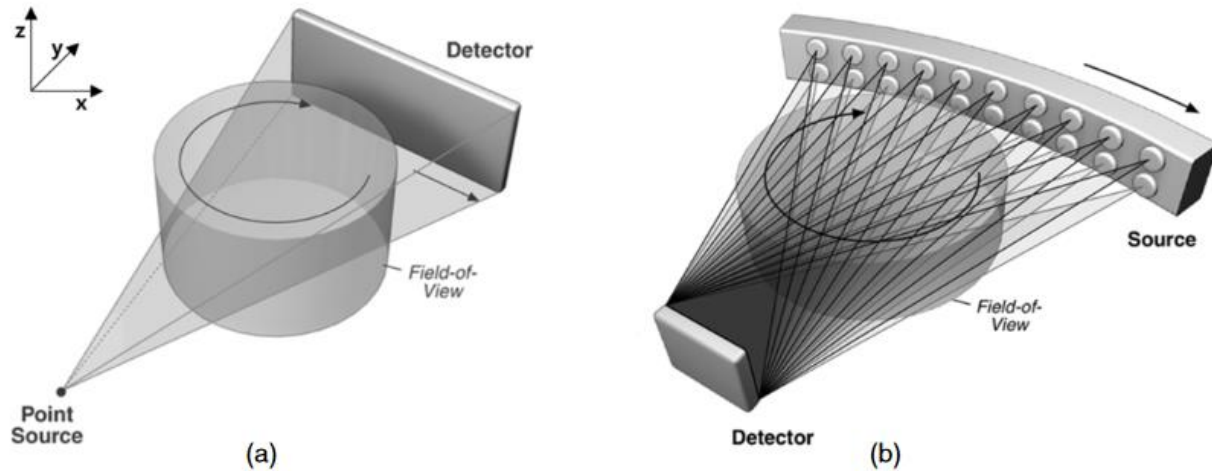
Figure 5: (a) Typical scanning configuration for single-source third-generation CT. (b) Distributed x-ray sources can be used for a concept (still based on rotation) known as inverse geometry CT (IGCT)[24]

It seems natural that adding even more x-ray sources to the gantry would yield even higher temporal resolution. Recent studies in CT architectures[25,26] have suggested that adding more than 2 or 3 x-ray sources is impractical given the size of existing components. It follows that the "next-generation" of CT configurations may depend on further development of distributed x-ray sources[27]. Described in more detail in section 2.1.5, these unique devices are typically customized to their application. For example, a system with 8 x-ray sources has been demonstrated in a novel concept known as inverse geometry CT (IGCT)[28] (Figure 5b). This research is an attempt to resolve issues with object-based scatter common in cone-beam CT (CBCT) scanners. Although this work is part of the frontier of research in multi-source CT, it still relies on the principle of rotation.

2.1.4   Stationary CT (s-CT)

One factor inhibiting the mobility of CT systems is the rotating gantry, which requires substantial counterweighting and steady anchoring for smooth operation. Combined with the high voltage slip ring system, this bulky collection of components requires consistent routine maintenance[29], and could be rendered unnecessary by a fixed array of x-ray sources and linear detectors. By removing the need for a rotating gantry, a stationary system potentially is more mechanically robust and could provide diagnostic CT images in a smaller footprint, with little to no loss in image quality. However, the stationary concept is difficult to realize with conventional tubes due to the excessively bulky housing and cooling peripherals they typically come with.
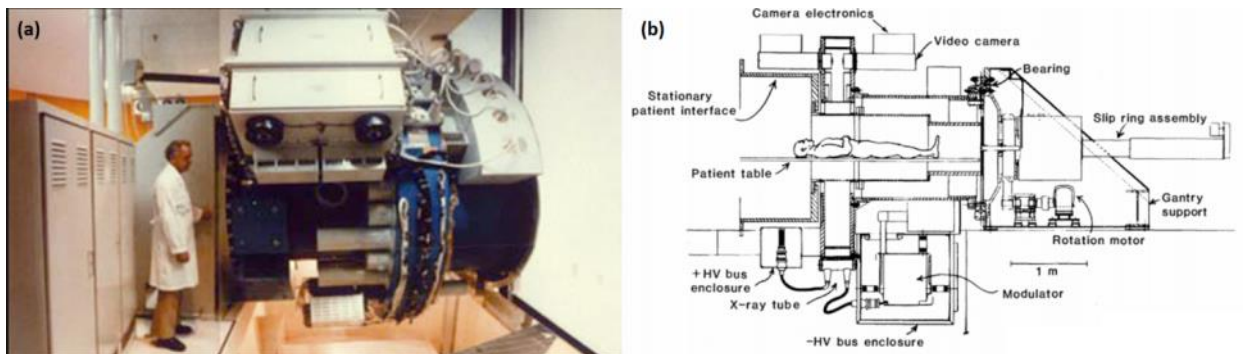
Figure 6: (a)Photo of one of the first multi-source CT prototypes, known as the Dynamic Spatial Reconstructor (DSR)[30]. (b) The DSR system schematic viewed from the sagittal plane.

The first attempt was a semi-stationary system known as the Dynamic Spatial Reconstructor (DSR)(Figure 6), combining 14 x-ray tubes and 14 image intensifiers on a rotating gantry[30]. While still relying on the principle of mechanical rotation, this machine was the first to demonstrate acquisition of CT projection data from multiple x-ray sources fired in sequence. One of the first fully stationary CT scanners was created for dynamic cardiac CT imaging in 1982[31], relying on a steered electron beam. This scanner directed the electron beam to change the focal spot position on an enlarged anode with the temporal precision necessary to acquire 20 reconstructed frames per second.

While this original concept was limited in terms of axial scanning range and overall size, the deflection coil technology has been used in smaller tubes that could potentially be arranged in a circular

pattern[32]. Though research suggests that scanned x-ray sources can produce comparable image quality to that of gantry-based systems[33], the technology has not become developed enough for widespread deployment in a clinical setting. The principle of electron beam steering has also been used in unique semi-stationary geometries[34,35] for the purpose of overcoming various fundamental limits of rotation-based CT.

2.1.5   Distributed X-ray Sources

More modern examples of distributed source technology are already in existence, consisting of multiple focal spots contained within one vacuum chamber, all designed for specific applications. In these complex devices, the high voltage anode is held at a fixed kVp and the electron source must be precisely gated in order for each x-ray source to be operated independently of the others. This has led to the development of a variety of electron sources for x-ray generation, such as carbon nanotube (CNT) based field emitters[36], tungsten dispenser cathodes[37], and Spindt type emitters [38]. Recently, spatially distributed x-ray source array technology with CNT field emitters has been demonstrated for a variety of 3D imaging applications[4-6,39]. Featuring source-to-source distances as low as 4 mm, these unique switching x-ray systems are well-suited to provide the necessary angular resolution for CT imaging. In this study we will assess the feasibility of using CNT source arrays for a fully stationary CT system designed for head imaging.

2.2   A Brief History of CNT Distributed X-ray Source Arrays

This section gives a brief timeline of the research in CNT x-ray cathodes from the initial invention to the sophisticated multi-source arrays in production today.

2.2.1   Initial invention

Carbon nanotubes (CNTs), part of the fullerene family, are hollow cylindrical structures made of graphite sheets with diameters ranging from < 1 nm to tens of nm. Ever since the discovery of this unique material in 1993[40], CNTs have found numerous applications such as electronic devices, sensors, drug

delivery, energy storage devices, crypto primitives and tissue engineering[41]. The high aspect ratio of the molecules also makes them ideal for field emission, capable of high current density in excess of 1 A/cm^2 [42]. After the high electron beam current density was demonstrated in vacuum, it didn't take long for CNTs to be used as an electron source in the production of x-rays[43].

Polychromatic (Brehmsstrahlung) x-ray radiation, discovered by Roentgen in the late 19th century[44], is created by accelerating free electrons in vacuum across a potential difference of several kV and bombarding a metal target (anode)[45]. Depending on the material, several characteristic x-ray wavelengths are also emitted. Traditionally, the electron beam in x-ray sources is emitted from a thermionic wire (cathode) that is resistively heated to over 1000° C. These mechanisms are still the underlying physical principles used in commercial x-ray tubes over 100 years after the initial invention of the Coolidge tube in 1913[46]. However, this design has several inherent limitations: high power consumption, high temperature operation, and slow response time.

The advantages of field emission cathodes over filament-based cathodes were recognized soon after their invention. The electrons are emitted at room temperature and the output current is easily and predictably adjusted with the input voltage[47]. Initial attempts at X-ray production with field emission cathodes in diode mode used micro-fabricated metal tips[48] with poor lifetime and only μA of current[49,50]. These "Spindt"[51] emitters have since become more robust through improvement of μ-fabrication methods[52], but research has tapered off in favor of other candidates such as ZnO nanowires[53].

CNTs are another attractive candidate for field emission; their use in x-ray sources roughly followed a similar research timeline as Spindt emitters. Through optimization of deposition techniques, macroscopic CNT cathodes were developed for use in x-ray tubes in the early 2000's with great success[36,54-56]. In the following years, CNT x-ray sources were developed for a wide variety of imaging applications with the help of industry partners. Some examples are described in the following sub-sections.

2.2.2   CNT μ-CT System

One of the first complete X-ray imaging systems to use a CNT field mission cathode was a rotating single-source CT system for the imaging of internal structures of small animals (mice) for biomedical research [57]. While the slow gantry and single-source nature of the CNT μ-CT system resulted in long acquisition times, a major advantage of CNT cathodes was demonstrated through respiratory gating[58] Furthermore, four-dimensional cardiac images of live mice were demonstrated with high spatial resolution[59]. These experiments provided the confidence necessary to proceed with the development distributed CNT x-ray source arrays.

2.2.3   Tomosynthesis

Many medical imaging applications can be achieved with standard 2D radiography, which consists of only one x-ray exposure. For 3D images, many exposures must be taken as in CT. In the interest of saving radiation dose to the patient, a technique has been developed known as limited-angle tomography, or tomosynthesis[60]. This method was first introduced in medical imaging around the same time as CT; however, poor-quality image detectors prevented tomosynthesis from becoming mainstream until the advent of digital detector technology in the 1990's[61]. Since then, Digital Breast Tomosynthesis (DBT) devices have flooded the market and became the go-to modality for mammography cancer screening.
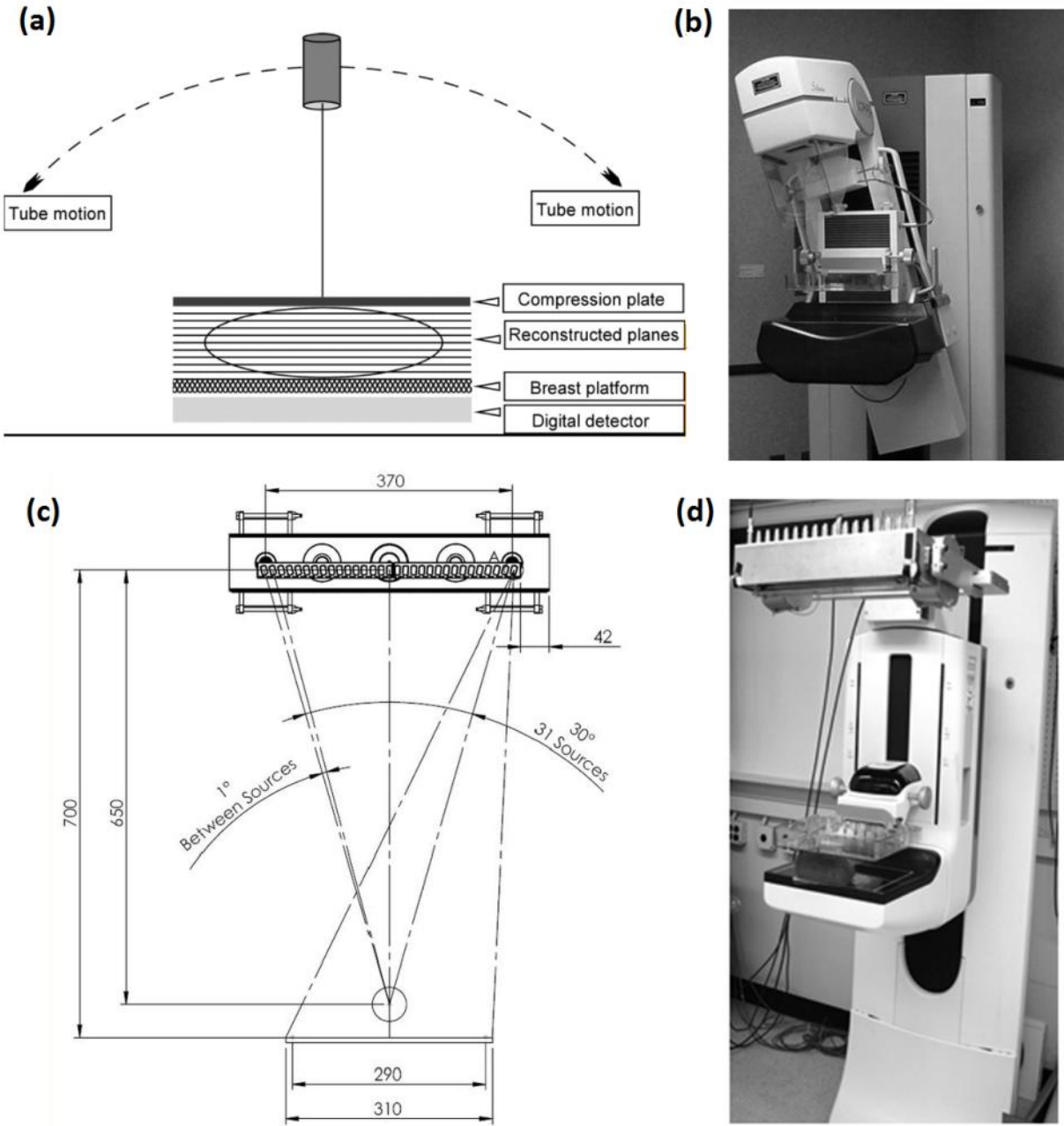
Figure 7: (a) Moving-source architecture for modern DBT systems[62] (b)Photograph of a moving-source DBT system[62] (c)Multiple focal spots on a shared anode can achieve the same angular range with no motion blur[4] (d) Photograph of a stationary DBT system[4]

Similar to CT, virtually all clinical DBT scanners use a single x-ray source rotating around an isocenter (Figure 7a). The ability to pattern CNT depositions on substrates and assemble them closely together allows for a drastic improvement in temporal resolution, and subsequently a reduction in the total

scanning time. For any medical imaging application, the total scanning time should be as brief as possible to minimize the blurring through patient motion. The clinical trials for the prototype s-DBT system produced comparable image quality with short scan times, effectively demonstrating the temporal resolution improvement afforded by distributed x-ray source arrays.

2.2.4 Stationary CT with CNT X-ray Sources

Many of the previously mentioned studies on field-emission based x-ray sources were limited in terms of the peak x-ray energy used. While the current-producing capabilities of the emitters are important, the ultimate usefulness of the x-rays depends on the voltage of the anode. For example, small objects such as mice and human extremities can be imaged with 40 or 50 kVp, but applications such as CT have much higher energy requirements in excess of 100 kVp. One of the first distributed x-ray source arrays using CNT cathodes (Figure 20a) was built for a s-CT concept, but suffered from lifetime issues under high voltage (HV) operation. More recently, CNT cathodes have been proven to produce reliable current in HV applications in excess of 120 kVp[63], making them a candidate for CT. For example, linear CNT x-ray source arrays operating at 160 kVp have been used in a rectangular configuration to produce 3D images of luggage phantoms for airport security screening[39].

Now that distributed x-ray source technology has been further refined and developed, it is possible to bring stationary CT from concept to prototype. This hardware change seems natural given the previous evolution of the third generation (fan-beam) architecture described in Section 2.1.2 In this transition, image acquisition speed was greatly increased with a hardware solution (multiple detector pixels) to eliminate the need for translation in addition to rotation. Similarly, further speed gains could be possible with a hardware solution involving multiple sources. This is supported by a large uptick in s-CT configurational studies in recent years. More examples are introduced in Section 3.3.1 as part of the research in system design.

2.3 Clinical Motivation for s-HCT

There exists a demand in resource-deprived environments such as military Forward Operating Bases and ambulances for a mobile, mechanically stable CT imaging system which can provide adequate diagnostic images for patients suffering head trauma or stroke[64,65]. However, there are also many additional reasons to pursue s-CT research and usher in the next-generation of machines. This section describes the present day clinical motivation for a head-specific s-HCT scanner, and also highlights some of the major advantages afforded by multi-source stationary CT in all applications.

2.3.1 Portability

Today's leading CT systems are mechanically complex instruments, built upon the principle of gantry rotation. Commonly a single x-ray source and detector pair are spun around the object at speeds up to 3 Hz. The resulting centrifugal forces will ultimately limit the scanning speed of such systems. Expensive operating costs, high maintenance requirements, and overall weight are some additional reasons why rotation-based CT systems are mostly used in hospitals or clinics with appropriate infrastructure. Consequently, a vast majority of patients suffering from acute stroke or head trauma must be quickly transported to appropriate facilities before being diagnosed and treated, introducing a delay which can cause additional morbidity or mortality. By bringing the diagnostic CT scanning capability to the patient, survival rates could potentially be greatly improved through quicker delivery of appropriate treatments[66].

Efforts have been made to mobilize CT technology specifically for head imaging[65]; naturally, a reduction in the physical size of these machines is necessary in order to realize this concept. Conveniently, CT imaging of the brain for diagnosis of stroke and trauma victims requires a smaller field of view (FOV) than full body systems, enabling the design of smaller CT scanners for this particular application. Instruments such as the CereTom (Neurologica, Danvers, MA, USA), the TomoScan (Philips Medical Systems, Best, the Netherlands), and the xCAT ENT (Xoran Technologies, Ann Arbor, MI, USA), have radically altered EMS strategy when responding to stroke victims. Not only is physical

footprint of these scanners smaller than that of full body scanners, but also the reduced source-detector distance (SDD) places less demand on the x-ray source itself, allowing for lower mAs values to be used. This greatly reduces the power consumption, further encouraging mobility by enabling the use of stand-alone power supplies. The first successful Mobile Stroke Unit (MSU) was reported in 2010, featuring a Philips TomoScan installed in the back of an ambulance[67]. These trials produced a call-to-therapy time of 35 minutes, faster than the >60 minutes required for conventional clinical care. A similar result was achieved in 2013 with the Neurologica CereTom[68], showing significant reduction in time to treatment compared to a control group. Other studies have demonstrated improvement of triage in stroke patients and a reduction in wasted resources with a mobile CT scanner[29].

On average, every day the United States alone reports over 2000 incidents of ischemic stroke[69], over 350 stroke-related deaths,[69] and over 150 deaths caused by TBI[70]. While the MSU shows promising results for field diagnosis, recent studies have shown that portable CT has many benefits within the hospital infrastructure as well[71]. The transport of critically ill patients through the hospital to the CT room introduces risk of additional morbidity[72]. In cases of ischemic stroke, diagnosis and administration of anti-coagulants can be faster with a scanner in the patient's room[73]. Furthermore, bedside imaging takes the guesswork out of intracranial catheter placement[74].

2.3.2   Image Acquisition Speed

Because of the potential advantages, s-CT remains an active field of research even 40 years after the invention of some of the first stationary (or semi-stationary) scanners.[31,75] These early prototypes were developed in the interest of increasing temporal resolution, specifically for cardiac CT. Despite numerous efforts, the ability to obtain accurate 3D images of the heart with remains one of the major challenges in x-ray imaging[76]. Third-generation CT relies on rapid rotation of a single source detector pair to acquire all views (or rotation of the object as in industrial inspection scanners). Because the heart is constantly moving, all of these views must be obtained in a period of < 50 ms for a reconstruction rate of 20 frames per second (fps). As a result, all projections must be acquired sequentially, and the frame

rate of even the most high-powered systems is limited by the gantry speed (< 4 rotations per second)[1]. The use of a limited angular span in the reconstruction can allow for temporal resolution of 125 ms to be achieved by state-of-the-art single source systems[25]. By adding an extra source-detector pair to the gantry, the dual-source CT design[77] can improve the imaging acquisition time two-fold (~60 ms). Fitzgerald et al. [26] propose that the addition of a third source can achieve the 50 ms goal, but adding more x-ray sources and detectors to the rotating gantry reaches a practical limit given the size, weight, and cost of the components.

If the rotational aspect can be removed, the maximum achievable temporal resolution for CT scanning in a stationary system is only limited by the large number of views required. Over the last few years, several multi-source s-CT system architectures have been proposed[78-83], with simulated data suggesting that 3D imaging with high temporal resolution is feasible. All of these examples provide image data specialized for their application while using much fewer than the ~1000 views required for traditional CT. Depending on the application, if the number of views required for diagnostic images can be reduced, it follows that the reconstructed frame rate can be increased. This has led to a wealth of research in sparse-view CT through iterative reconstruction and deep learning algorithms[84-86]. However, rotating CT systems cannot take advantage of sparse-view approaches because the image acquisition time depends on the rotation rate which has a practical engineering constraint. One way to realize faster 3D imaging through few-view reconstruction is to use stationary sources and detectors.

The security screening of luggage in airports has been another proponent of development in sparse-view, quasi-3D x-ray imaging. Due to the high throughput demands of this particular application, image acquisition speed is highly valued. In one example, advanced deep learning algorithms are used with a medical CT to produce reconstruction of luggage objects with only 9 views[87]. In another study, Moser et al. demonstrated a functional s-CT system with only 6 views and sub-ms 3D images in a ballistics application[88]. This presents another fundamental advantage of s-CT: multiple source-detector pairs can be operated simultaneously to collect all views in even less time. However, simultaneous imaging requires careful consideration to the effects of object based scatter. In certain systems, this issue can be

averted through collimation to minimize the cross-talk between sources and peripheral detectors; this concept is explored further in Section 5.6.1.

2.3.3 Other Advantages

Generally speaking, the motivation for s-CT is driven by a need for a mechanically simpler machine. By removing the rotational aspect from the system architecture in favor of a fixed configuration of x-ray sources and detectors, the electrical connections become simpler, no slip ring is required, and the operational overhead and maintenance requirements can be greatly reduced. Furthermore, reduction of the number of views is correlated with lower x-ray exposure to the imaging object.
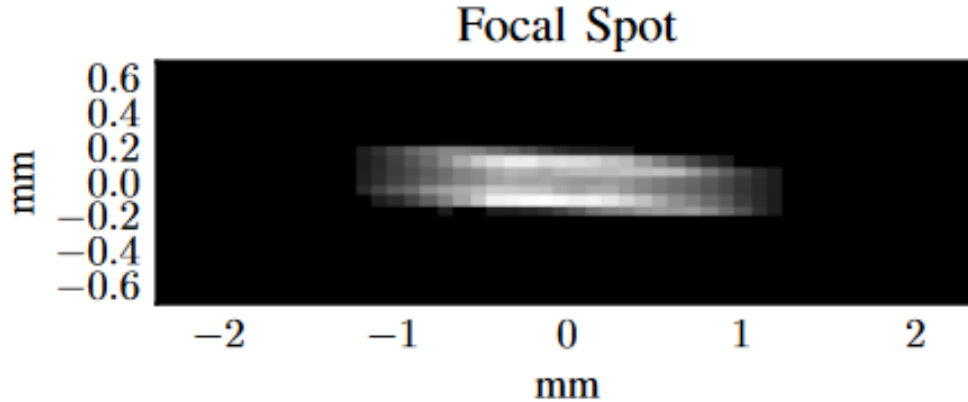
Figure 8: Simulated magnitude of focal spot blurring based on a pinhole image of a stationary focal spot with nominal size 0.6 mm[89]

A final characteristic of s-CT that may be obvious but is worth noting: the focal spots are not subjected to motion blur. The magnitude of the focal spot blurring in gantry-based systems has been investigated thoroughly[89], and depends on multiple factors including the gantry rotation speed, x-ray exposure time, and the system source-isocenter distance (SID), but is estimated on the order of ~0.2 mm. Although this effect is small compared to the scale of patient motion and the typical image resolution of 0.5 mm, the orientation dependence of the spatial resolution is detectable in super high resolution (SHR) scanners[90]. Reduction of motion blur in cardiac imaging has also been the motivation driving the design of inverse geometry multisource x-ray imaging systems[91].

2.4   Summary

Despite numerous advances in hardware, third-generation CT scanners have dominated the market for over 40 years. The inclusion of a constantly moving x-ray source coupled with a need for high power and rapid image acquisition have resulted in complex, bulky machines with limited accessibility. Efforts have been made to improve the temporal resolution possible with third-gen architecture by adding more sources, which quickly reaches a practical limit. Previous studies with CNT distributed x-ray source arrays have demonstrated the benefits of stationary medical imaging applications; it remains to be proven if this technology can be used for medical CT as well.

The proposed system is stationary in two senses: multi-view eliminates need for rotating gantry, and also power requirements are low enough in this unique application that the rotating anode can be replaced with a stationary tungsten target. The next step is to evaluate if an existing CNT x-ray source array can be used to generate useful 3D images.

CHAPTER 3: EVALUATION OF LINEAR CNT X-RAY SOURCE ARRAY AND NON-CIRCULAR CT GEOMETRY

CNT x-ray source arrays have demonstrated excellent imaging capability in tomosynthesis and μ-CT applications, and have long been considered a viable candidate for use in multi-source CT. However, the use of a linear anode makes it difficult to adapt this technology to the CT imaging modality without a complete redesign of the architecture. Furthermore, while the CNT cathodes can produce adequate current, the ultimate power of these systems is currently limited by the melting temperature of the anode. In single-focal spot x-ray sources, the excess heat is managed through rapid rotation of the anode, but this is also a difficult concept to duplicate with multi-source arrays. Rotating rod anodes have emerged as one natural solution to this problem, but development is still in the early stages[92].

The subject of this chapter concerns the feasibility of using an existing CNT x-ray source array with a passively cooled linear anode for the specific application of head CT imaging. First, the requirements are determined by examination of an existing third-generation CT system designed for bedside head imaging (CereTom). Next, the CNT x-ray sources are characterized in three areas: focal spot size (FSS), beam quality, and total dose output. Finally, some consideration is given to the arrangement of multiple source arrays for optimal CT geometry. Additional research has been performed through simulation[8,9] to help inform the decision. In an experimental benchtop setup, a single array is used with rotation of the object to emulate the proposed geometry in order to determine if s-HCT is possible with the selected components.

Parts of this this chapter have been reproduced from previously published works[10,12].

3.1 Requirements

Before the s-HCT system can be built, careful consideration must be given to the target specifications of the device. In the proposed scanner, the major fundamental change is the replacement of the x-ray source. Therefore, it must be confirmed that the new source can meet the requirements for head CT.

3.1.1 Existing Commercial System

A major goal of the present study is to demonstrate real-time CT scanning of head-sized objects with multiple CNT x-ray source arrays. In order to determine the specifications required of such a device, a commercial system must be selected to use as a benchmark. The CereTom (Figure 9) is a rotation based portable CT imaging system sized exclusively for head imaging. It has demonstrated diagnostic capability both within and outside the hospital setting, with NeuroLogica providing a machine at National Football League games, the Indy 500, and a professional boxing match, where its use helped to diagnose a post-fight subdural hematoma[65].
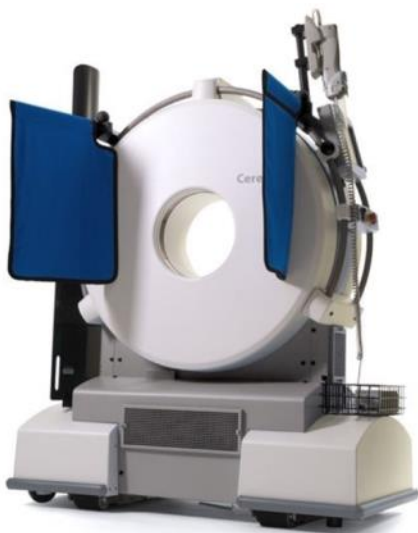
Rotation time	2s
Gantry speed:	30 rpm
Typical scan range:	25 cm
Scan time:	2 s
Scan cycle time:	3 s
Slice thickness:	2.5 mm
Number of slices per scan	4
Z scan widths at ISO-center:	10 mm
Image reconstruction time:	1s/image
X-ray beam shape:	Cone Beam
X-ray tube voltage:	100, 120, 140 kV
X-ray tube current:	7.5 and 3.75 mA
X-ray tube cooling time:	12 minutes max
Focal spot size:	1 mm x 1 mm
X-Ray Tube Type	Fixed Anode

Figure 9: The Neurologica Ceretom will be used as a benchmark for comparison to the s-HCT system. Relevant specifications from the brochure are listed[93].

3.1.2   Focal Spot Size

The FSS must be sufficiently small to allow for a high degree of spatial resolution. Smaller FSS has been shown to produce sharper images[94] and reduce beam hardening artifacts from calcifications in CT reconstruction[95], but at the expense of reduced x-ray tube current and longer imaging time due to limitations of the metal anode thermal management. Typical x-ray sources used in CT machines have an IEC 1,0 FSS (including the CereTom), but this does not take into account the enlargement of the effective FSS in the direction of rotation caused by tube motion during exposure. The stationary CT design offers a fundamental advantage in that there is no FSS blurring due to source motion. The magnitude of the FSS blurring in gantry-based systems depends on multiple factors including the gantry rotation speed, x-ray exposure time, and the system SID, but is estimated on the order of 0.2 mm. It should be noted that this effect is negligible compared to blurring caused by patient motion.
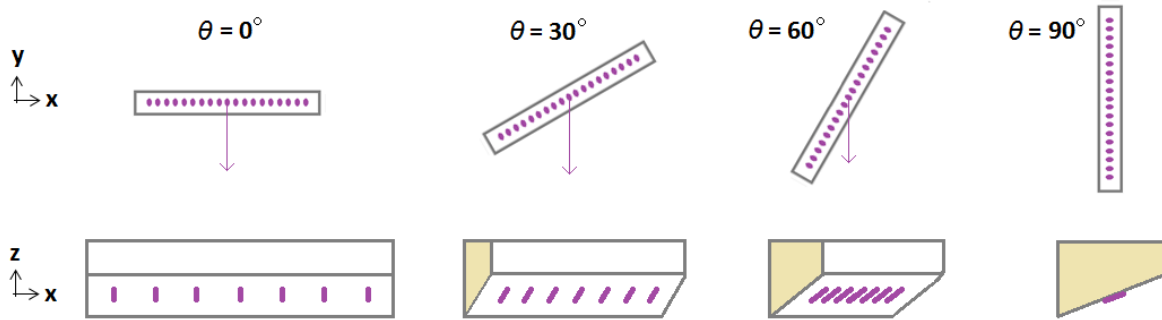
Figure 10: Illustration of enlargement of the FSS depending on viewing angle.

As another consideration, the CNT x-ray source array used in the present study has a common and flat anode. At such the sources at extreme ends of the array can be expected to have an enlargement in the effective focal spot width due to the geometry of the anode. When viewing an individual focal spot, the forward angle of the high voltage anode produces a slanted shape that makes the effective FSS wider at higher fan-beam angles (Figure 10).

3.1.3 Beam quality

The output spectrum and resulting average energy must be sufficiently high to penetrate the skull and reduce low energy dosage which will not reach the detectors. 120 kVp is the typical peak energy used for brain imaging. The average energy will depend on the inherent filtration of the tube window. Existing CT systems were examined to determine an appropriate HVL value to use in this application. On average, the surveyed systems reported a HVL of 7.4 [96,97].

3.1.4 Density of Views

The focal spot pitch must be small enough to provide suitable angular resolution. While most rotating CT scanners use over 1000 views over 360°, successful reconstruction has been demonstrated with as few as 90 views[98]. The s-HCT system configuration will feature a number of views somewhere in between, depending on the number of source arrays. More on the angular density of views is presented in Section 4.1.

3.2 CNT Distributed X-ray Source Array
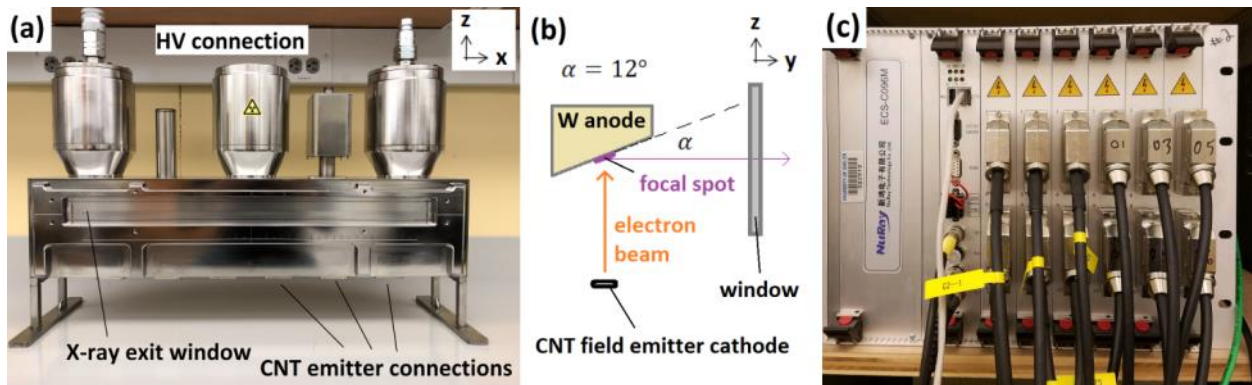
Figure 11: (a) Photograph of the CNT x-ray source array. The HV connection services a stationary tungsten target (oil-cooled model pictured) with anode angle α = 12°. (b) The geometrical relationship between the target and the CNT field emitter cathode. (c) Electronic Control System (ECS) included as part of the CNT x-ray imaging system.

The CNT source array (XinRay Systems Inc., Research Triangle Park, NC) is a prototype consisting of 45 individually addressable x-ray focal spots enabled by an array of gated CNT field emission cathodes. All focal spots are collinearly positioned along a continuous elongated tungsten

target, with a center-to-center distance of 12 mm and a total length of 528 mm. A picture of the array is shown in Figure 11a. The source can be operated at a maximum energy of 160 kVp. The anode voltage is supplied by a Spellman XRV Generator, programmed to hold a fixed voltage of the user's choice. The internal vacuum is maintained below 1×10^{-8} Torr by an ion pump connected to the x-ray source housing. The x-ray exit window is composed of stainless steel with a thickness of 0.2 mm. The system includes a switchable Electronic Control System (ECS) (also supplied by XinRay Systems Inc.) (shown in Figure 11c) to provide the automatically adjustable bias extraction voltage to each CNT emitter gate to maintain the constant output with high temporal precision. The source array was mounted on an optical table with custom machined aluminum hardware. All measurements were taken in the *x-y* plane, using the measured height off the surface of the table as a planar reference. The source array was installed with the center mark above a pivot point, about which the various measurement sensors were rotated on a rigid mounting plate. All angles were measured to within ± 0.5° with an angle ruler.

3.2.1   Focal Spot Size (FSS) Measurement

The FSS of all 45 beams was measured according to the European Standard (EN 12543-2) using a magnified pinhole method. The anode voltage was 120 kVp, with each cathode operating at 15 mA (~12 mA anode current), and 1.0 ms exposure time. Figure 12a shows a diagram of the experimental setup. The diameter of the pinhole is 100 μm, machined into a tungsten disk 2 mm thick. The images were taken with a magnification factor of 3.8. The flat panel detector (Teledyne Xineos 2301) used to record the magnified focal spot image has a pixel size of 0.099 x 0.099 mm^2. To measure the change in effective FSS with viewing angle, the pinhole and detector apparatus was rotated about an axis centered on the central focal spot (#23). These measurements are taken with regard to fan-beam angle only, meaning all measurements take place in the *x-y* (axial) plane with no variation in cone-angle. Due to the forward angle geometry of the anode (Figure 11b), the focal spot width is expected to increase with θ.
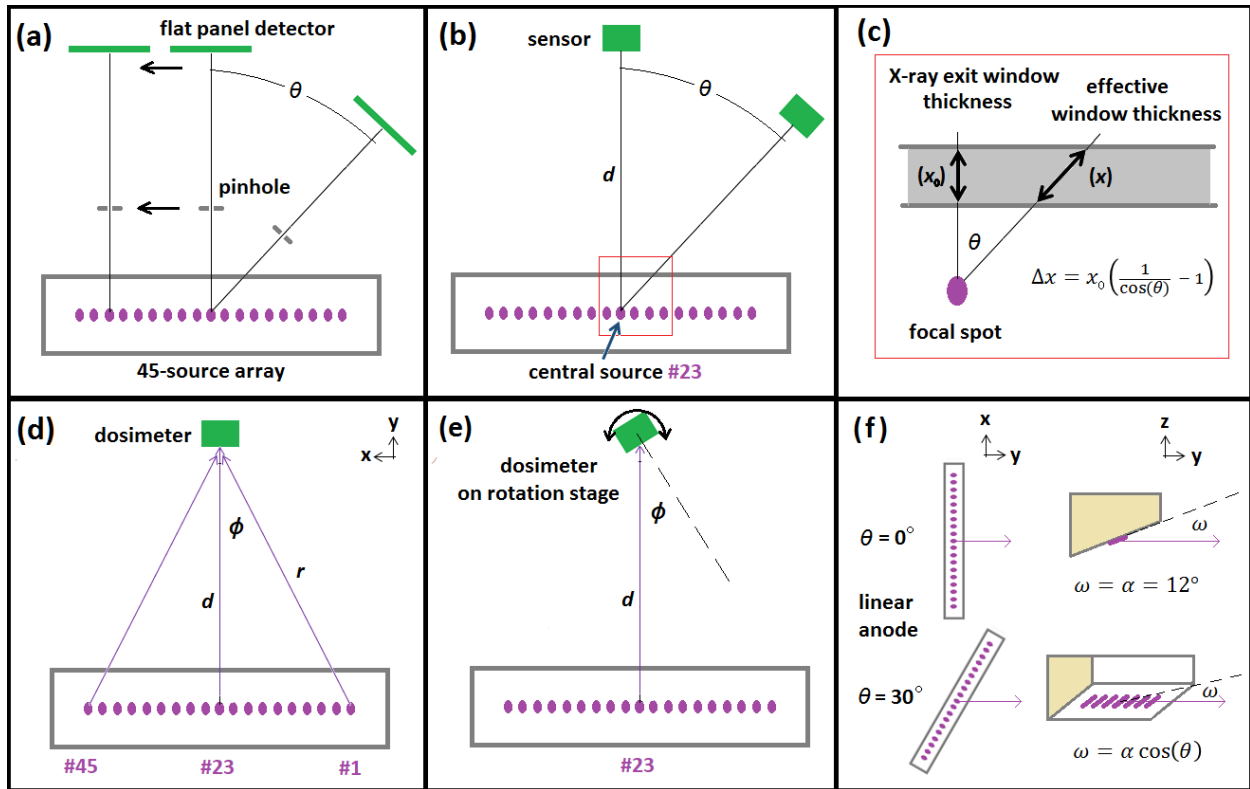
Figure 12: (a) Diagram of testing setup used for measurement of FSS. The detector-pinhole apparatus was translated in 12 mm steps to obtain a 0° viewing angle for each of the 45 focal spots. (b) Source #23 was used for measurement of FSS, HVL, and energy spectrum as a function of exit angle θ. (c) Red square inset from (b), defining effective window thickness as a function of θ. (d) Diagram of testing setup used for x-ray exposure measurement from all sources in one scan. (e) Diagram of testing setup used for characterization of the dosimeter response as a function of sensor incident angle ϕ. (f) Illustration of the anode angulation effect on the resulting heel angle ω.
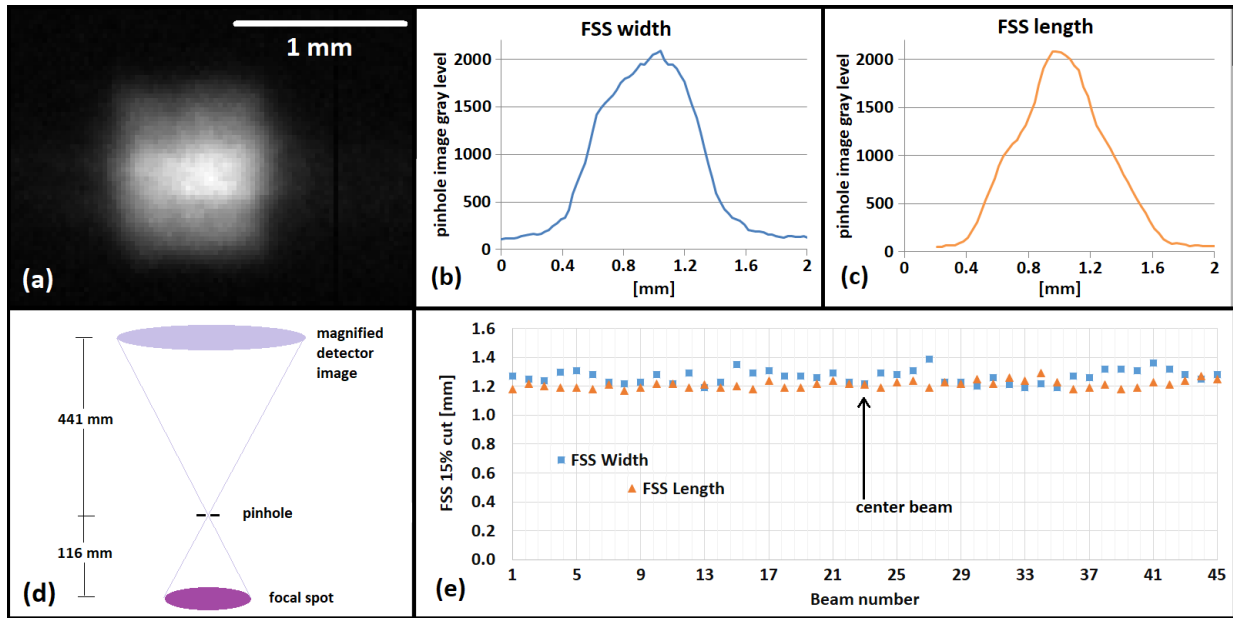
Figure 13: (a) Pinhole image of the central beam of the CNT x-ray source array (100 μm pinhole, 3.8 magnification). (b) Horizontal and (c) vertical cuts of the pinhole image give the FSS of 1.23 x 1.21 mm (width x length). (d) FSS experimental diagram. (e) Width and length values for all focal spots.

The pinhole image of the central beam (source 23) is shown in Figure 13a. 5 rows and 5 columns were averaged to generate the horizontal (width) and vertical (length) profiles. With an effective image pixel size of 0.026 x 0.026 mm2, the width and length at 15% of the maximum intensity are measured to be 1.23 mm and 1.21 mm, respectively. The same measurement on all 45 beams (Figure 13e) resulted in an average FSS of 1.26 (± 0.04) mm × 1.21 (± 0.03) mm. This is equivalent to IEC value of 1,0.
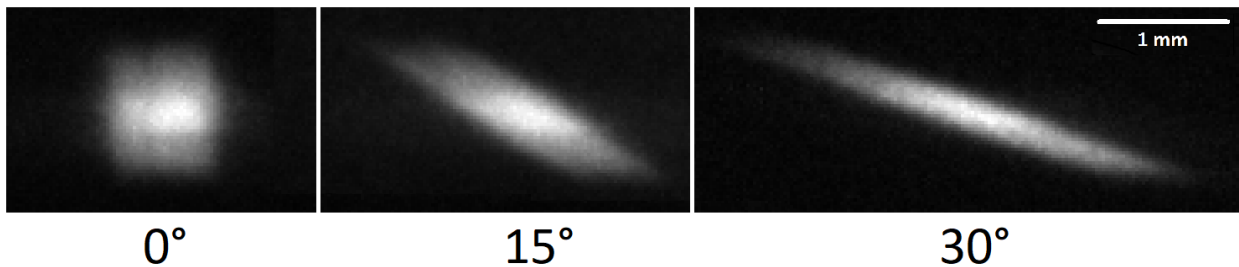
Figure 14: Pinhole images of the central beam of the CNT x-ray source array, as seen from the given viewing angle.

The pinhole-detector apparatus was pivoted about the central source to acquire images of the focal spot from viewing angles 0°, 15°, and 30°, displayed in Figure 14. The magnification was constant for

each image. While the length remains constant, the width increases from 1.23 mm to 1.5 mm at 15°, and 2.0 mm at 30°. These width values are estimated using an average of all rows in the dark-corrected pinhole images.

These extreme end measurements conform to IEC 1,7 within a total fan-beam angle of 60 degrees. This is not a fundamental issue of the CNT source array technology, but rather a limitation of the angular anode design which has been studied and corrected for in rotation based CT[99]. For more sensitive applications, the issue can be mitigated by rotating the individual anodes towards the isocenter of the system, as, for example, in the array designed for the s-DBT device[4].

3.2.2   Filtration, Spectrum and Half Value Layer (HVL) Measurement

The inherent filtration of any x-ray source is determined initially by the exit window material. For many medical applications, a low-Z material such as aluminum or beryllium is typically chosen. The x-ray exit window material in this particular CNT source array is stainless steel, which will result in a comparatively harder beam and higher average energy. Given the geometry of this source array, the effective thickness of the window along the beam path will also vary with fan-beam angle (θ), adding filtration and thus increasing HVL for wide viewing angles (Figure 12c). For example, when viewed from an angle of 60° (the most extreme case for a 120° fan-angle), the effective window thickness increases from 0.20 to 0.40 mm. This added filtration along with the variation in SID will change the effective dose per projection.   To characterize the effects of the added filtration, a dosimeter (RaySafe X2, Unfors RaySafe AB, Sweden, manufacturer calibrated) with a built-in solid state multisensor was used to evaluate the HVL of the central source (#23) at a distance of 50 cm. As with the FSS measurement, a range of viewing angles was included to investigate the increase in HVL (and subsequent reduction in dose rate) at wide angles up to 60°. See Figure 12b for an illustration of the testing setup. In the same manner, a spectral analyzer (Amptek XR-100T-CdTe) was used to measure the energy distribution from the central focal spot at a distance of 50 cm and viewing angles of 0° and 60°, for a

period of one hour (~7200 exposures) at each angle. All spectrum and HVL measurements were performed at 120 kVp, 12 mA anode current, and 1.0 ms exposure time with 2 Hz pulsing frequency.
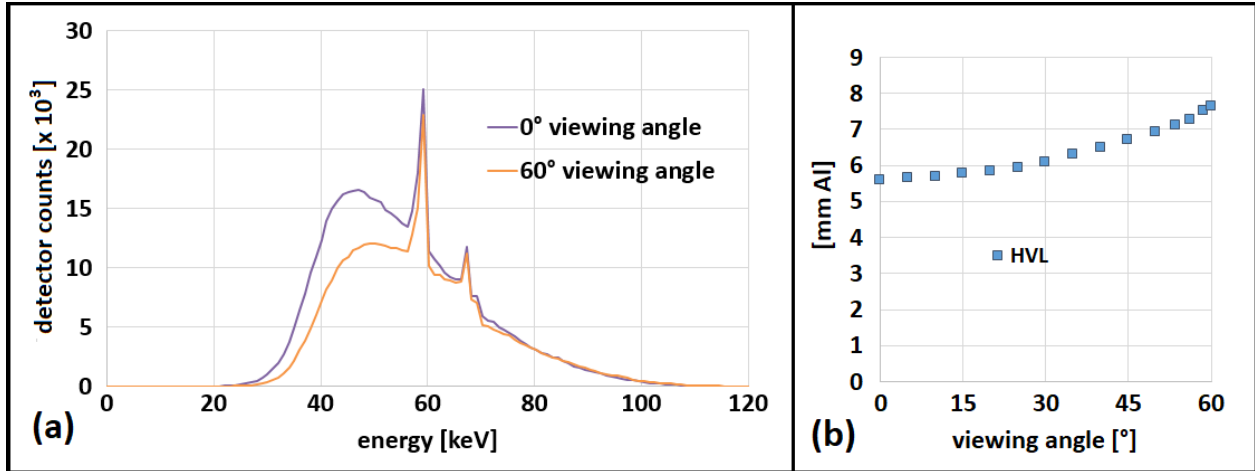
Figure 15: (a) Energy distribution measured from central beam of the CNT x-ray source array, displayed with 1 keV bin size. (b) The HVL changes from 5.7 to 7.6 mm Al when the viewing angle is swept from 0 to 60 degrees.

The output spectrum of the central beam is shown for viewing angles 0 and 60 degrees in Figure 15a. The expected beam hardening effect is observed and confirmed by the HVL variation with respect to θ in Figure 15b. At a 0° viewing angle, the HVL is 5.7 mm Al, with an average energy of 55.6 keV. At the 60° viewing angle, these values are shifted to 7.6 mm Al and 58.2 keV.

Due to the variation in exit angle from the CNT source window, the HVL increases at wide angles, which is confirmed by these measurements. From 0 to 60 degrees, the HVL changes from 5.7 to 7.6, corresponding to an average energy shift of ~ 3 keV. The spectrum and HVL measurements at 60 degrees correspond to a worst case scenario in terms of the widest fan-angle expected to be used from these sources (120°). In most practical imaging geometries for head CT, the beam will require additional filtration. Specially designed filters with varying thickness for each focal spot could potentially be used to even out the energy variation within the desired FOV.

3.2.3 X-ray exposure measurement

Each emitter in the CNT source array is controlled by a switching ECS with 96 channels. The included software allows the user to program a nominal cathode current, which is maintained by the ECS for a specified duration. In these experiments, the cathode current was monitored for each source in the array via oscilloscope (Tektronix TBS1064) using the ECS output interface. The ECS output signal was calibrated by simultaneously using a current sensing probe (Tektronix AMP-100). It should be noted that the ECS cathode current signal does not represent the true anode x-ray current. According to the manufacturer, only about 80% of the free electrons generated by the CNTs are transmitted to the anode. In this study, the term "transmission rate" refers to this effect. For verification and quantification of the x-ray output, a dosimeter (RaySafe X2 R/F sensor) was used to evaluate the exposure in mGy/s for each beam at a distance of 50 cm from the center of the array. Figure 12d shows a diagram of the experimental setup. In this measurement, the exposure rate is expected to decline as the source position moves away from center. The variations in SDD (r), incident angle (φ), and x-ray exit angle (θ) all contribute to this effect, and all three can be measured and used to normalize the exposure rates. The three correction factors are defined as such:

SDD
$$A(r) = \left(\frac{r}{d}\right)^2 \tag{1}$$

X-ray exit angle
$$B(\theta) = \exp\left(-\mu_W x_0 \left(\frac{1}{\cos(\theta)} - 1\right) - \mu_T D_{avg}\left(\frac{\cos(\alpha)}{\sin(\alpha)} - \frac{\cos(\alpha)}{\sin(\alpha\cos(\theta))}\right)\right) \tag{2}$$

Dosimeter incident angle
$$C(\phi) = \text{see Supplemental data} \tag{3}$$

$$Corrected\ dose\ rate = A(r)B(\theta)C(\phi)(Measured\ dose\ rate) \tag{4}$$

The first correction factor $A(r)$ increases the dosimeter reading according to the inverse square law, where the central source remains uncorrected ($d = r$). The second correction factor $B(\theta)$ takes into account the extra attenuation caused by the increased window thickness (Δx) illustrated in Figure 12c, as well as the additional heel effect caused by the decreasing heel angle (ω) (Figure 12f). Using the NIST materials database for Fe and W, the linear attenuation coefficients of the window and target materials are

estimated at average energy 40 keV to be μ_W = 2.9 and μ_T = 20.5 mm^{-1}, respectively. The heel effect

attenuation is calculated using a 'constant depth of production model'[100] with an average electron

penetration depth D_{avg} = 2.0 μm. The window thickness and anode angle are reported to be x_0 = 0.2 mm

and α = 12° from the manufacturer. In order to verify the validity of Eq. (2) and the nominal values, the

experimental setup in Figure 12b was used to measure the dose rate at a range of exit angles (θ) for the

same beam.

      The final correction factor $C(\phi)$ normalizes the dose rate from each emitter based on the calculated

angle of incidence on the dosimeter. According to the dosimeter specifications, the R/F sensor has

uniform response within an incident angle of φ < 10°. With an SDD of d = 500 mm from the central

source, the sources at extreme ends of the array have incident angles of 28°. In order to characterize the

dosimeter response for the full range of incident angles, the experimental setup in Figure 12e was used

with a single source (central focal spot #23). The dosimeter was fixated to a rotation stage and pivoted

from -40° to +40° in 1° increments to obtain a calibration curve for this sensor (Figure 16). Unless noted

otherwise, all exposure measurements were performed at 120 kVp, 12 mA anode current, and 3.2 ms

exposure time.
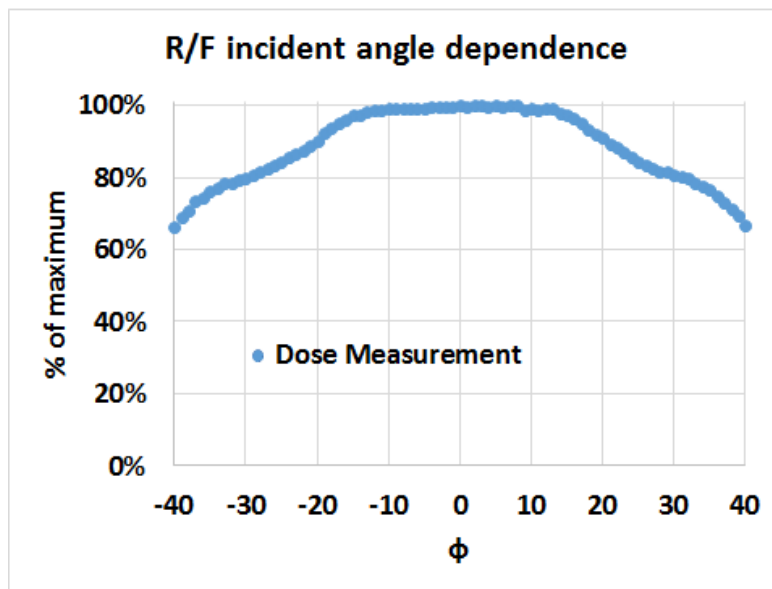
Figure 16: Calibration curve for the RaySafe R/F sensor as a function of incident angle on the sensor face.

The emitter current measurements for the central beam are displayed in Figure 17a. The current probe confirms the validity of the ECS cathode current output, and the beam can reach up to 40 mA anode current and 20 ms exposure. This is intended as a demonstration of the CNT cathode performance at low anode voltage (~20kV). The limitation on the total mAs available from a given focal spot is based not on cathode performance, but rather depends on the maximum temperature increase (ΔT) that the target material can tolerate. For a stationary target, ΔT can be estimated over a short exposure time (τ) using a simplified version of the Oosterkamp formula[101]:

$$\Delta T = \frac{2\Lambda}{wl} \sqrt{\frac{\tau}{k\rho c_p \pi}} \qquad (5)$$

The values k, ρ, and c_p are the thermal conductivity, density, and specific heat capacity of the target material (tungsten). The input power (Λ) is deposited over an area of size w x l. From the FSS measurement, $w = 1.2$ mm and $l = 5.8$ mm. The electron bombardment area is larger in the length direction due to the anode angle (12°). Using an input power of 4800 W (120 kV, 40 mA) and exposure time $\tau = 10$ ms, a temperature rise of $\Delta T = 3800$ K is calculated, indicating melting of the target material. This calculation is a rough estimate; the simplified Oosterkamp formula may not hold true for exposure times > 1 ms, and also fails to account for the power carried by backscattered electrons. In this case, the formula is used to provide confidence that a given individual focal spot can operate reliably at the target exposure settings (120 kV, 12 mA, 5 ms).
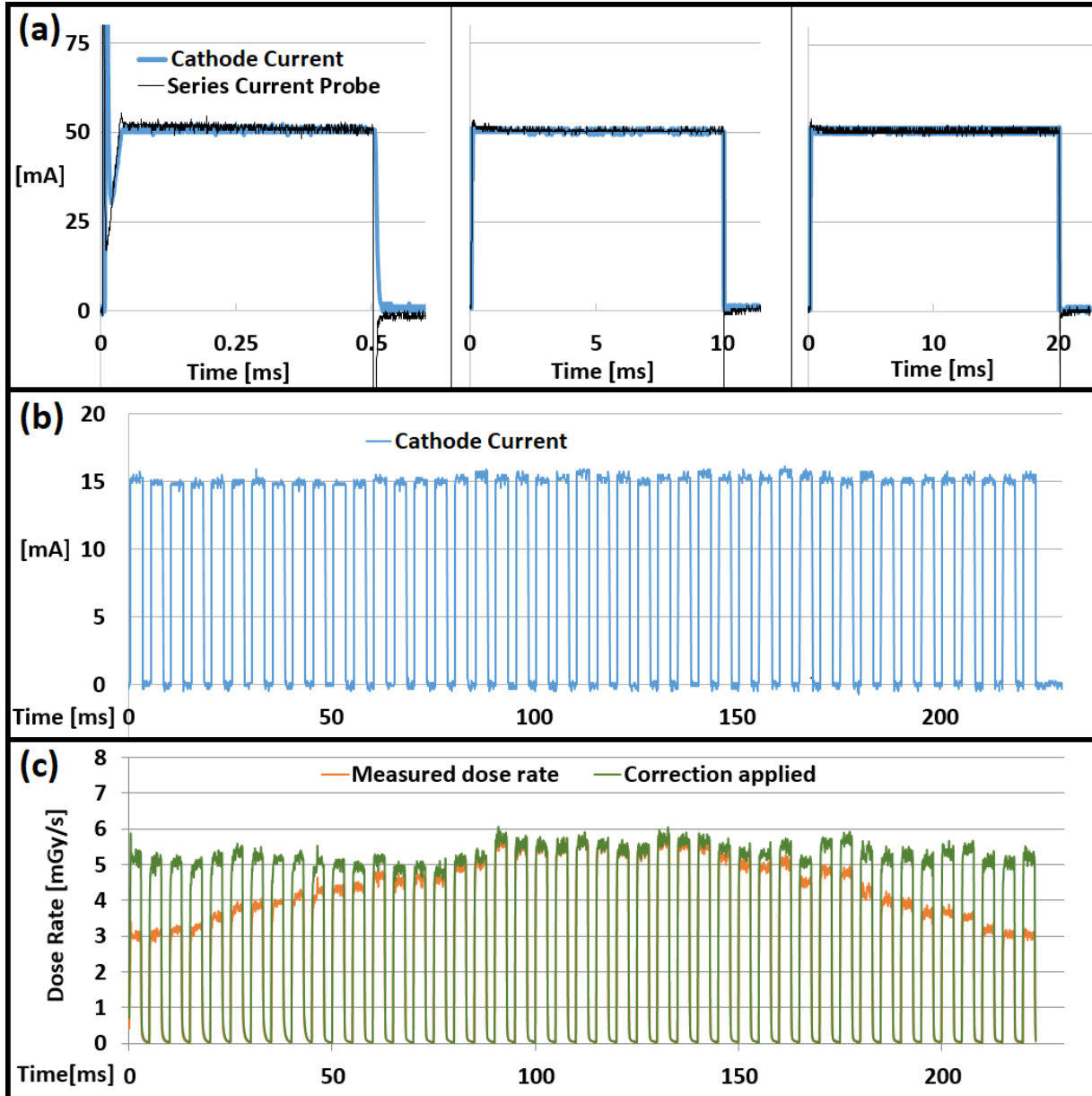
Figure 17: (a) Calibration of cathode current readback signal from the ECS. 50mA nominal current was used with exposure times of 0.5, 10, and 20 ms. (b) All 45 beams programmed for 15 mA cathode current (12 mA focal spot current) and 3.2 ms exposure time. (c) Dose rate as measured at a SDD of 0.5 m from the central beam, and subsequently corrected for known variations in SDD, incident detector angle (ϕ), and x-ray exit angle (θ).

To demonstrate a portion of a typical CT scan, each emitter cathode was programmed at a nominal 15 mA (12 mA anode current) with 3.2 ms on-time. The resulting cathode current measurement for all 45beams is shown in Figure 17b along with the corresponding dose rate measurement (Figure 17c). As expected, the dose rate decreases for off center beam positions.
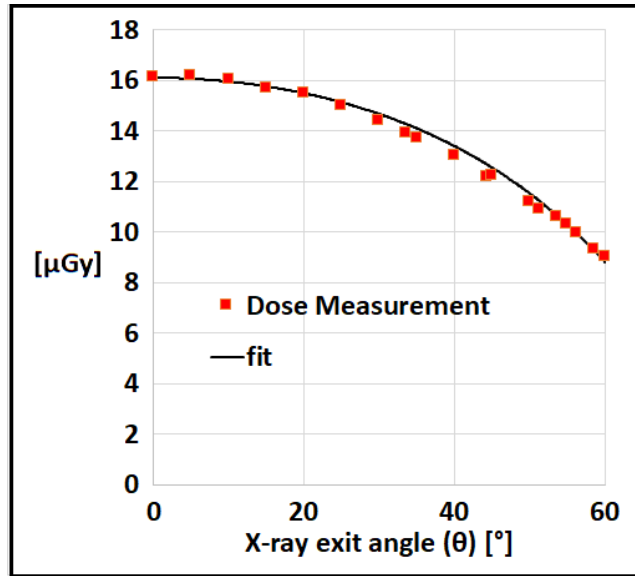
Figure 18: Reduction in dose with respect to viewing angle, keeping exposure time, SDD and incident detector angle constant.

By keeping the SDD and incident angle constant, the attenuating effect as a function of x-ray exit angle (θ) is isolated in Figure 18. The fit according to Eq. (2) provides verification that this formula can be used to normalize the dose rate measurements for known variations in θ. Using the correction factors for SDD, x-ray exit angle, and incident detector angle, the original dose rate data has been normalized in Figure 17c. After correction, the average dose rate for all 45 sources is found to be 5.28 mGy/sec at 0.5 m from the source, with a standard deviation of 0.24 mGy/sec. The dose rate variation from source to source ($\pm$ 5%) is larger than the random variation in cathode current produced by the ECS ($\pm$ 1.5%). This is attributed to the variation in electron beam transmission rate for each individual CNT emitter cathode. This source to source variation is found to be deterministic; repeated measurements of the cathode current for any given individual source fall within $\pm < 1\%$ of the nominal value. While direct measurement of the fast switching anode current is not possible at high voltage with the given equipment, the anode transmission has been reported from the supplier to be approximately 80% of the cathode current. Given the normalized direct dose rate measurement of the array's x-ray output, it can be assumed that the transmission rate also varies by $\pm$ 5% from source to source.

34

One challenge that is unique to the CT design using linear source arrays comparing to a conventional single-source rotating gantry system is the variation in both the SDD and the filtration from focal spot to focal spot, producing non-uniform imaging dose for each projection if the same mAs is used for each focal spot. This non-uniformity can be compensated by varying the exposure from each focal spot, using a unique feature of the ECS which has the ability to program the tube current individually for each focal spot for uniform exposure at the object. This is a major benefit of the CNT x-ray source technology, as the dose can potentially be tailored for larger patients or to avoid sensitive organs in more advanced ways than simple filtration. This effect could potentially be used to calibrate for a wide range of system configurations and dose requirements. Figure 19 shows a demonstration of this calibration for uniform dose rate at the isocenter of a proposed system with 50 cm SID targeting 0.015 mGy per projection. After ECS calibration, the resulting dose rate per projection was 5.0 mGy/s with $\pm$ 0.5% tolerance from source to source (Figure 19b).

The CNT x-ray source array is a competitive candidate for s-HCT. The source has demonstrated reliable and repeatable operation at the power and energy required for the intended imaging geometry and protocol. The measured FSS, HVL, and dose rates meet the requirements for this unique application. The challenges associated with using these source arrays for CT are geometry related. The linear nature of the currently available CNT x-ray source array will force a polygonal shape in the source ring, and subsequently each focal spot will have a different SID. As part of this evaluation, the effects of the varying SID (and viewing angles) on FSS, HVL, and effective dose per projection have been quantified. As demonstrated, the ECS can be programmed to accommodate for these effects in a wide variety of polygonal source arrays.
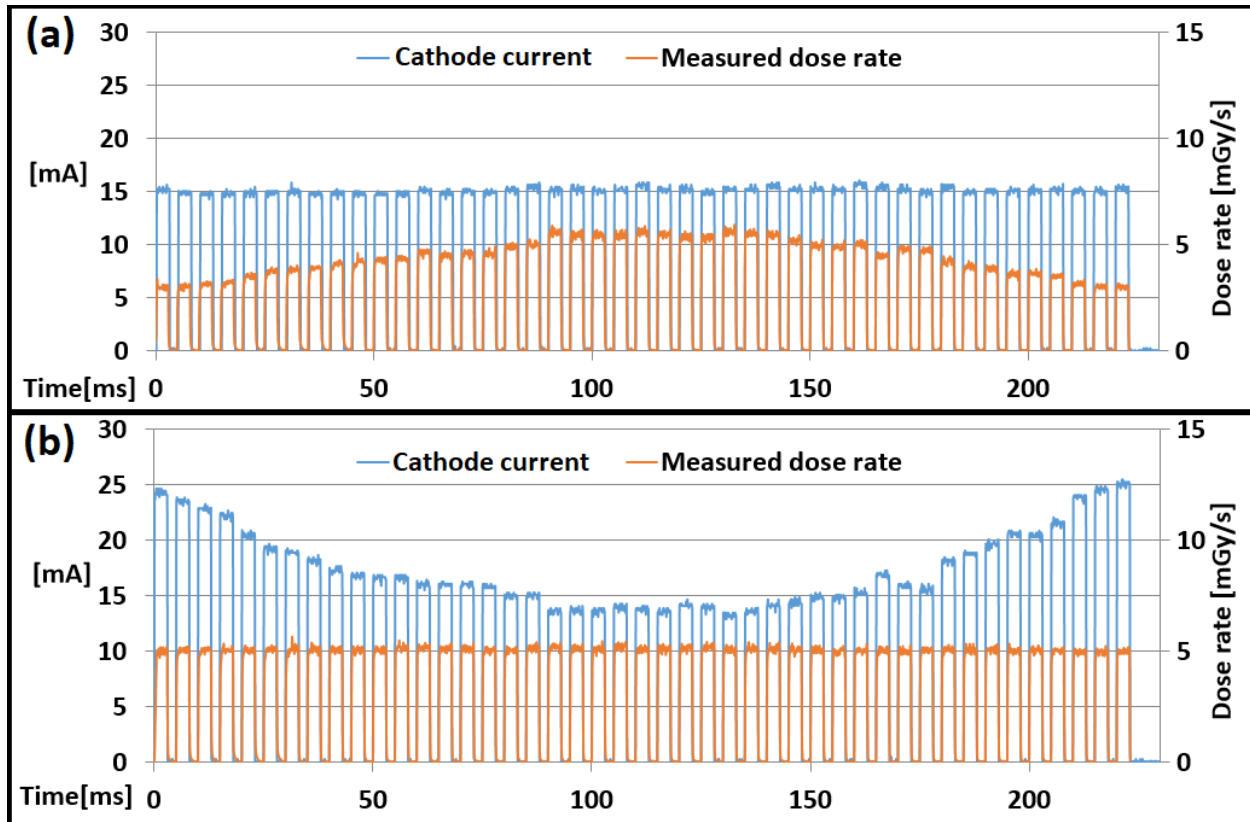
Figure 19: (a) A scan of all 45 beams at constant current and the resulting dose rate measured at a SDD of 0.5 m from the central beam. (b) Calibrated scan using individually programmed nominal current values for each beam and the resulting dose rate measurement.

3.3 System Architecture and Optimization of Geometry

The implementation of linear source arrays in CT presents many fundamental challenges. The curved path of the x-ray source will be replaced by a straight line of emitters, representing a radical shift in system geometry. This concept has been presented in previous studies which demonstrate a tomosynthesis system retro-fitted with a linear source array[4,102]. Building off of these works, a CT system concept is envisioned which combines data from multiple tomosynthesis-style imaging planes into one reconstruction.

3.3.1 Polygonal CT Architecture

The early s-CT prototypes[30,31] used a circular arrangement of focal spot positions. This allows for easy integration with existing system designs, and more importantly with existing reconstruction software based on filtered back projection (FBP) and Feldkamp-Davis-Kress (FDK)[103] methods. Additionally, a circular configuration has the least variation in SID, making it the ideal shape for CT in general.
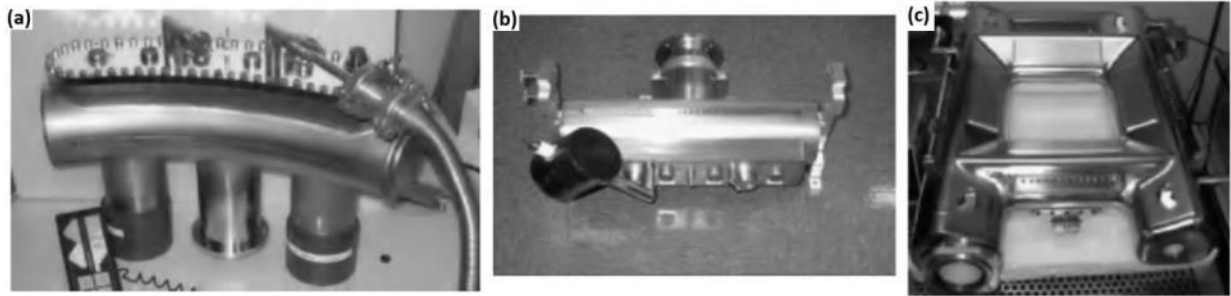
Figure 20: Early CNT X-ray source array prototypes, capable of operation at 120 kV, and customized for applications such as (a) s-CT, (b) baggage scanning, and (c) image-guided radiotherapy[63].

For these reasons, one the first CNT x-ray source array prototypes was constructed in curved shape featuring a 40° arc of ~ focal spots (Figure 20)[63]. Ultimately, the fabrication of such a curved array becomes expensive in the prototyping stage, and subsequent CNT x-ray source arrays (CNTXSA?) were built with linear (Figure 20b) or square (Figure 20c) geometries. As a result, many of the recent studies in s-CT with CNT x-ray source arrays have used non-circular architectures. In all of these cases, when viewed from the axial (*x-y*) plane, the linear source arrays form a polygonal configuration.
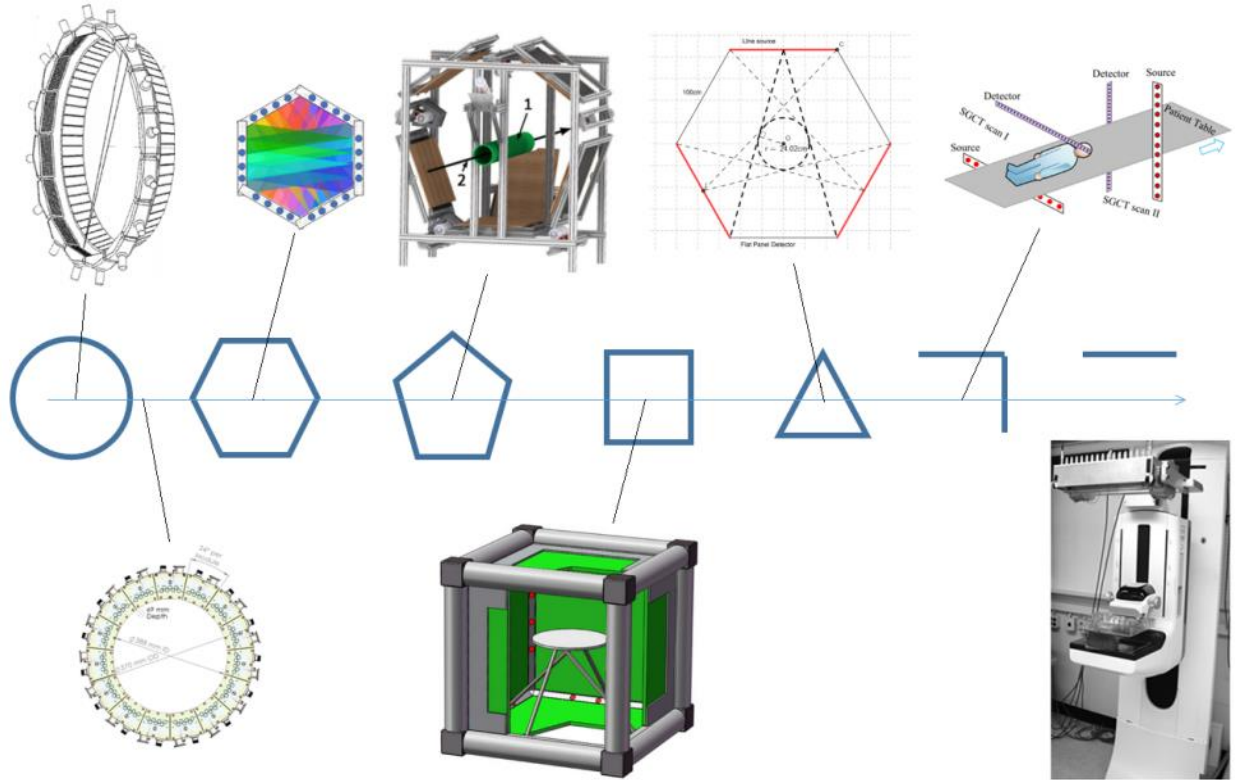
Figure 21: The broad spectrum of polygonal shapes possible with linearly distributed x-ray source arrays. Shorter arrays bring the system configuration close to a circle, such as a 17-sided[32] or 15-sided[83] shape. However most practical geometries have significantly fewer arrays, resulting in hexagonal [79], pentagonal[88], square/cubic[78], triangular[81], or L-shaped[80] configurations. Systems with only one linear x-ray source array are already in existence[4], commonly referred to as tomosynthesis devices.

One of the first decisions to make in designing the s-HCT system is the number of source arrays to include, as well as the shape of the overall arrangement. For a given length of a linearly distributed source array and a desired FOV, the number of possible polygonal shapes is actually quite limited. If the array length is short enough, the polygon can have many sides[32,83] and approach a circular shape. However, most existing distributed source arrays are several cm in length, and the resulting configurations are often in the shape of a hexagon[79,81], square[78], or L-shaped in the case of only 2 arrays[39,80] (Figure 21). On the extreme end of the spectrum of shapes is the case with only one array, such as previously mentioned tomosynthesis imaging configurations[4-7].

With the length of the source array(s) fixed at 53 cm and a desired axial FOV of ~20 cm diameter, the s-HCT system configuration was quickly narrowed down to having 3, 4, or 5 source arrays. Based on

previous experience, 2 arrays would not produce enough views, and 6 arrays would greatly increase the SID, placing higher power requirements on the x-ray anode. With the additional goal of portability in mind, a system with too many source arrays was considered undesirable.

The number of source arrays in the s-HCT system was also influenced by the implied number of focal spots. With the number of sources per array fixed at 45, the total number of projections can be either 135, 180, or 225 in systems with 3, 4, and 5 source arrays respectively. Out of a total angular span of 360°, the average angular resolution can be easily calculated in units of views per degree. While the number of view used in rotation-based systems can vary, a majority of commercial systems use a minimum of 720 views per rotation, imposing an angular resolution of 1 view every 0.5°. The average angular resolutions for the potential s-HCT system designs with 3, 4, and 5 arrays are calculated at 1 view every 2.7°, 2.0°, and 1.6° respectively.

3.3.2   Multi-plane imaging

The next consideration for the system architecture is the positioning of the x-ray detectors. Regardless of the specific details of the detectors (covered in greater depth in Section 4.2.1), they must be placed on the opposite side of the FOV as the corresponding source array. Unfortunately, the mechanical interference prevents all sources and detectors from occupying the same imaging plane. One way to address this problem would be to position the detectors with slight z-offset from the position of the source plane[32], which would introduce approximate cone-beam reconstruction artifact. The preferred solution is to arrange each source array and detector pair in separate but parallel imaging planes with minimum inter-plane spacing.

Collecting projection data in separate imaging planes is perhaps not the most ideal scenario. This means that the projection data for a given slice are acquired at different times. Furthermore, the object must be translated to complete image acquisition; single-slice still imaging is not possible. However, this is not a new concept. Even the state-of-the art CT scanners still require accurately calibrated z-translation of the object, since the detector z-dimension is usually much smaller than the object length.

39

3.3.3 Sinogram coverage

In order to determine the best possible configuration of source arrays and detectors, the total coverage was considered in the form of a sinogram. Each voxel in the reconstructed FOV must be informed by a number of rays from different angles spanning at least up to 180° in order to fully resolve the shape of imaging objects.
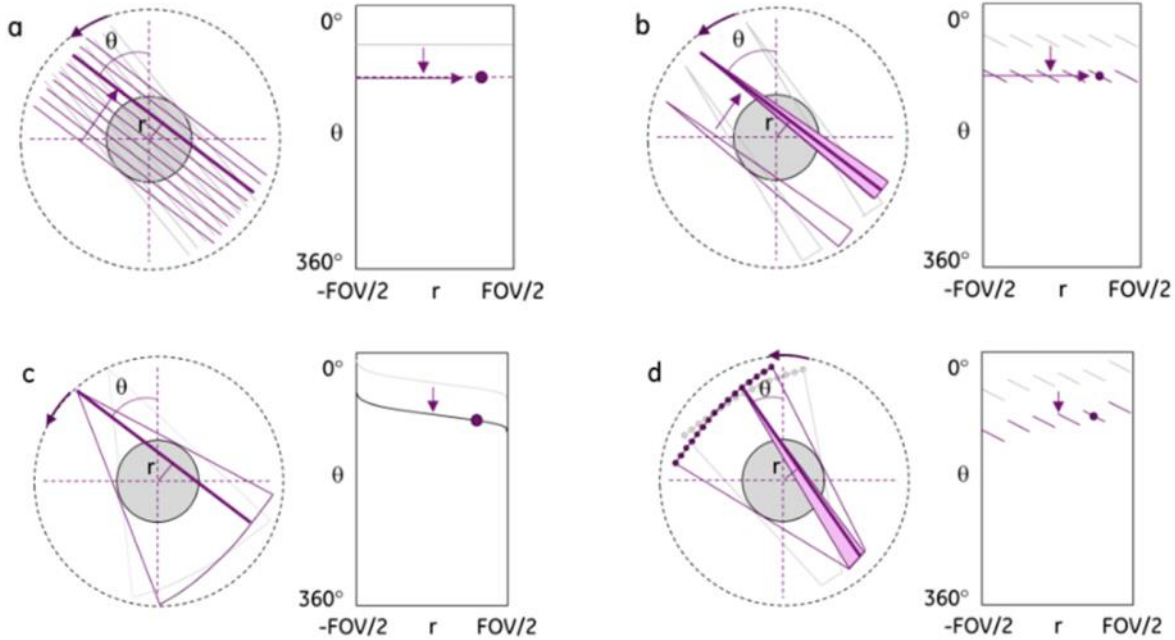
Figure 22: The sinogram maps acquired via Radon transform of four different rotation-based CT system geometries. (a) First-generation, (b) second-generation, and (c) third-generation systems with a single source. (d) IGCT uses multiple sources[28].

For the best visualization of the total coverage provided by a given system geometry, each ray (source → detector pixel) is plotted in a sinogram of ray angle vs. distance from origin. Each ray can be represented in polar coordinates: θ is the angle the projection ray makes with the *y*-axis and *r* is the signed orthogonal distance between the ray and the origin (a minus sign is added if the origin is to the left of the ray as seen by the x-ray source). While rotation-based systems naturally have "complete" angular ray coverage within the FOV (Figure 22), hardware limitations on s-CT architectures are often "incomplete" due to low density of views or large gaps of missing views.

This technique of visualizing sinogram space via Radon transform of the Cartesian system geometry is well-known and has been used to aid the design of other stationary CT systems[39,81,104] (Figure 23). In these examples, it is noted that triangular[81] or hexagonal[104] designs with 3 source arrays provides more coverage at the center of the field of view than square [104] and rectangular[39] geometries.
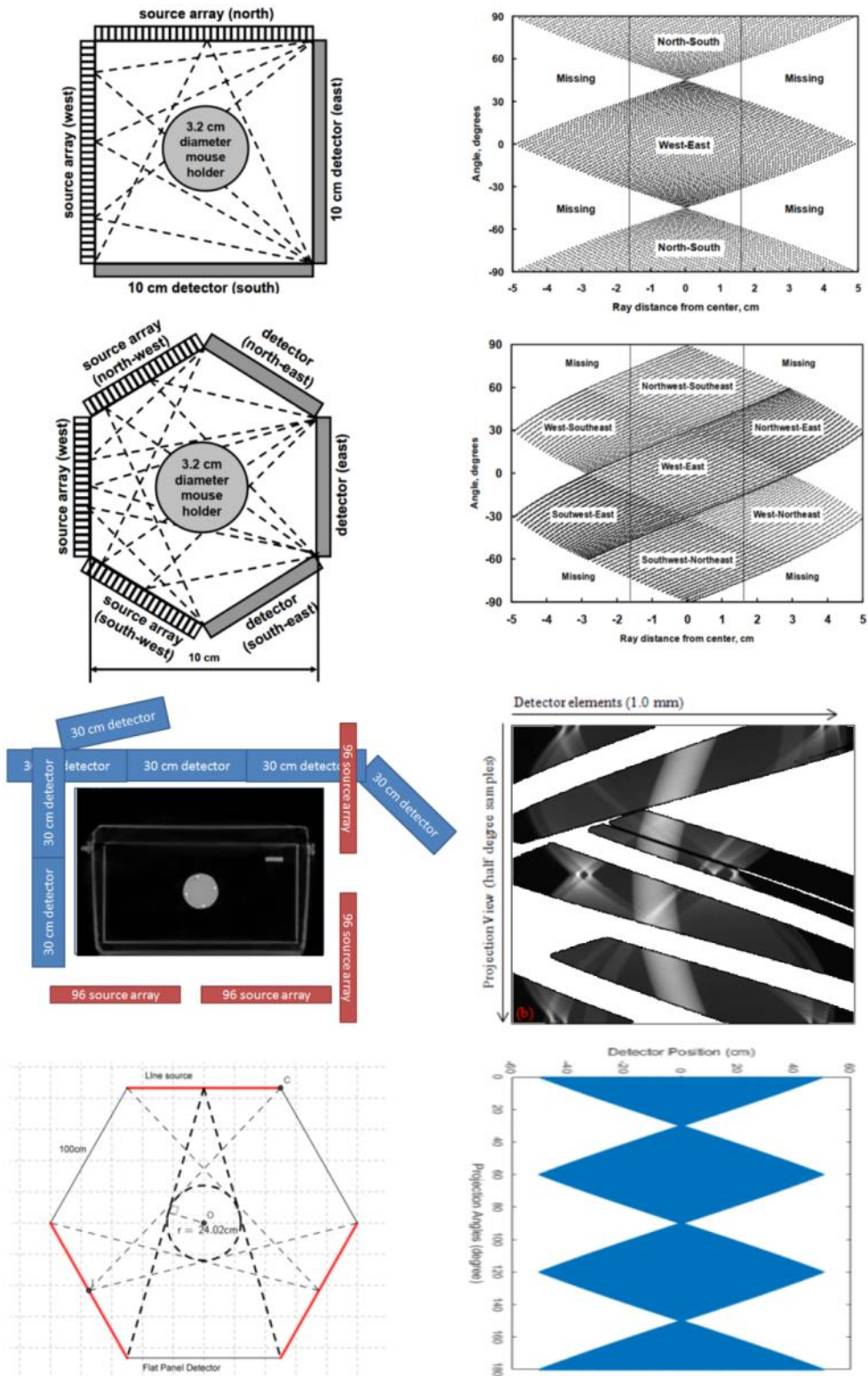
Figure 23: Various s-CT configurations and their accompanying sinogram coverage maps calculated by Radon transform. (a) Square [104] and (c) rectangular[39]geometries have larger coverage gaps compared to (b) hexagonal[104] or (d) triangular[81] designs.

3.3.4   Benchtop feasibility study

Figure 24b shows the experimental benchtop s-HCT setup consisting of a CNT linear x-ray source array, 3 flat panel CMOS detectors (Teledyne Xineos 2301), and a programmable rotation stage near the isocenter for object rotation. By rotating the object/phantom relative to the source-detector array, this bench-top system can emulate different polygonal acquisition geometries. This setup has been used to generate projection data from around the object using only one linear x-ray source array for simulation of a fully stationary system.
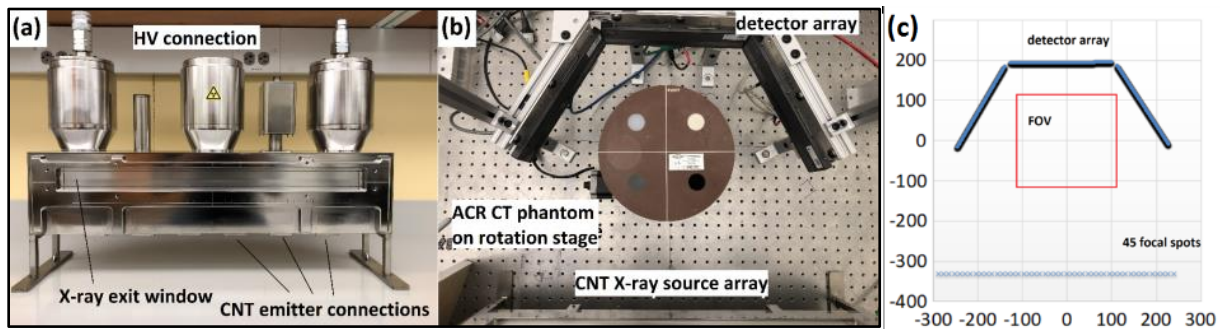
Figure 24: (a) CNT x-ray source array and (b) Bench-top s-HCT system with a segmented multi-row detector array. The rotation stage can be used to turn the object incrementally and simulate a system with multiple CNT X-ray source arrays. (c) 2-dimensional source-detector geometry of the benchtop s-HCT system, on a coordinate plane with the origin at the center of rotation. Dimensions are in mm.

Figure 24c shows the source-detector geometry as calculated from the use of small customized calibration phantoms (details on the calibration procedure can be found in Section 4.3). The s-HCT system design differs from conventional systems in that the SDD and SID vary for each focal spot. On average, each beam that passes through the square FOV has an SDD of 530 mm, and the angular coverage of x-ray at the isocenter is 90°. This configuration was used to gather projection data in 120° rotation steps to generate a triangular dataset, simulating a system with 3 linear x-ray source arrays.

Each detector has an effective imaging area of 228mm × 6.8mm with 0.099 × 0.099 mm pixel size. This detector was chosen for its high resolution, sensitivity, and fast frame rate of 300 fps. Furthermore, the multi-row aspect of this detector allows for selective summing to produce a desired reconstructed axial slice thickness. At a SDD of 530mm and detector height of 6.8mm, the maximum cone angle is 0.4°

which allows for 2D fan-beam reconstruction to be implemented with minimal cone-beam artifacts. In this particular study, the center 50 detector rows were binned (in the z-dimension) for an effective detector height of 5mm. The detector data was binned in the fan beam direction as well for the purpose of increasing photon counts. The images presented from the s-HCT benchtop setup were reconstructed with projection data binned to 50×4 pixels for an effective pixel area of 1.96 mm^2.
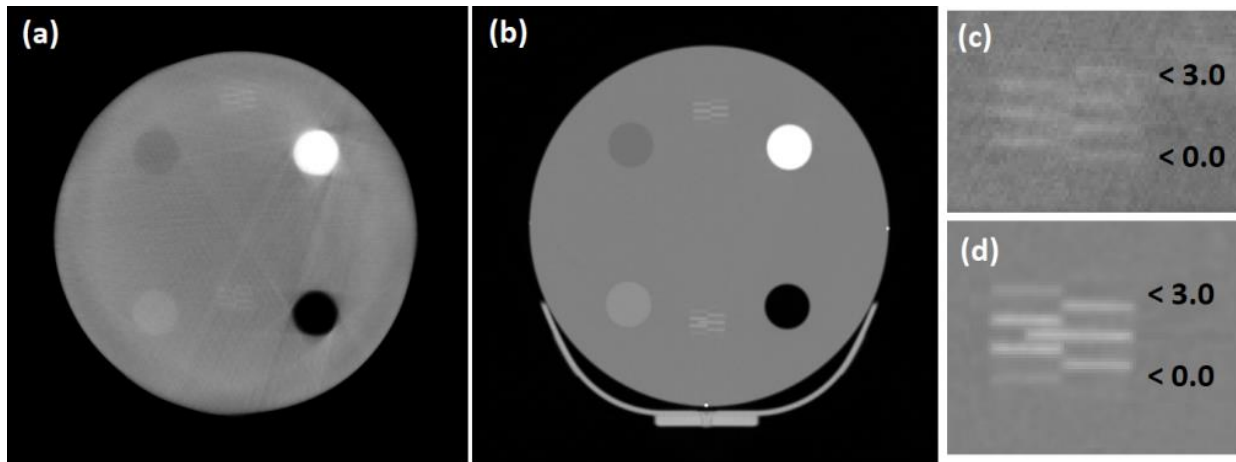
Figure 25: (a) Reconstructed image of the ACR CT phantom Module 01 taken with the benchtop s-HCT system. The projection data from 3 scans was combined to simulate a system with 3 CNT x-ray source arrays. (b) Clinical image of the same phantom taken with a Siemens SOMATOM Force. Both images are displayed with a window of [-1000 1000] HU. Zoomed images show slice thickness measurement for (c) the s-HCT system and (d) the clinical system.

The benchtop imaging setup was used to collect projection data of the ACR CT 464 phantom Module 01 in 3 scans of 45 sources each, rotating the phantom 120° in between each scan for a full 360° view with a total dose of 2.88 mGy at the isocenter. The resulting reconstructed axial slice is shown in Figure 25a alongside an image of the same phantom taken with the clinical scanner in Figure 25b. A slice thickness of 2.5 mm is confirmed for both systems in Figure 25c and d.

CHAPTER 4: S-HCT PROTOTYPE

Parts of this this chapter have been reproduced from previously published works[10,11]

4.1   System Architecture
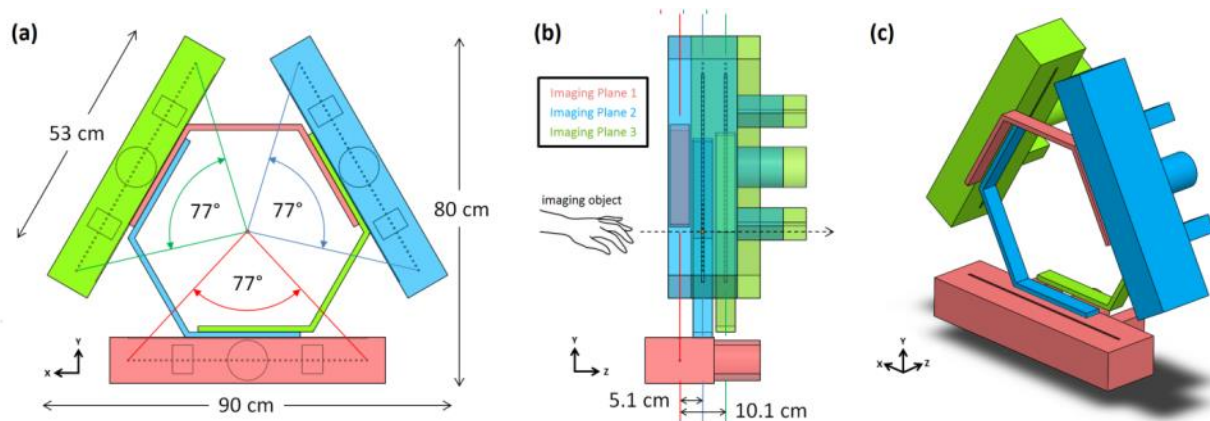
Figure 26: Architecture of the prototype s-HCT scanner. (a) Axial view: each CNT x-ray source array has 45 focal spots, providing 77° of angular coverage at the isocenter. More views are afforded by duplicate imaging planes with z-offset. (b) Sagittal view: The parallel imaging planes are in different z positions to avoid mechanical interference. (c) Isometric view

The s-HCT system configuration is pictured in Figure 26. This particular arrangement of three linear CNT x-ray source arrays and nine detectors has been optimized for a FOV targeting human head CT imaging-in previous feasibility studies[8,10,12], based on the availability of existing components. Figure 26a shows the imaging geometry of a single plane (P1). By design, the source array and detector sensors are coplanar. The focal spots are spaced 12 mm apart for a total array length of 528 mm. At a SID of 330 mm, this produces 45 views with an angular range of 77° [-38.7 38.7]°, suggesting an average angular resolution of 1 view every 1.75°. Three linear detectors are arranged around the isocenter to form a hemi-hexagonal shape. The imaging geometry of P1 (red) is duplicated in P2 (blue), with a 120° rotation about the z-axis. The issue of detector hardware interference with other imaging planes is solved by offsetting the entire source-detector array by + 50.8 mm in z. The z-offset between imaging planes is currently

restricted by the *z*-dimension of the detector housing, and could potentially be reduced with customized detector arrays. The source-detector geometry is duplicated again in P3 (green), resulting in a stepwise spiral-like structure of the total 135 source and 9 detector architecture. The relative geometry of each coplanar source-detector system is identical for all three imaging planes. Arranging the three systems with three-fold rotational symmetry about the *z*-axis maximizes the angular range of the system, with views spanning 232° out of 360°.

4.2   Final Assembly

The s-HCT system (Figure 27) consists of 5 major hardware components: the x-ray sources, anode power supply (DC), cathode power supply (gated), flat panel detectors, and finally the linear translation stage for movement of the imaging object along the *z*-axis. The CNT x-ray source arrays (NuRay Technology Co., Ltd. M/N MED1245)   have been characterized previously[12]; a summary of relevant specifications is presented in Table 1.

Table 1: Specifications of the CNT x-ray source array used in the s-HCT system

X-ray tube type	Fixed linear anode
Filter	0.25 mm Sn
X-ray beam shape	1° cone beam
Focal spot size	1,0 (IEC)
Number of focal spots	45
Focal spot pitch [mm]	12.0
Anode voltage[kVp]	120
Anode current[mA]	16
X-ray exposure time [ms]	0.5 - 4.0
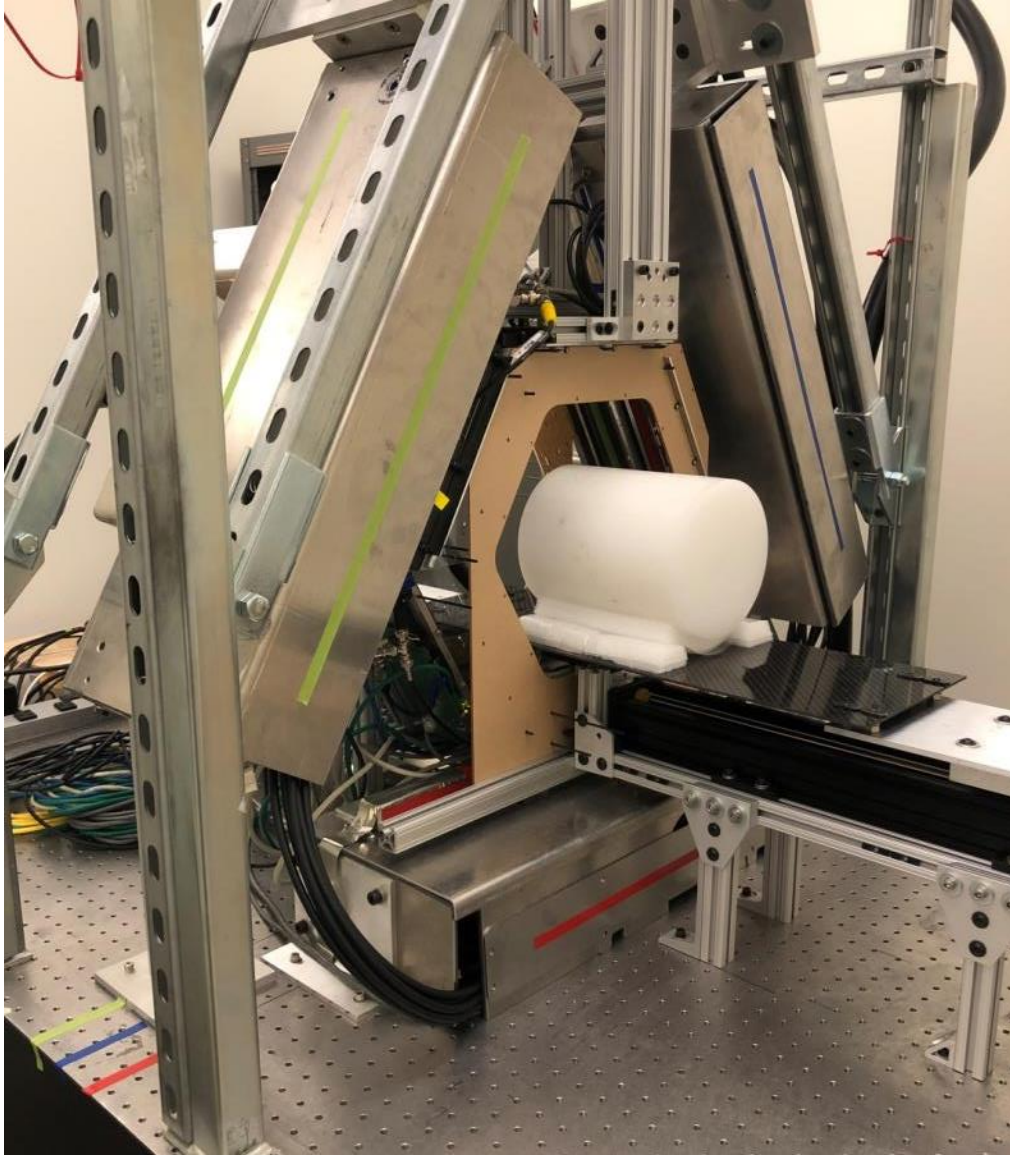
Figure 27: The s-CT prototype with a solid LDPE cylinder as the imaging object.

Three identical CNT x-ray source arrays with 45 beams each are used for a total of 135 views. A Spellman XRV x-ray generator provides the DC anode voltage, while the Electronic Control System (ECS) provides the bias extraction voltage to each CNT cathode individually. This cathode voltage is automatically adjusted in real time to maintain a constant tube current for the entire exposure duration. For a given focal spot, the ECS has been able to reproduce the same anode current (I_A) from scan to scan with a tolerance of < 1% in a previous demonstration[12]. In an effort to compensate for the variable SDD,

the I_A was adjusted for each focal spot in a 45-beam sequence to produce constant dose rate at the isocenter. While this capability exists, the focal spots are all operated at the same current in the present study. For verification, an oscilloscope (Tektronix TBS1064) was used to monitor the x-ray current from all focal spots via the ECS readback signal.

The ECS allows enormous flexibility for programming projection sequences not possible with rotating or moving sources. Also, the ECS can be used to provide the extraction voltage to cathodes in multiple source arrays, a feature which is used in the current system design. In the existing system, one 48-channel ECS is used to sequentially control 45 x-ray exposures in P1, and a second ECS with 96-channels controls the source arrays in P2 and P3. This configuration is based on available equipment; the potential exists to operate all three planes simultaneously through the addition of one more ECS control units.

4.2.1   Flat Panel X-ray Detectors

The rapidly switching x-ray beams from a single source array are collected by an opposing array of three flat panel detectors (Teledyne Xineos 2301). Each detector has an effective imaging area of 228mm $\times$ 6.8mm with 0.099×0.099 mm^2 pixel size, for a total detector length of 684 mm. In practice, this particular pixel size may be too small for this application, which is why the hardware binning feature (2x2) is used in this study, making for a 0.2 x 0.2 mm^2 pixel size in the raw projection data. Since this may still be too small (typical CT scanners have a pixel size on the order of ~1mm), the pre-processing software can bin the data further, allowing for the ideal pixel size to be optimized empirically.

This commercially available detector was chosen for its plug-and-play capability, high resolution, sensitivity, and fast frame rate of 300 fps. However, there are certainly many other considerations for selecting the ideal detector for this application, which could be implemented in future version of the prototype. For example, a direct conversion or photon counting detector with superior sensitivity may be more appropriate for this low-dose scenario. Also, a curved detector array with no gaps between modules would be the most ideal; such a shape could be customized for this particular system design.

4.2.2   Shielding and Collimation and Filtration

Within a single imaging plane, the x-ray beams are shaped to a very small cone angle ($< 1°$) by two extruded collimator leafs. Not only has this design been shown to reduce the "cupping" artifact due to scatter from large objects[11], but also it is necessary to minimize cross scatter between planes. As illustrated in Figure 28b, the collimator width (w) is tuned as small as possible to illuminate only the detector sensor area. At a SDD of 530mm and detector width (h) of 6.8mm, the maximum cone angle is 0.4° which allows for 2D fan-beam geometry to be implemented with minimal cone-beam artifacts, as in the previous study. In future iterations of the s-HCT system, total scan time could be reduced with a larger area detector by increasing h to 3-4 cm, giving more detector rows from the same exposure. This approach requires a 3D reconstruction with cone-beam filtering and other corrections.
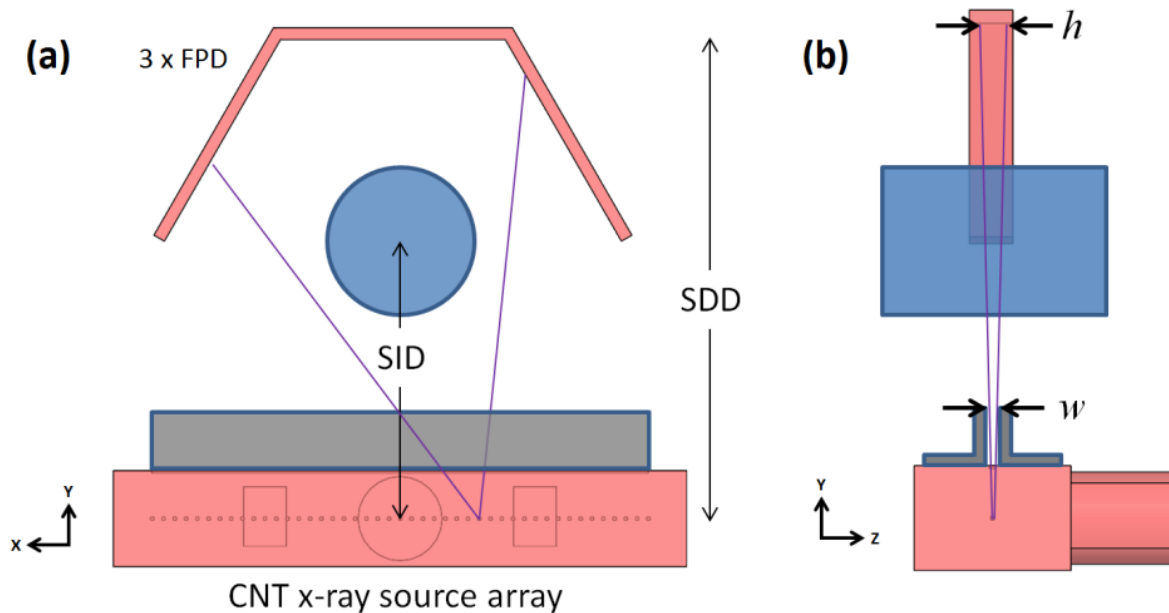
Figure 28:(a) 2D source-detector geometry of a single imaging plane. While the SID and SDD are fixed, the collimator design allows for adjustable cone angle as viewed from the sagittal plane (b)

4.2.3   Translation Stage

The translation of the imaging object is performed by a linear stage (Velmex BiSlide) and stepper motor with an effective linear step size of 5 μm. This level of precision may not be necessary for the

system, but is used to ensure constant speed during the imaging sequence for simple correction of motion-based artifacts.

4.3   Geometric Calibration Methods

One of the strongest arguments against the development of s-CT in general is the enormous difficulty of calibrating a large number of x-ray sources and detectors. Due to the prevalence of rotation-based CT, almost all existing calibration methods actually rely on the circular motion to neatly solve their underlying equations. For such a customized architecture as the s-HCT system, a new method must be derived and implemented, a topic which presents great opportunity for further research in s-CT. Here, two of the calibration methods used and their associated phantoms are described.

4.3.1   Single-plane x-y calibration (square method)

The source-detector geometry for a single imaging plane is pictured in Figure 29a. Ideally, the source array and detector array would have a curved structure to mimic rotation-based systems and keep a constant SID, but the existing hardware is linear, resulting in a polygonal configuration. Such a configuration does not lend itself well to traditional methods of CT geometry calibration, which usually rely on circular motion and sinogram data[105]. In this demonstration, the raw detector projection data of a square (4-point) phantom of known side length L is used to determine the relative positions of each source and detector.
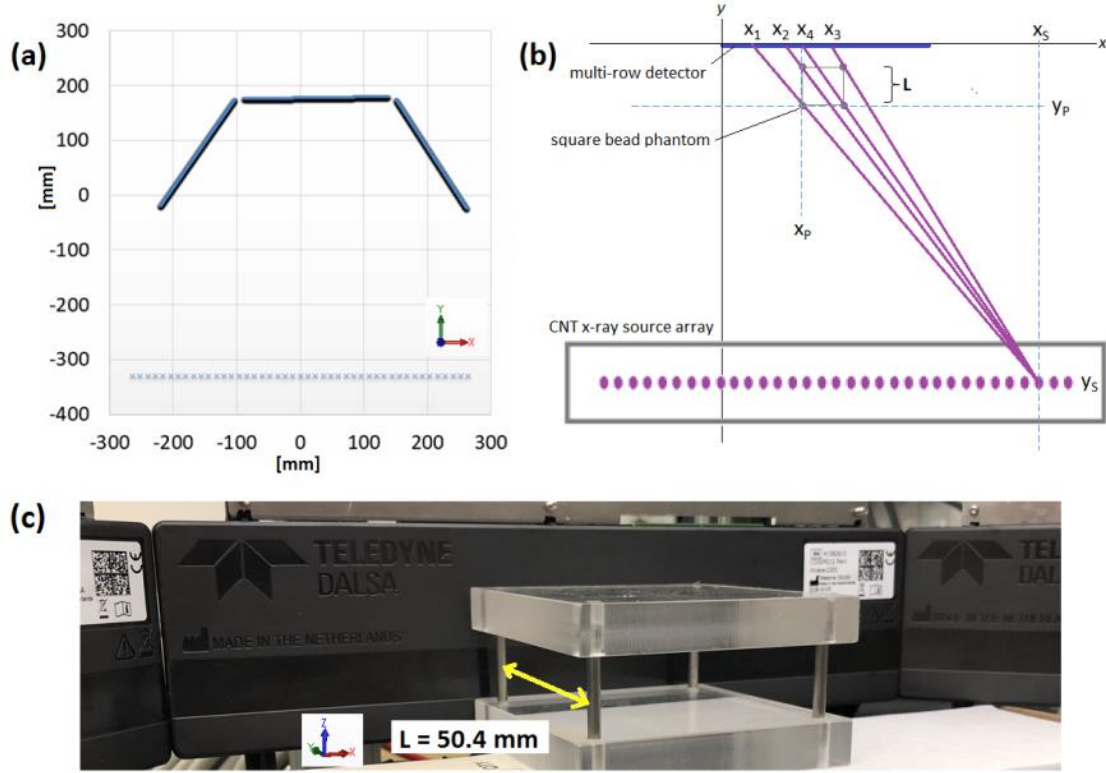
Figure 29: (a) Two-dimensional source-detector geometry of the benchtop s-HCT system, on a coordinate plane with the origin at the center of rotation. Dimensions are in mm. (b) Illustration of the square 4 bead phantom variables. The 23 cm detector array is defined along the x-axis with the leftmost pixel at x = 0, and the square phantom is positioned flush with the detector face. (c) Photo of the initial crude calibration phantom which used pins instead of beads.

The two-dimensional geometry of the imaging plane with the square phantom is illustrated in Figure 29b. The phantom must be mounted directly to the detector face to ensure squareness. All 45 sources are fired sequentially. Points x1-x4 are measured using a Gaussian fit of 50 averaged rows in the resulting image. From these four values and the known square phantom side distance *L*, the x and y coordinates for the phantom (x_P, y_P) and source (x_S, y_S) are derived using similar triangles, and calculated according to the following equations:

$$x_S = \frac{x_3(x_1 - x_2) + x_2(x_3 - x_4)}{(x_1 - x_2) + (x_3 - x_4)}, \quad y_S = \frac{(2x_s + x_2 + x_3)(x_4 - x_1)}{(x_1 - x_2) + (x_3 - x_4)} \tag{1}$$

$$x_P = \frac{L(x_S - x_4)}{(x_1 - x_4)}, \quad y_P = \frac{L\, y_S}{(x_1 - x_4)} \tag{2}$$

In order to derive the simplified two-dimensional formulas used in this study, the phantom is assumed to be a perfect square, with one side flush against the detector face. For the preliminary study, a crude rod phantom was used (Figure 29c) for a single square pattern (two versions, $L = 50.8, 63.5$) from each source.

The results of the preliminary square phantom calibration from 45 sources and 1 detector are shown in Figure 30a. The scan was performed twice with square pin phantoms of different sizes. Several outliers were removed after the observation that sources with x-positions near to x_P or $x_P + L$ gave erroneous values due to the overlapping projections of at least two pins. In the case of $L = 63.5$ mm, a single source position in between x_P and $x_P + L$ was found accurately. While the relative x-spacings between each source were found to be consistent with the 12mm nominal pitch (11.97 +/- 0.05mm), the y-positions were found to have errors as high as +/- 4 mm. Some reduction in the y error is noticed by enlarging the phantom bead spacing L from 50.8 to 63.5 mm. The linear fit of the 45-source array also shows an improvement in the R^2 value for the phantom with larger L value (Figure 30b).
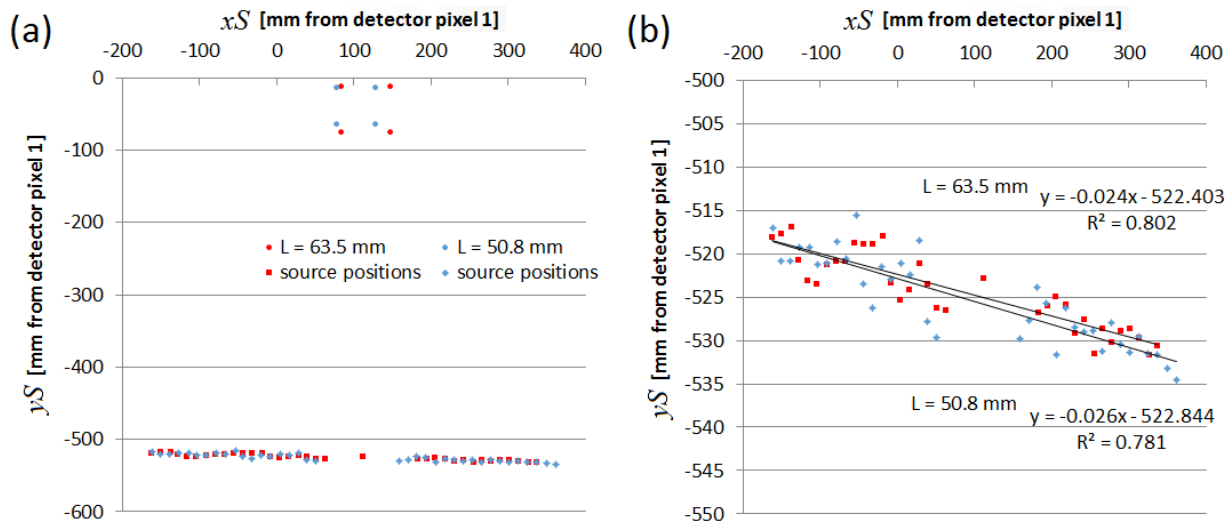
Figure 30: (a) Results of two separate geometry calibration scans using square phantoms of different side length L. The detector array lies along the x-axis from [0 230] mm. (b) Zoom window showing only the source coordinates. Some outliers were removed due to overlapping or truncated projections of the beads.

52

Based on these results, a second iteration of the phantom was constructed with the following improvements: a switch from 3 mm diameter rods to 1 mm beads, an increase in L to 88 mm, and the inclusion of several beads for a total of 22 square patterns. The 88 mm bead phantom is pictured in Figure 31.
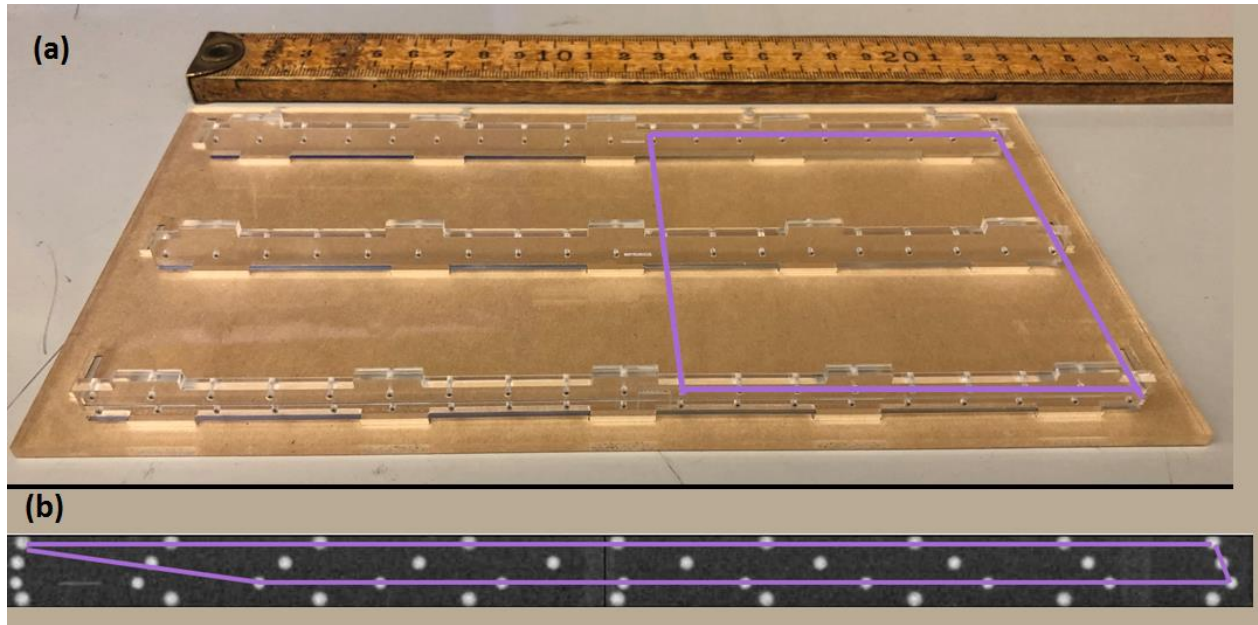
Figure 31: Photo of the bead calibration phantom. One of the squares of side length L = 88 mm is drawn over the photo as well as the resulting projection image from one of the x-ray sources in (b).

Calibration results from the second iteration of the phantom (Figure 31a) are presented in Figure 32. This phantom allows for several measurements for each source; the resulting values are an average reported with a standard deviation (σ) in both x and y coordinates (x_S and y_S). The slight separation of each row of beads in z (1.1 mm) prevents overlapping bead projections, allowing for all of the center sources to be calibrated.
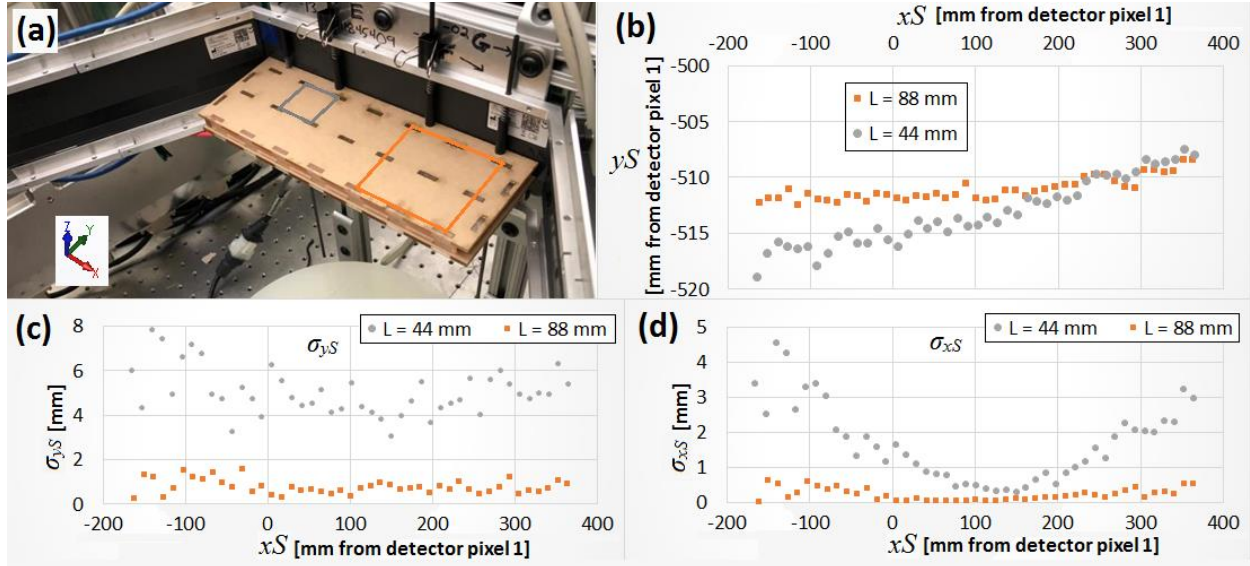
Figure 32: (a) Photo of the s-HCT benchtop setup with square bead phantom attached to center detector face. (b) Calibration results produced from one set of projection data from all 45 sources. The detector array lies along the x-axis from [0 230] mm. The reported y_s and x_s values are averages gathered from several square bead patterns; their standard deviations in are shown in (c) and (d).

The s-HCT system is essentially 3 separate tomosynthesis systems working together within the same three-dimensional coordinate system; it follows that this calibration procedure bears similarity to that of tomosynthesis systems[102]. With the given L values, the result of a single measurement lacks the precision necessary for CT calibration. The statistical advantage afforded by the bead phantom allows for sub-mm σ values when the 88 mm squares are used. The standard deviations (σ_{xS}, σ_{yS}) exhibit some dependency on x_S; sources directly in front of the detector are more accurately calibrated than those far to the side. It is also observed that the standard deviation and associated measurement error can be reduced by using larger values of L.

4.3.2   Multi-plane x-y thin wire method

The limitations of the 2D tomosynthesis-style calibration led to the exploration of alternative methods. After many efforts to calibrate the source-detector pairs with small beads mounted close to the detector, the next set of phantoms was constructed for placement within the image FOV. This was initially avoided due to the segmented nature of the detectors and large spans of truncated data (images

54

off the detector edge). However, with the beads close to the detector, the phantom only provides information about one detector, meaning the procedure needs to be repeated 9 times or with 9 phantoms at once. Calibrating all of the source-detector pairs separately represents a tremendous effort.
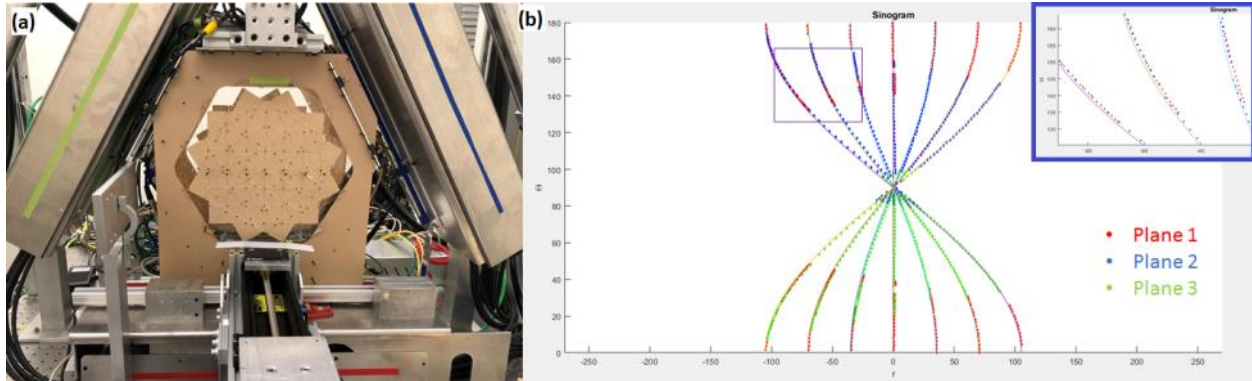
Figure 33: (a) Geometric Calibration phantom for the s-HCT system consisting of multiple parallel wires visible in all three planes. (b) Calibration measurement in sinogram space for the pictured configuration of wires. The calibration error is easily measured as the distance of each point from the "ground truth" sine curve (inset).

The next phantom for geometric calibration was inspired by a wire-based method[106]. A single wire can be easily modeled 3D space and compared to the projection data; this method seeks to gain a statistical advantage by using many wires distributed across the desired image space. Multiple straight steel wires were oriented parallel to the z-axis and suspended within the FOV (Figure 33a). This offers the advantage of higher magnification on the spacing in the 2D phantom images (more detector pixels for a given L value), as well as the ability to bridge the multi-plane configuration so that the same object is measured in all three planes. The other major advantage is the ability to work within the system sinogram space. The calibration error can be easily measured (Figure 33b) and uses as the input for a cost function. The calibration procedure involves shifting the source-detector geometry in small increments in order to minimize the value of this cost function.

The wires were held linear by rigid carbon fiber tubing. The position of the wires was fixed by an acrylic plate mounted to the detector assembly. The precision of the plate holes (< 0.025 mm) provides a "ground truth" position for the wires for comparison during the calibration process. Many wires can be imaged at once, but more difficulty arises when wires overlap. For this reason, the plate was designed so

the configuration of wire positions could be easily changed with minimal physical disturbance to the detector assembly.
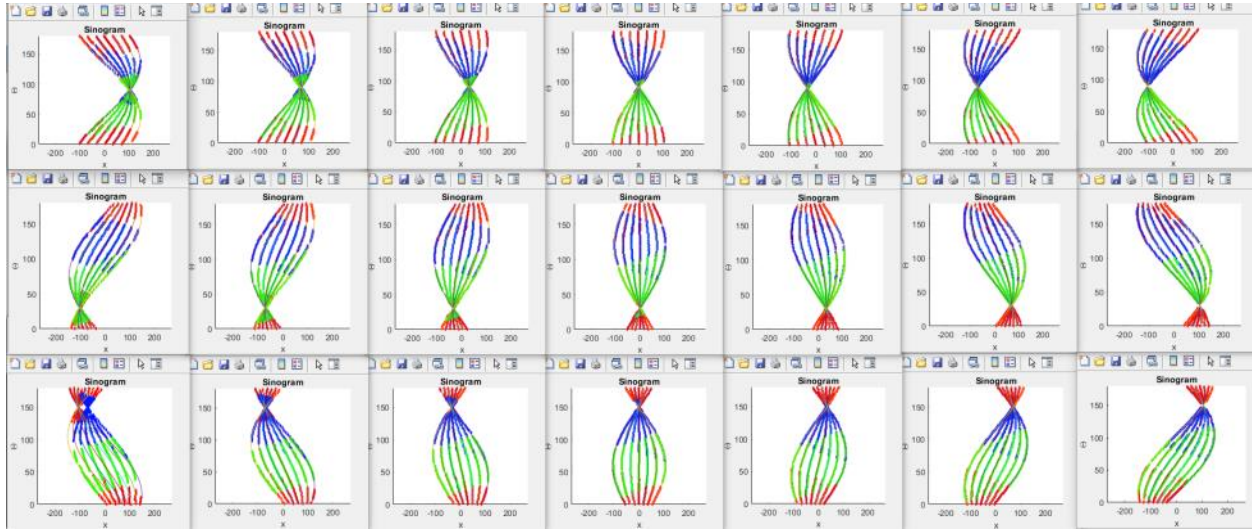
Figure 34: Calibration results from all 21 images of 7 thin wires each. The different configurations are meant to distribute the data points widely in all three imaging planes.

For a given plane, a configuration of wire positions parallel to the source array direction will have no overlap. The final calibration of the system was performed with 7 images of 7 wires each for a guaranteed 49 data points for each source. However, this configuration will have significant overlap in the other planes, reducing the number of useful data points. For this reason, each configuration is repeated 3 times with 120° rotation about the z-axis each time to match the shape of the system. After repeating for all three planes, all 21 images are used to contribute to the cost function sum. The geometry is then shifted and the cost function is minimized iteratively as such. The final results are shown in Figure 34. The accuracy of this calibration procedure is confirmed by spatial resolution measurements in Section 5.4.

4.4 Image Acquisition and Processing

Of course, none of the multi-source x-ray applications would be possible without the use of advanced iterative reconstruction algorithms. The constant need for dose reduction in the medical field has driven extensive research efforts focused on iterative CT reconstruction with low-dose or incomplete projection datasets[107-109]. Combined with noise suppressing methods such as compressed sensing and total variation minimization, algebraic iterative reconstruction (ART) has enabled the success of smaller, more dose-efficient quasi-CT systems such as the C-arm design. Along with recent advances in parallel computing power, the invention and refinement of iterative reconstruction techniques over the last ~20 years has led to the exploration of non-circular geometries previously not possible with existing FBP algorithms[110]. Compared to more well-established analytical Radon-based methods, these algorithms offer enormous flexibility in the system geometry, and are more forgiving in cases of limited number of views. As a result, many studies have been conducted to determine an acceptable level of view undersampling, with mixed results depending on the application[84].

The majority of stationary multi-beam x-ray source arrays, regardless of emitter type, are distributed along a straight line, due to the comparatively high cost of prototyping curved anodes and other components. The linear nature of these tubes lends itself well to existing "2.5D" tomosynthesis systems such as those used for mammography screening[4], but challenges are presented when attempting to adapt to the well-established field of circular CT. Specifically, the reconstruction algorithm and software will need to be changed. The most widely used method for CBCT reconstruction has been the Feldkamp, Davis, and Kress (FDK) algorithm[103], which has been heavily developed for a fixed radius system. The linear array of sources necessitates an alternative iterative technique.
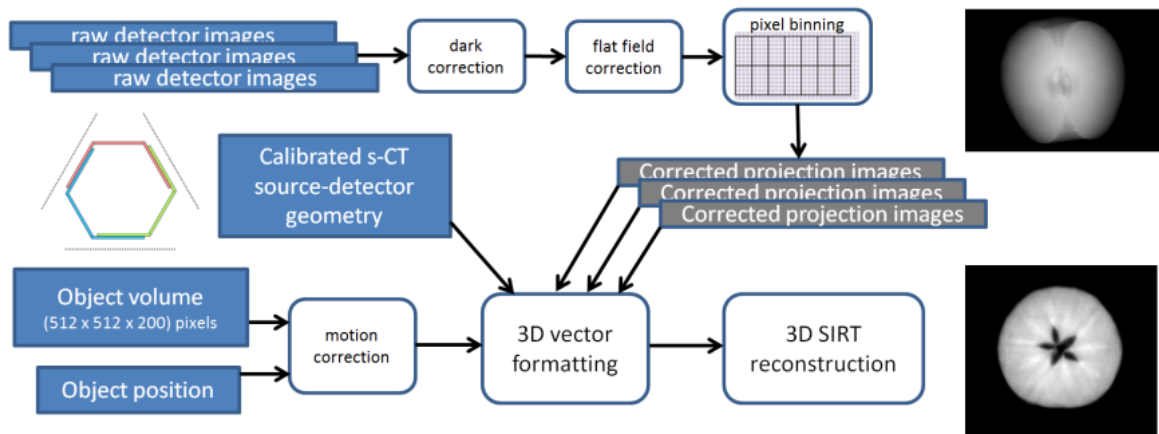
Figure 35: Input data and processing steps for 3D image reconstruction from the s-HCT system

The overall process for generation of 3D image data from the s-HCT system is shown in Figure 35. Square pulse waveform function generators are used to trigger the detector readouts. The delay is adjusted to synchronize the readout of one of the three detector arrays immediately after an x-ray exposure of time t from the corresponding source array. In a single imaging plane, 45 projection images are captured, and the same output comes from the other two imaging planes for a total of 135 views, each spanning three detectors. The raw projection image data is stored in buffer memory on a local CPU until the entire volume has been scanned, and then saved to disk upon completion of the programmed number of cycles. At the present, this is the part of data processing that takes the longest, with over 60,000 images.

After the raw projection data has been saved, dark and gain correction are applied, as well as a standard bad pixel map interpolation. The multi-row aspect of this detector allows for selective binning based on the desired reconstructed axial slice thickness. For example, in the reconstructed apple slice (Figure 35), the central 32 detector rows are used with 2 row binning (in the z-dimension) for an effective detector with 16 rows and total height of 6.4mm. The projection data are also binned laterally to 2 columns, resulting in an effective pixel size of 0.4 x 0.4 mm. Detector binning presents a tradeoff with respect to spatial resolution versus overall photon noise; appropriate values can be chosen depending on

the application. The tradeoffs associated with detector binning are discussed further in Section 5.3 and 5.4.

4.4.1   Reconstruction

After the pre-processing steps, the projection data are vectorized using the known system geometry. Given the x, y, and z, coordinates of the sources and the centers of the binned detector pixels, the system matrix can be calculated prior to imaging to reduce the overall reconstruction time. The object volume is generated with a user-input 3D voxel size and number of voxels. The reconstruction speed depends heavily on overall number of voxels; in this way the image size and resolution can be easily adjusted depending on the desired application. The voxel size must be chosen with consideration to the binned detector pixel size, to avoid over- or under-sampling. To correct for the motion of the object, the known imaging sequence is used to correct the z coordinates for each projection based on the translation speed.

The s-HCT reconstruction package is based on the ASTRA Toolbox[111] in Matlab R2020b. Previous work on the comparison of various algorithms[112] has led to the current version which uses a 3D Simultaneous Iterative Reconstruction Techniques (3D SIRT) implemented for GPU. The output volume size was chosen to be 512 x 512 x 512 voxels, with the center and ROI adjusted depending on the object. The voxel size can be chosen for the application; for the case of head imaging, axial slices are typically reconstructed with 0.5 (x) x 0.5 (y) mm^2 pixel size, and the z dimension can range from 0.5 to 5 mm.

CHAPTER 5: SYSTEM CHARACTERIZATION AND IMAGE QUALITY EVALUATION

The s-HCT scanner prototype scanner was assembled in the laboratory with 3 CNT distributed x-ray source arrays, 9 flat panel detectors, and a translation stage. After performing a geometry calibration and streamlining the MATLAB software (both described in the previous section), phantoms of any size comparable to a human head can be imaged and reconstructed within a few minutes. This chapter summarizes the imaging results of a variety of phantoms selected for the purpose of comparing the output CT images of s-HCT with those of clinical scanners.

5.1   Temporal resolution

One of the major advantages afforded by s-CT in general is the potential improvements in image acquisition time, or temporal resolution. With the rotational motion of the gantry eliminated, the focal spots can be scanned sequentially at much faster speed. However, without using a rotating anode, the temporal resolution is now limited by the amount of energy that can be deposited per focal spot needed to maintain image quality. This energy can be distributed over a longer exposure time to reduce the system power, but this goes against the goal of decreasing scan time. Increasing the temporal resolution means that the necessary energy is deposited over a shorter exposure time, increasing the overall system power and excess heat generation which can potentially melt the anode material and lead to x-ray source failures. Therefore, the anode heat management is one of the main limiting factors in increasing the temporal resolution in s-CT systems. Although the available mAs from each focal spot is limited, the s-HCT architecture has a major advantage over moving-source systems in that the 3 imaging planes can be acquired simultaneously.

5.1.1 Imaging Parameters

A summary of the fixed imaging parameters used in this study is given in Table 2. These values were chosen to meet a target exposure level, which was determined by considering the specifications of a rotation-based CT system of similar size (CereTom, Neurologica, Danvers, MA, USA)[93]. The commercial system typically uses 7.5 mAs per rotation in a routine low-dose adult head scan (3.75 mA, 120 kV, 2 sec rotation). It can be assumed that some of this exposure does not contribute to the image since the source is always on, even during the detector readout. This presents another advantage of s-CT: the scanning sequence can be programmed such that for a given imaging plane, no exposure occurs during detector readout, resulting in less wasted dose to the patient. The target exposure of 6.48 mAs used in the present study should be sufficient to visualize the features of head CT phantoms.

Table 2: Constant imaging parameters used in this study

Number of imaging planes:	3
Number of sources per plane:	45
Number of projections (N):	135
x-ray exposure time (t):	3 ms
Detector readout time (r):	1 ms
exposure per source:	0.048 mAs
total exposure per cycle:	6.48 mAs

Table 3: Cycle Times and resulting z-translation speeds for 2.5 mm/cycle

Imaging scheme:	Cycle time (T) [ms]	Translation speed (s) [mm/s]
a	588.0	4.25
b	588.0	4.25
c	441.0	5.67
d	294.0	8.50
e	196.0	12.76

5.1.2 Image Acquisition Speed

Many exposure schemes are possible with the s-HCT system. The use of multiple parallel imaging planes and object translation presents an immediate speed gain through simultaneous acquisition of views from different-positions of the object. For a fixed number of projections (N), the timing diagrams in Figure 36 illustrate how the cycle time (T) can be reduced dramatically by simultaneous data acquisition in the parallel imaging planes. The ECS allows for each focal spot to be individually controlled in terms of beam current (I_A), exposure time (t), and cycle time or period (T) with an option for delay (T_d). Through appropriate programming of the imaging sequence, the s-HCT system can readout the detectors in one plane while x-ray exposure occurs in another as in Figure 36c, in which case T depends only on t and N.
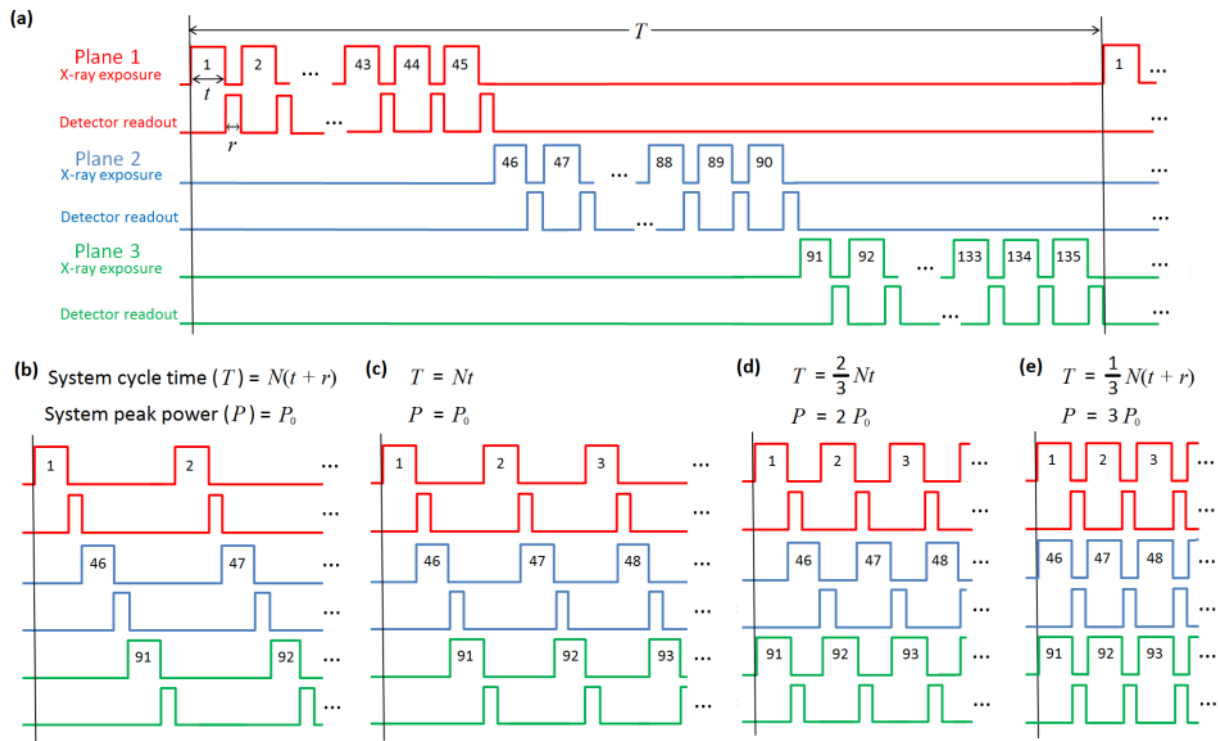
Figure 36: Timing diagrams exhibiting the variety of exposure schemes possible with the s-HCT system (N=135 projections). The fully sequential scheme (a) is similar to the helicial acquisition pattern of third-generation CT. The multi-plane architecture of the s-HCT system allows for simultaneous events, decreasing scan time at the cost of higher system power

This is just one example of how the solid-state nature of the prototype can be exploited to maximize scan speed depending on the situation. Although the current iteration of the s-HCT system can only perform schemes a-d due to the limitation of the system power, it is simple to calculate the gains in scanning speed by scanning all three planes simultaneously (scheme e) in future versions of the s-HCT system with a modified ECS. The translation speeds required for 2.5 mm coverage per cycle in each imaging scheme are shown in Table 3. For comparison, the Ceretom covers 10 mm per 2 second cycle, implying 5 mm/sec translation speed.

5.1.3   Dose Measurement

For quantification of the x-ray exposure provided by the s-HCT system, a CT probe (Raysafe Inc) was fixed to the translation stage. The omni-directional probe is effectively a pencil-shaped ion chamber 10 cm in length and 1 cm in diameter. While the response time of this sensor is not fast enough to see the start and stop of individual exposures, the time-averaged dose rate from each scan of the CNT x-ray source arrays can be observed. With the probe oriented along the system z axis (x, $y = 0,0$) and moving at constant speed, there are some positions where the chamber can receive radiation from 2 planes at once. For the first trials, the x-ray exposure scheme was programmed in sequential-plane mode (Figure 36a). For easy separation of dose from different imaging planes, 3 more scans were performed, each with only one of the three imaging planes operational. For the speed trials, exposure schemes b (Figure 36b), c (Figure 36c), and d (Figure 36d) were used with the translation speed adjusted appropriately to maintain equivalent scanning pitch.

CT probe measurement results from imaging schemes a through d are shown in Figure 37. In single-plane mode (Figure 36a), the separate scans using P1, P2, and P3 illustrate the alternating cycles generated by imaging scheme a. The cumulative exposure from a full scan of all three planes together (Figure 37b) produced 8.65 mGy. The scan was repeated three more times with imaging schemes b, c, and d (Figure 37c). The schemes with shorter cycle time (T) produce the same cumulative imaging dose when the translation speed (s) is adjusted according to Table 3. The system dose rate is increased

through the advantage of s-CT and simultaneous events, and subsequently the temporal resolution (and in this case scanning speed) is improved.
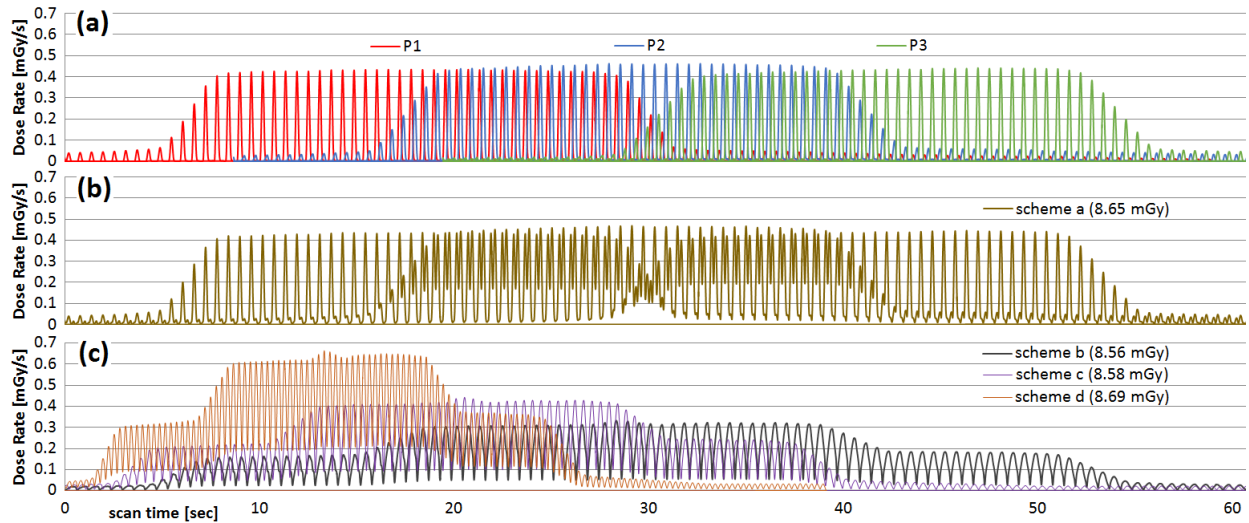
Figure 37: Real time CT probe dose rate measurements collected from the s-HCT prototype using different exposure schemes, cumulative exposure indicated in the legend. (a) Single plane imaging dose rate from all three planes taken in separate scans. (b) Total scanning exposure on the 10 cm probe with 4.25 mm/sec object translation speed and all three planes operating according to scheme a (Figure 36a) (c)Total scanning exposure from similar scans using schemes b, c, and d (Figure 36). The object translation speed is adjusted to match the decreasing cycle time and maintain constant pitch.

5.2   Phantom Imaging

The ability of the s-HCT prototype to collect full scans within minutes makes it well-equipped for rapid data collection. A wide variety of objects have been selected as the first imaging phantoms to be reconstructed in this project. Some objects such as the apple (Figure 38a) and lotus root (Figure 38b) are for qualitative display, while the LDPE cylinder (Figure 38c), ACR CT phantom (Figure 38d), and angiographic CT head phantom (Kyoto Kagaku Co.,Ltd.) (Figure 38e) are used for quantitative measurements of the reconstruction image quality. Unless otherwise noted, the data was acquired using scheme c (Figure 36c) and the 3D voxel size is fixed at 0.5 x 0.5 x 0.5 mm^3. The 3D renderings (Figure 38f-j) were performed using ImageJ. The axial slices for the apple (Figure 38k) and lotus root (Figure 38l) are binned to 1.0 mm slice thickness, and those for the LDPE cylinder, ACR, and Kyoto phantoms are binned to 2.5 mm.
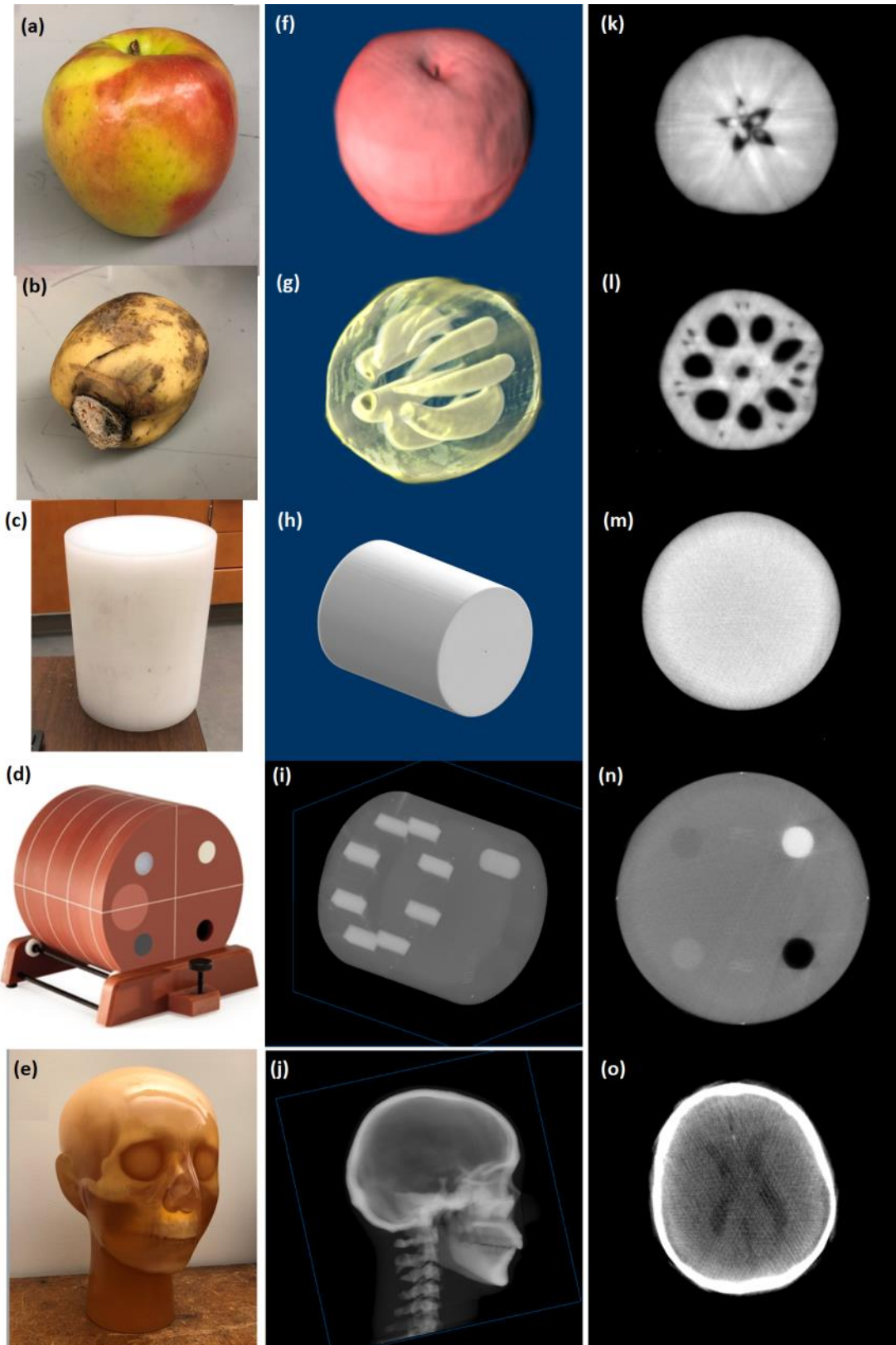
Figure 38: Various phantoms imaged with the s-HCT prototype along with their respective 3D renderings and axial slices.

5.3   Signal-Noise Ratio (SNR)

A common measure of image quality is the signal-to-noise ratio (SNR), or the mean pixel value divided by standard deviation (σ) over a given image area. In the final reconstructed axial image, many factors have influence on the final SNR, such as photon noise, detector noise, and number of reconstruction iterations. However, there can also be a limit on SNR imposed by the severity of configuration-based artifacts (such as gaps in detectors and/or source arrays), as well as artifacts due to mis-calibration. In ideal imaging scenarios, the photon noise is expected to dominate due to photon starvation (σ scales with $\sqrt{N}$). Accordingly, the SNR should also increase with the square root of the number of quanta interacting with the detector. With a detector resolution smaller than necessary, the relationship between effective 2D pixel size and the resulting 3D image SNR can be examined.

As illustrated in Figure 39a, each 2D detector pixel provides one data point to inform the 3D iterative reconstruction voxels. Detector binning is a common way to improve SNR in projection space (SNR_{2D}). However, binning too heavily will severely reduce the number of data points per voxel and degrade the 3D SNR (SNR_{3D}). For a fixed voxel size (0.5 x 0.5 x 0.5 mm^3), SNR_{3D} is also expected to increase with heavier binning on the 2D detector projection data. To observe this effect, a uniform density cylinder (16 cm diameter) of low-density polyethylene (LDPE) was used as the imaging object (Figure 38c). This object was chosen because it has a similar geometry and density to that of a human head, but with no features that could influence the SNR values, making the statistical analysis straightforward and uncontaminated with artifacts.
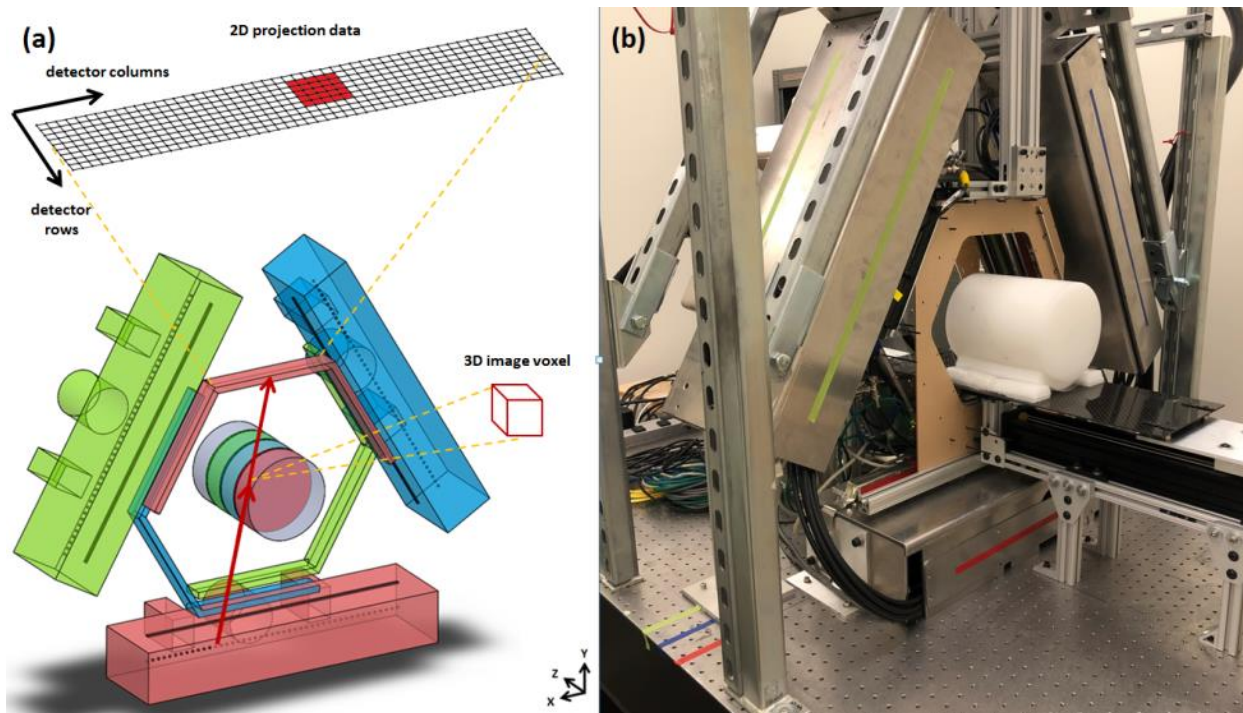
Figure 39: (a) Illustration of the 2D binning geometry relative to the 3D image space. By binning the detector data in 2D projection space, the SNR and spatial resolution of the reconstructed 3D data can be altered. (b) The 16 cm LDPE cylinder used for the SNR measurement.

5.3.1 SNR in projection space (SNR$_{2D}$)

First, the 2D detector projection data was checked to verify the behavior of SNR$_{2D}$ with varying x-ray exposure (Figure 40). The anode voltage was fixed at 120 kV, and all other imaging parameters were held constant except for the x-ray exposure time (t). As expected, at exposure times of 1, 2, and 3 ms (0.016, 0.032, and 0.048 mAs), the value of SNR$_{2D}$ increases linearly with $\sqrt{N}$.
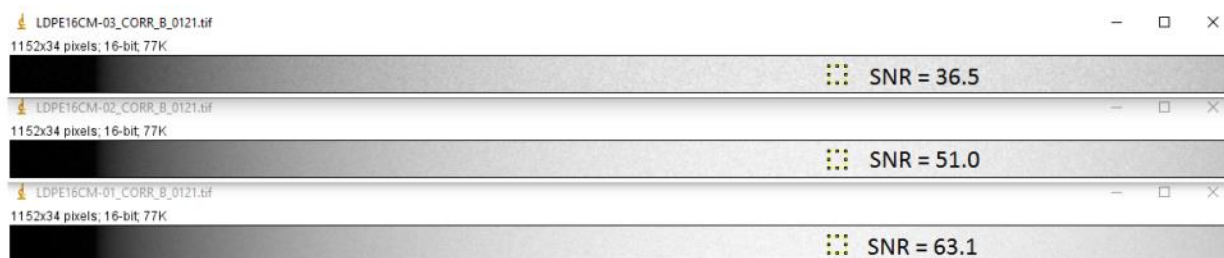
Figure 40: Sample projection data (dark and gain corrected) of the LDPE cylinder from one of the nine detectors in the s-HCT prototype. From top to bottom, the x-ray exposure time t = 1, 2, and 3 ms. The detector linearity is verified by the increase in SNR in proportion to the square root of the incoming photon count.

Next, the image with $t = 3$ ms was binned in an attempt to improve SNR_{2D} even more (Figure 41). This time, the value of SNR_{2D} is expected to improve linearly with the square root of the effective pixel size. For this simple test, binning values 1x1, 2x2, and 3x3 were used for effective pixel sizes 0.0004, 0.0016, and 0.0036 mm^2 respectively. The SNR did not improve as well as expected, indicating some diminishing returns in the usefulness of software binning. This is partially due to the effects of detector noise and dark current being more severe at small pixel size; a detector with physically larger pixel size or hardware binned pixels would be expected to have higher SNR than can be achieved through software averaging.
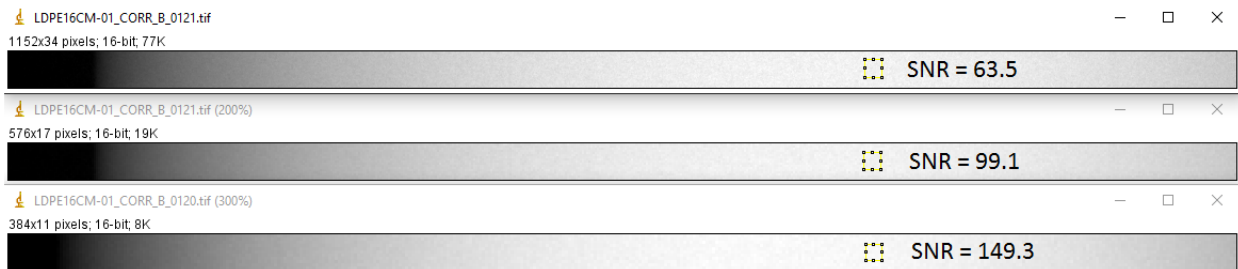
Figure 41: From the same 2D detector data in Figure 40, even higher SNR can be achieved through binning. From top to bottom: 1x1(unaltered), 2x2, and 3x3 binning.

5.3.2 SNR in image space (SNR_{3D})

The values of SNR_{2D} indicate the performance that should be expected from an ideal reconstruction in terms of SNR_{3D}. For a fixed voxel size (0.5 x 0.5 x 0.5 mm^3), SNR_{3D} is expected to increase linearly with the square root of the effective detector pixel size. According to the values plotted in Figure 42b, this principle holds true for 0.5 mm slice thickness, although the slope of this relationship differs depending on the direction of binning (higher SNR_{3D} gains from binning columns instead of rows). This effect is exaggerated even more when the data is binned to a more typical 2.5 mm slice thickness (Figure 42c). For example, a binning of 1x4 produces an SNR_{3D} of ~90, while 4x1 binning results in a SNR_{3D} of ~65.
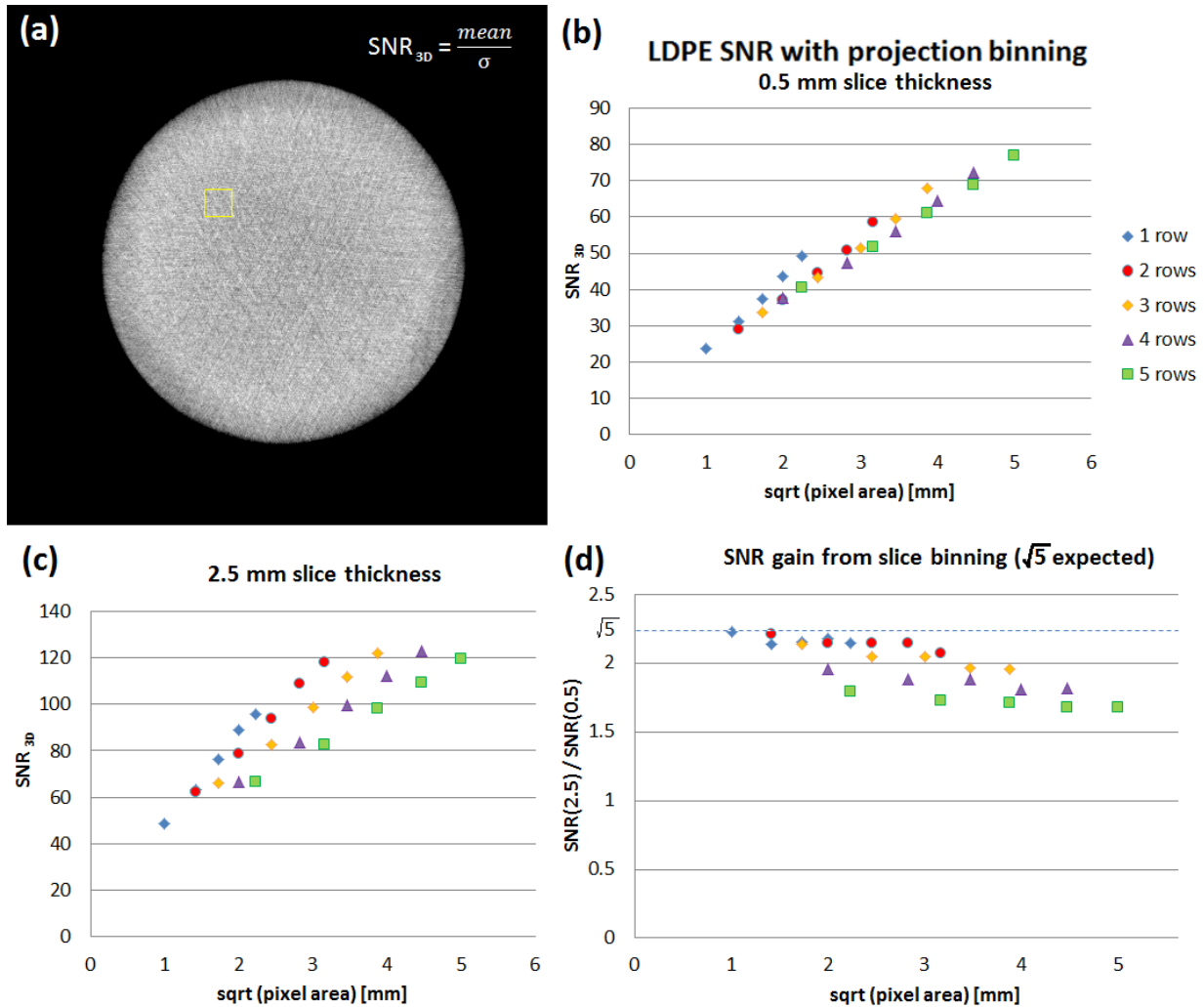
Figure 42: (a) Sample axial slice (0.5 mm) from the 3D recon of the LDPE cylinder with 2x2 detector binning ([-400 100] HU). (b)The SNR of the 3D image increases proportionally to the square root of the effective pixel area. (c) SNR_{3D} can also be increased by binning multiple slices in the z-dimension. (d) The ratio of the SNR_{3D} in 2.5mm slices vs. 0.5 mm slices suffers diminishing returns from binning of the projection data.

Increasing the voxel size by a factor of 5 is expected to produce a gain of $\sqrt{5}$ in the SNR_{3D}. This is true for the unaltered projection data (1x1) case, but binning of the 2D detector data produces diminishing returns beyond 2 or 3 pixels in either direction (Figure 42d). This is largely due to the similar effect seen in Figure 41, where the influence of other factors degrades the SNR. In the 2D case, the inherent detector noise plays a role; the value of SNR_{3D} is reflective of this effect as well as noise introduced by the reconstruction, object-scattered x-rays, and streak artifacts due to configuration or mis-calibration. Based

69

on these results, for a target slice thickness of 2.5 mm, row binning should be limited to only 1 or 2 rows. Perhaps more columns can be binned in the range 1-4; the system is capable of SNR > 100 with 2x4 binning. It has been shown that the image statistics improved in general as the detector pixels were binned to larger size. Of course, these improved values do not reflect the loss of spatial resolution associated with pixel binning.

5.4 Spatial Resolution

An important part of any CT scanner evaluation is a measure of the smallest details that can be visualized, or the intrinsic spatial resolution. Although the iterative reconstruction software can support the 0.5 x 0.5 x 0.5 mm^3 voxel size, the detection capability may be limited by the specifications of the hardware. The FSS was previously measured at 1,0 IEC, or ~ 1.2 mm in the direction orthogonal to the z-axis. With a detector pixel size about 5 times smaller, the FSS will clearly be the limiting factor. By imaging a very small (< 0.5 mm) object placed at the center, the magnification factor is ~1 and the intrinsic spatial resolution can be measured. For more qualitative assessment, other objects such as a 1mm steel bead

The spatial resolution of the s-HCT system was measured in the axial plane using the Modulation Transfer Function (MTF) applied to the 3D reconstruction of a 50 μm tungsten wire phantom. The taut wire was oriented parallel to the z-axis (within 2°) and scanned over a length of 10 cm. Reconstructed axial slices of the wire were used to define the oversampled line spread function (LSF), from which the MTF curve was calculated. The high resolution of the detector (0.2 x 0.2 mm^2) allows for selective pixel binning to improve SNR at the expense of spatial resolution; to demonstrate this effect, the reconstruction was performed with pixel binning (and effective pixel dimension) of 1 (0.2 mm), 2 (0.4 mm), 3 (0.6 mm), 4 (0.8 mm), and 5 (1.0 mm) for all detectors in the direction orthogonal to the z-axis. All detectors were binned in the row direction (parallel to the z-axis) by 2 rows (0.4 mm).

Other objects can provide a more direct measurement of spatial resolution. The ACR CT phantom Module 4, the high contrast spatial resolution segment, contains thick bar segments embedded within the

plastic to serve as literal line pairs. However, the ACR phantom and the tungsten wire phantom are only measuring in the axial plane; it may also be desirable to estimate the *z*-resolution as well. Because CT data is typically binned to thick slices (2-5 mm), this specification is not as critical. Nevertheless it can be estimated using a small metal object (1 mm bead) and demonstrated with a fine-tooth comb. The phantoms used for spatial resolution measurement are pictured in (Figure 43), along with their 3D renderings in ImageJ and a sample slice.
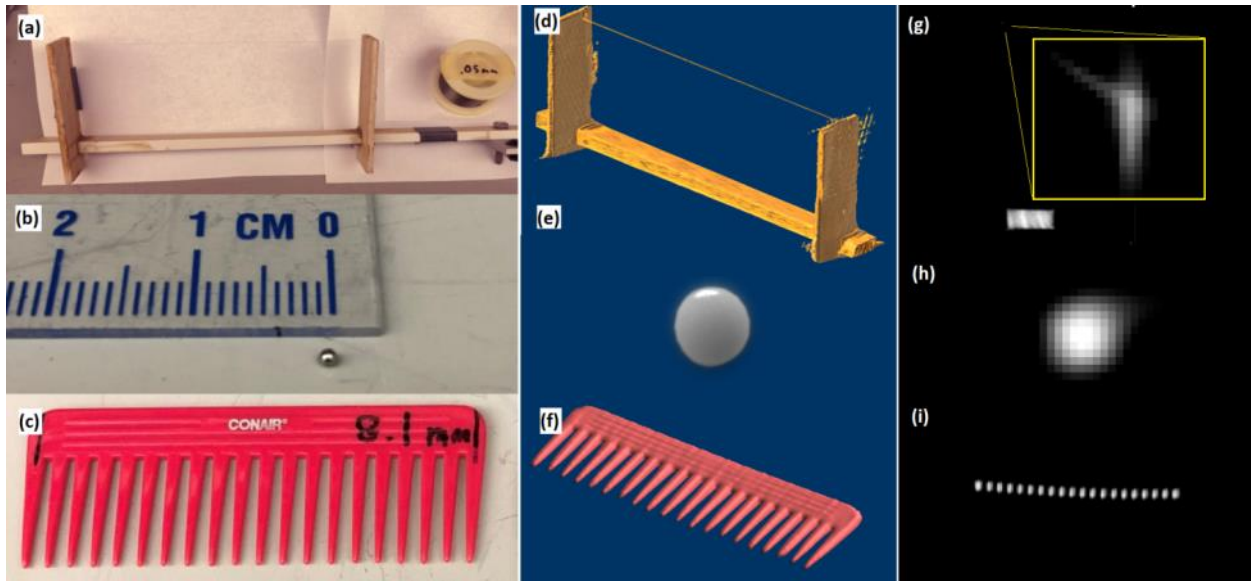
Figure 43: Various phantoms used for spatial resolution measurements. (a)Tungsten wire (0.05 mm) on a wooden frame. (b) 1 mm diameter steel bead. (c) Comb with plastic teeth at 8.1 mm pitch. (d-f) 3D renderings of the phantoms performed in ImageJ. (g) Axial slice (2.5 mm thickness) of the tungsten wire 3D data (0.125 x 0.125 mm^2 pixel size) (h) Coronal slice of the 1 mm steel bead ((0.125 x 0.125 mm^2 pixel size) (i) Sagittal slice along the teeth of the comb.

5.4.1 Tungsten wire MTF

The MTF of the LSF generated by axial reconstructions of a 50 um tungsten wire has been calculated with different detector binning and plotted in Figure 44. The reconstruction voxel size was drastically reduced (0.125 x 0.125 x 0.5 mm^3) to better capture the intrinsic resolution determined by the system hardware. At effective pixel size of 0.2, 0.4, 0.6, 0.8, and 1.0 mm, the 10% MTF values are 1.7, 1.4, 1.2, 1.0, and 0.9 lp/mm, respectively. These results are comparable to the expected intrinsic spatial resolution of ~ 1mm given the system geometry (particularly magnification), FSS, and detector pixel size.
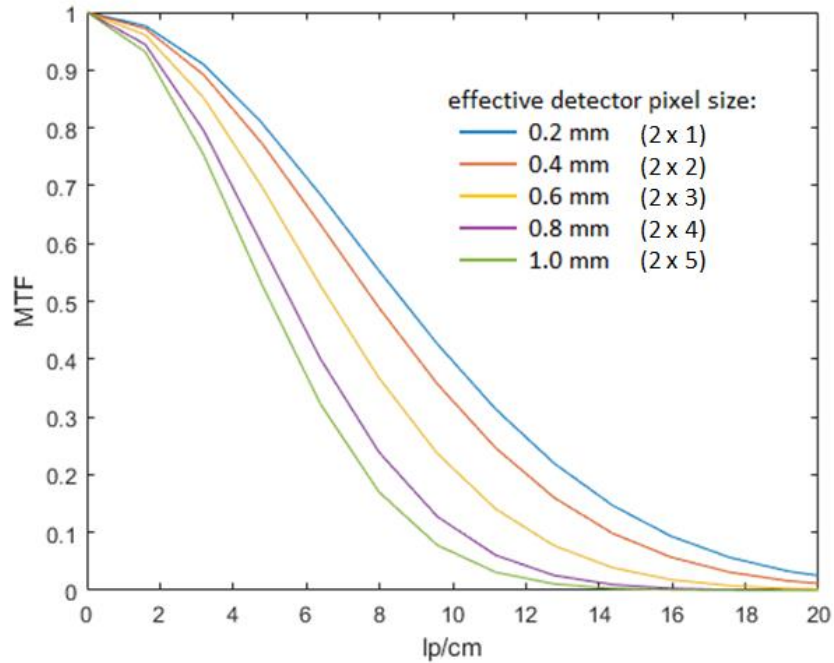
Figure 44: MTF calculated from the axial reconstruction images of a 50 um W wire with 0.125 x 0.125 mm resolution. The effective pixel size was adjusted via binning of the projection images.

5.4.2   ACR Module 4

The ACR CT phantom contains a more direct measure of spatial resolution embedded within Module 4. Figure 45 shows a sample reconstruction of the ACR CT 464 Phantom (Gammex) Module 04. The alignment accuracy of imaging planes and is noted through the capture of all 4 beads (1 mm diameter) on the perimeter of the cylinder. The spatial resolution for x and y can be visualized by zooming in on the bar patterns with a high window level. In generating the zoomed inset images, the reconstruction voxel size was altered from (0.5 x 0.5 x 2.5) to (0.125 x 0.125 x 2.5) mm^3 for better sampling of the bar patterns. The high resolution images of the segments containing 6 and 10 lp/cm are pictured in Figure 45b and Figure 45c respectively. In the accompanying line plots drawn perpendicular to the bar patterns, the ability to see 10 lp/cm confirms the sub-mm accuracy of the geometry calibration, and consequently the sub-mm resolution of the s-HCT prototype.
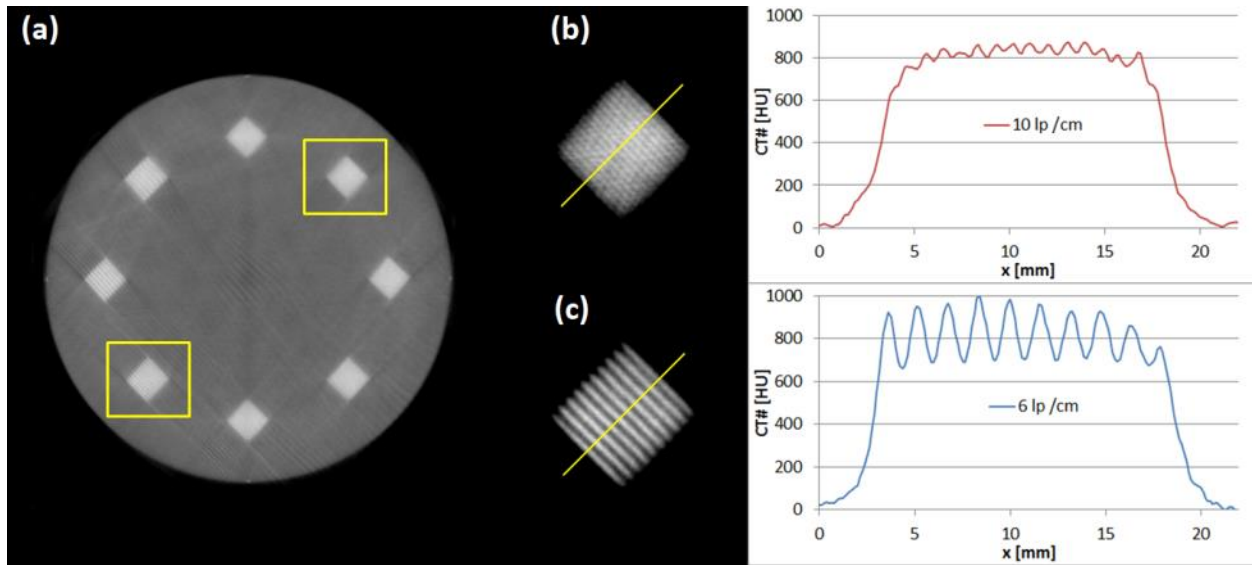
Figure 45: a) Reconstruction of the ACR CT phantom Module 4 taken with the s-HCT prototype ([-1000 1000] HU). Diagonal line profile plots of the (b) 10 and (c) 6 lp/cm bar patterns are visible when reconstructed at small voxel size (0.125 x 0.125 x 2.5 mm^3).

5.4.3   Other small objects

Because CT data is typically binned to thick slices (2-5 mm), the z-resolution is not as critical. Nevertheless, it can be estimated by imaging a small bead of 1mm diameter (Figure 43b).
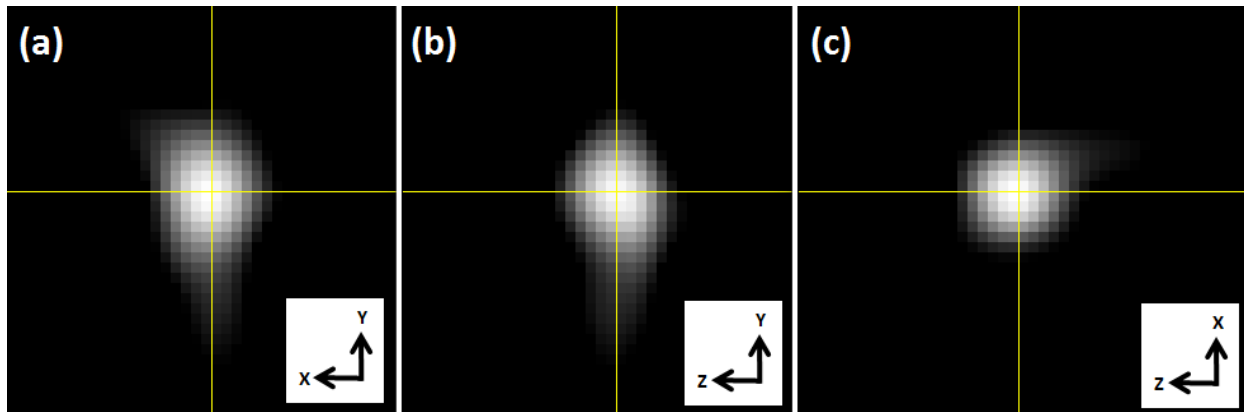
Figure 46: 3D image of a 1mm diameter steel bead reconstructed with 0.125 x 0.125 x 0.125 mm^3 voxel size.

As with the tungsten wire, the voxel size in the reconstruction output for such a small object was reduced by a factor of 4 to 0.125 x 0.125 x 0.125 mm^3. The resulting 3D image (Figure 46) confirms the sub-mm spatial resolution of the system, as well as the accuracy of the geometric calibration. The bead

should reconstruct as a sphere, but some distortion is visible at this scale. This distortion is evidently on the order of 3-4 pixels, or ~0.5 mm. These artifacts are regarded as an effect of mis-calibration rather than the system configuration; they could be reduced by further refinement of the calibration procedure.

5.5 CT number accuracy, uniformity, and linearity

Besides SNR and spatial resolution, another simple but important measure of image quality is that of the actual material density. Thus far, the attenuation values produced by the reconstruction have been unit-less; in the medical field CT images are displayed in Hounsfield Units (HU). The ACR CT 464 phantom Module 01 (Figure 47a) is commonly used to measure the accuracy of a scanner's HU output[113]. It contains 5 smaller cylinders of materials with known HU values for linear calibration of the system.
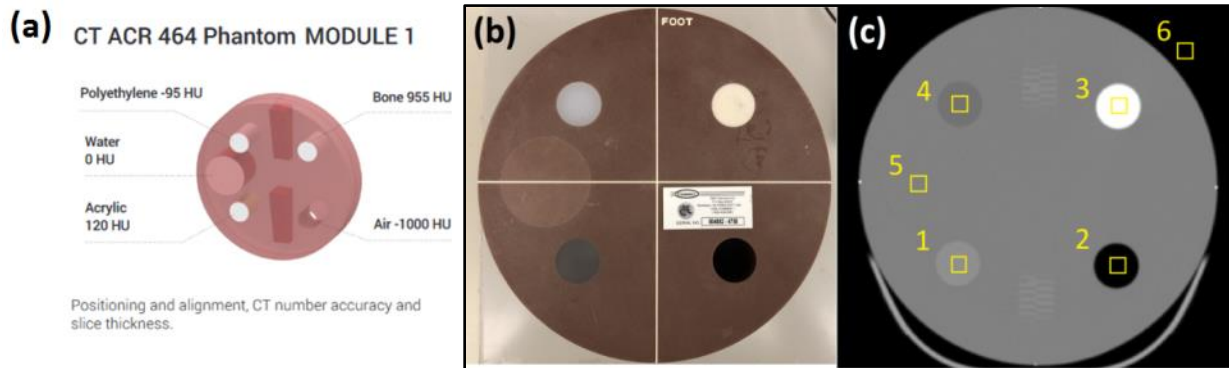
Figure 47: (a) ACR CT 464 Accreditation Phantom Module 0[113]1. (b) Photo of Module 01 (c) Sample image from clinical scanner with 6 16x16 pixel (8x8 mm) ROIs used for CT number accuracy analysis. Slice thickness measurement visible in center.

The s-HCT reconstruction outputs 16-bit integer values for each pixel in the 3D image. Using a 16 x 16 ROI centered on each material (Figure 47c), the mean values have been calibrated and converted to Hounsfield units (HU) using the nominal phantom values. The resulting linear fit is displayed in Figure 48. The window levels used for all figures in this study are determined using this calibration scale.
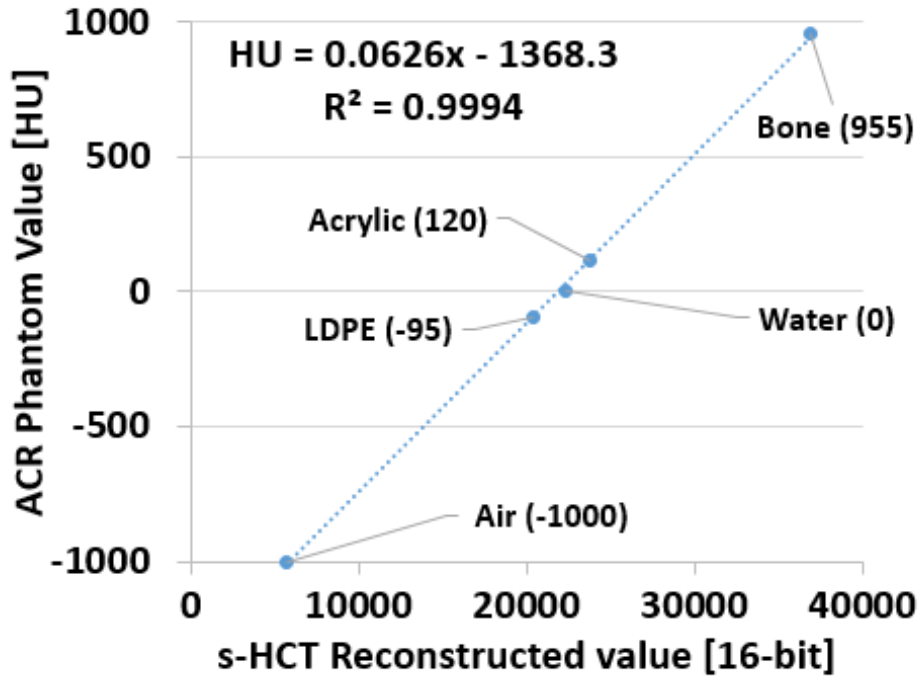
Figure 48: Calibration of the reconstructed 3D image pixel values in HU

In order to further compare the reconstructed images, the same phantom was scanned with the Ceretom (120 kVp, 14mAs) as well as a state-of-the-art clinical CT system (Siemens SOMATOM Force, 100 kVp, 398 mAs). Reconstruction was performed with the HR40 kernel at 2mm slice thickness and 0.5mm × 0.5mm pixel size. Table 4 displays the mean, standard deviation (σ), and signal-to-noise ratio (SNR) of the same 16 × 16 pixel ROIs evaluated in each of the 5 materials present in this phantom, for the s-HCT image as well as the clinical images.
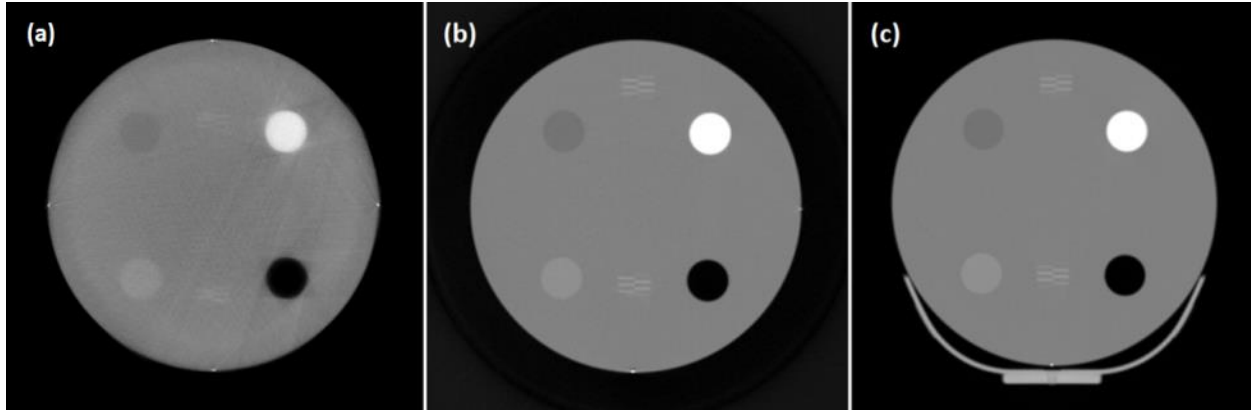
Figure 49: Axial reconstruction images of the ACR CT phantom Module 01 taken with the (a) s-HCT, (b) CereTom, and (c) SOMATOM Force scanners ([-1000 1000] HU).

The SNR of the s-HCT images in the range near 0 HU is 55. This is consistent with the SNR of 79 measured with the LDPE phantom; because the ACR phantom has nearly twice the volume, the transmitted photon count at the detector is much lower, resulting in higher noise in the projection data. Furthermore, some of the streak artifacts introduced by the non-uniform phantom structure also can degrade the SNR. Some of these streak artifacts may be removed by including correction for beam hardening in the reconstruction. Still other streaks may be caused by slight mis-calibration of the system geometry. Finally, the sharpness of the outer edge clearly is degraded along the perimeter at intervals spaced 120° apart; this is recognized as a fault of the incomplete sinogram coverage in these areas.

Table 4: Comparison of SNR values for the 5 materials in the ACR CT 464 phantom Module 01.

	CTDI$_{vol}$ [mGy]:	s-HCT (8.6)			Ceretom (41)			SOMATOM Force (53.6)		
ROI	**Material**	**Mean [HU]**	**σ**	**SNR**	**Mean [HU]**	**σ**	**SNR**	**Mean [HU]**	**σ**	**SNR**
1	Acrylic (120)	118.4	18.7	55.5	120.6	6.8	165.6	117.7	5.4	207.8
2	Air (-1000)	-1015.6	17.1	5.2	-990.6	5.4	1.7	-996.5	3.5	1.0
3	Bone (955)	936.3	28.0	75.5	1082.3	10.0	208.9	1052.8	7.1	287.6
4	LDPE (-95)	-91.3	21.4	47.9	-98.3	6.2	146.0	-101.6	3.5	257.0
5	Water(0)	15.2	23.0	55.5	4.6	7.3	137.9	1.1	3.8	262.0

The SNR in the Ceretom images is approximately 3 times higher than the same ROIs in the s-HCT image. This makes sense given that the $CDTI_{vol}$ for the Ceretom is roughly 5 times higher. With a higher imaging dose, the photon statistics improve and noise is reduced. While the scan parameters were designed to match the mAs for a routine low-dose adult head scan on the Ceretom, the measured dose at the isocenter can depend on other system specifics such as the SID, and also the beam HVL, both of which are higher for the s-HCT scanner.

5.6   Object-based Scatter

One of the factors influencing the image quality in any x-ray imaging system is the non-negligible quantity of x-rays which interacts with the object and scatters in a new direction, also known as Compton scattering. The effect of object-based scatter is to contaminate the true image projection with additional photons, artificially increasing the perceived transmission and thus lowering the calculated attenuation. Many efforts have been made to understand and correct for object scatter in a fan- or cone- beam imaging scenario with a single source[114-117]. One of the most effective solutions involves adding collimating plates on the detector face which only accept incoming rays originating at the source, also known as an anti-scatter grid. It is well known that stationary CT comes with a breadth of scatter-related issues that cannot be corrected by anti-scatter grids in the same fashion as traditional single-source CT.

The s-HCT prototype uses multiple imaging planes operating simultaneously, introducing a new source of scatter. In this section, scatter originating from other planes will be referred to as "cross-plane" scatter, a problem unique to multi-source systems. The term "in-plane" scatter refers to that which is confined to single source-detector pairs.

5.6.1   Cross-plane Scatter

One of the major drawbacks of the simultaneous multi-plane imaging configuration is the impact of scattered x-rays originating from the object in other planes. One of the design goals was to minimize the *z*-spacing between planes, which inadvertently increases the SPR related to this "cross-plane" scatter. Although the severity is largely dependent on the source activation sequence, the constantly integrating

nature of the flat panel detectors necessitates a hardware solution. One of the most effective ways of managing the cross-plane scatter is through collimation on the detector side.
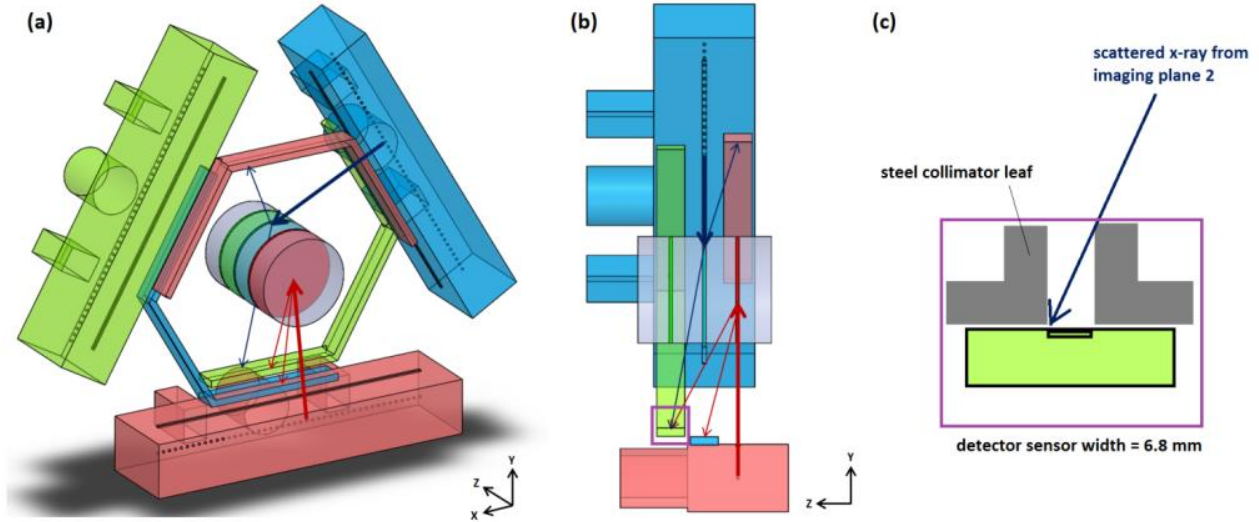
Figure 50: (a) Examples of cross-plane scatter originating at the object in all three imaging planes in the s-HCT configuration. (b) Seen from the x=0 plane, the object is approximated as a cylinder and the illuminated sections are treated as the source of unwanted scatter in the design for the detector collimators. Scatter from the object in Imaging plane 1 (red) contaminates the readings in Imaging planes 2 (blue) and 3 (green). (c) The addition of a collimator on the detector surface, shown in Imaging plane 3, blocks incoming scattered radiation from the object originating in other imaging planes.

The cross-plane scatter geometry is depicted in Figure 50a and Figure 50b. Given the detector width of 6.8 mm and the SID, a collimator can be installed on the detector face of sufficient height to block x-rays originating from the other imaging planes. The resulting design concept is shown in Figure 50c. The collimator leafs were fabricated according to this L-shaped design using 6.4 mm thick steel and installed on the faces of all detectors. In this demonstration, the angiographic CT head phantom (Kyoto Kagaku Co.,Ltd.) (Figure 38e) was scanned twice, once with detector side collimators and once without. The same imaging parameters were used in both scans to illustrate the effect of cross-plane scatter in the s-HCT configuration, and verify the performance of the new collimator design.
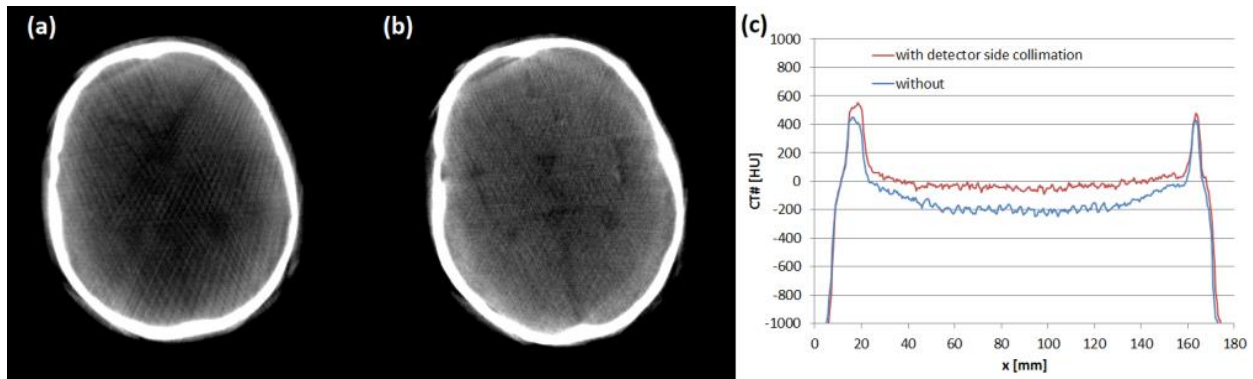
Figure 51: (a) Reconstructed axial slice of the Kyoto head phantom ([-200 200] HU) taken before the detector side collimators were installed. (b) The same slice from a dataset taken with collimation to block the cross-plane scatter. (c) Line profile plots demonstrating the reduction of the cupping artifact through use of detector side collimation (w = 7.0 mm)

3D reconstruction has been carried out for the Kyoto phantom and a sample slice is displayed in Figure 51b. In order to evaluate to effects of cross-plane scatter on the reconstruction, the detector-side collimator was removed for a duplicate scan. This image (Figure 51a) contains heavy streak artifacts introduced by contaminated projection data, rendering the image unusable. Furthermore, from the horizontal line profile in Figure 51c, the artificial attenuation reduction commonly associated with scatter (cupping artifact) is more apparent without collimation. The "cupping" artifact is a well-known issue in cone-beam CT caused by both beam hardening and scattered x-rays[118]. The introduction of detector-side collimation in the s-HCT system makes it possible to acquire data in multiple parallel imaging planes without any of these artifacts. This means that a wide variety of imaging sequences (such as with simultaneous acquisition of planes) can be used to acquire the same images in shorter cycle times, thus increasing temporal resolution.

5.6.2 In-plane Scatter

The "cupping" artifact mentioned previously can occur as a result of both cross-plane and in-plane scatter. While cross-plane scatter can be easily blocked by collimation, the in-plane scatter is mixed with the transmission projection data, requiring a series of collimators angled towards the source for scatter rejection. The s-HCT design aims to minimize the contribution due to scatter by using a very small cone

angle (~1 degree) and a small number of detector rows. This will eliminate many of the common cone-beam CT artifacts seen in multi-slice reconstructions[119] by reducing to a nearly true fan-beam (two-dimensional) shape. The thin cone beam is also necessary for the multi-plane architecture; one of the design goals was to minimize the z-spacing between planes. As a final consideration, in a system with 3 detector arrays, a small z-dimension will reduce the final cost of the system/detectors when compared to larger flat panel arrays.

Figure 52 displays the adjustable collimator leaf design for reduction of the beam width in the z-direction. At the given distances from the focal spot, an opening of $w = 1.6$ mm results in a beam thickness of 5.8 mm at the isocenter and 9.3 mm at the detector. The detector has a height of $h = 6.8$ mm. These dimensions are for the center source and center detector only, and are not constant for all sources. The opening of $w = 1.6$ mm allows for > 5 mm x-ray coverage in z from all source positions. The effect of this collimator on the s-HCT images can be most dramatically visualized using a large round object; in this case a cylinder of water 23 cm in diameter.
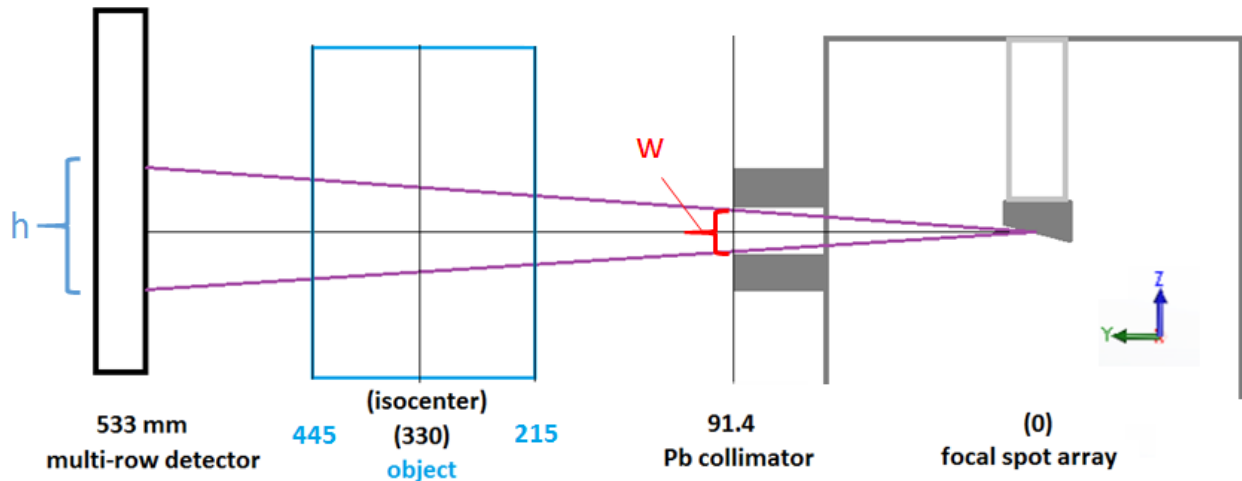
Figure 52: Dimensions of the collimated x-ray beam along the sagittal plane. The top and bottom leafs can be adjusted to provide a cone angle up to 4°. All dimensions referenced from the center focal spot in mm.

Images of the 23 cm water cylinder were acquired to evaluate the imaging performance of the s-HCT system. Scan parameters were 120kVp, with 12.0 mA anode current and 6.5 mAs x-ray exposure

(total). Figure 53a shows a sample image of a 23cm diameter cylinder of water generated by the benchtop system with 3 scans, rotating the object in 120° steps. In order to evaluate to effects of scatter on the reconstruction, the collimator was removed for a duplicate scan. Line profiles of the axial slice for both images are presented in Figure 53b. The cupping artifact is effectively reduced using a z-collimation of $w = 1.7$mm.
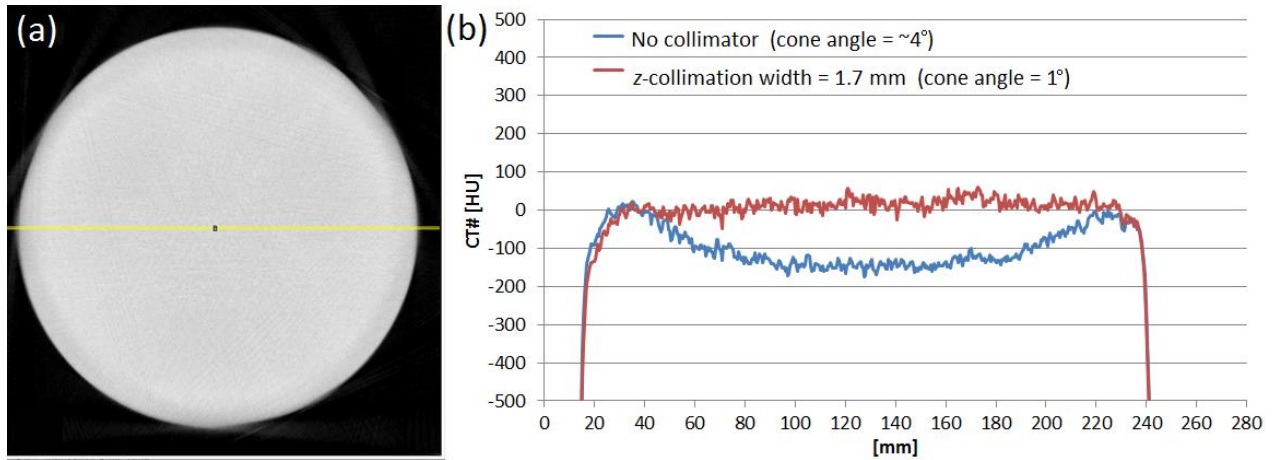
Figure 53: (a) Reconstructed axial slice of the 23 cm water cylinder ([-1000 200] HU). (b) Line profile plots demonstrating the removal of the "cupping" artifact through use of z-collimation (w = 1.7 mm)

The s-HCT benchtop setup was used to demonstrate a reduction of the in-plane scatter contribution by collimating to a very small cone angle (~1 degree) and a small number of detector rows. This source-side collimator has been shown to reduce the cupping artifact by reducing to approximation nearly 2D fan beam.

Although the beam is collimated to a cone angle of 1° (effectively eliminating cone-beam scatter), the illuminated object volume emits scattered photons in all directions, including within the fan beam. One of the primary arguments against pursuing s-CT research is the inability to resolve this in-plane scatter issue through a hardware solution.

CHAPTER 6: CONCLUSION AND FUTURE OUTLOOK

A prototype s-HCT scanner has been constructed with 3 CNT x-ray source arrays and 3 opposing detector arrays. Using in-house developed iterative reconstruction and calibration methods, initial CT imaging results have demonstrated the potential for reduced cycle times among other natural advantages of s-CT in general. The present system provides a valuable data point in the study of CT architectures, and can potentially serve as a testing platform for further experiments in s-CT research. As a final thought to the evaluation of the system, this chapter further weighs the pros and cons of s-CT, and also gives a few potential improvements for the next prototype.

6.1 Discussion

The advantages of s-CT over rotating source architectures are numerous. A lower degree of system complexity results in a reduced need for maintenance and routine calibrations. Smaller physical footprint also increases portability. The advantage highlighted in this study is the programming flexibility of the acquisition schemes and cycle time (T). Systems with a single moving source are limited to the sequential acquisition of views along the time-dependent focal spot path (as in helical CT), and T is typically limited by the rotation speed of the gantry. The s-HCT system can be programmed to deliver the same imaging dose in a variety of different sequences, opening the door to new scanning possibilities, such as non-sequential or simultaneous projection acquisition sequences which have much shorter T. Views can also be omitted from the scan to decrease cycle time (increasing scanning speed) at the cost of image quality. Looking to the future, the usefulness of this ability will depend on the development of sparse-view CT through iterative reconstruction and deep learning.

The prominence of CT in medical imaging has driven the need for large-bore systems that can accommodate the human torso. This places a large power demand on the x-ray source due to the large

(>1 m) distance from source to detector, requiring rotating anode(s) and oil cooling. Combined with the power supplies, rotating gantry (and related counterweighting), CT scanners are notoriously complex. The prototype s-HCT scanner is designed for a smaller FOV (~20 cm diameter) and as a result can generate sufficient x-ray dosage within the limits of a stationary target. Using multiple source arrays provides unique advantages such as achieving higher system power through simultaneous exposures. A final advantage is that the focal spots can be turned on in any order to distribute the heat load as evenly as possible and maximize x-ray flux from the x-ray targets.

The multi-plane imaging aspect of the system configuration combined with the thin cone beam geometry presents the need for z-translation of the object, a concept which is at odds with the "stationary" system concept. In this sense, only the sources and detectors are stationary. While many CBCT imaging systems with large area detectors can acquire 3D data with no object translation, most volumetric data acquisition processes involve translation of the object in some way. The reconstructed image of the Kyoto phantom (Figure 51b) shows that no artifacts arise from the use of a multi-plane imaging configuration.

The use of moving sources introduces a slight artificial enlargement of the FSS through motion blurring. While minimal compared to patient motion, the focal spots in s-CT are not subject to this effect. In rotation-based systems, this effect has been minimized through the use of microsecond exposure times, made possible by high-current rotating anode technology. This concept could be applied to linear source arrays in the long term to overcome the power limitations of stationary anodes. Ultimately, the future of high power s-CT systems could very well follow the path of developing advanced HV anode technologies, such as rotating rod[92] and HV liquid metal jet[120].

It is well known that s-CT comes with its disadvantages as well. Reports have been made regarding the high degree of difficulty in calibrating s-CT systems involving many source-detector pairs[26]. Although calibration methods have been developed, many are system-specific and still require customization. For the s-HCT prototype, sub-mm calibration accuracy has been achieved using an in-house developed method[11], and confirmed by the tungsten wire MTF.

Aside from the obvious added complexity of calibrating many sources and detectors, the other major disadvantage of s-CT in general is the lack of capability for anti-scatter hardware. The inability to resolve the in-plane scatter issue through a hardware solution is one of the primary arguments against pursuing s-CT in general. This issue is partially addressed in the current prototype by collimating the beams to a cone angle of ~1° for dramatic reduction of scatter in the z direction. The apparent tradeoff is that with such a narrow beam, fewer detector rows can be acquired per cycle, slowing the ultimate scanning speed. The multi-plane aspect of the s-HCT prototype allows the translation speed to be recovered through simultaneous projection acquisition, a process which introduces a new source of scatter. This "cross-plane" scatter, typically a major issue in general for s-CT, is also solved by narrow collimation in the z dimension on the detector side.

The results presented in Chapter 5 indicate that the s-HCT system can perform as well or better than the Ceretom in the areas of temporal and spatial resolution, but falls short of matching the total x-ray exposure and SNR of the clinical scanners (Figure 49, Table 4). While this is a shortcoming of the present prototype, it is not a fundamental limitation of s-HCT. By further optimization of the source and detector, the dose and resulting image SNR can be optimized.

6.2 System Improvements

The current iteration of the s-HCT system is certainly not the most ideal configuration. Rather, it is the optimal arrangement given the availability of existing components. The major system hardware components (x-ray sources and detectors) as well as the image processing software could be further developed or customized for improvements in image quality. The following specific improvements to the hardware have been identified for the next version of the s-HCT scanner.

6.2.1 Source array length and pitch
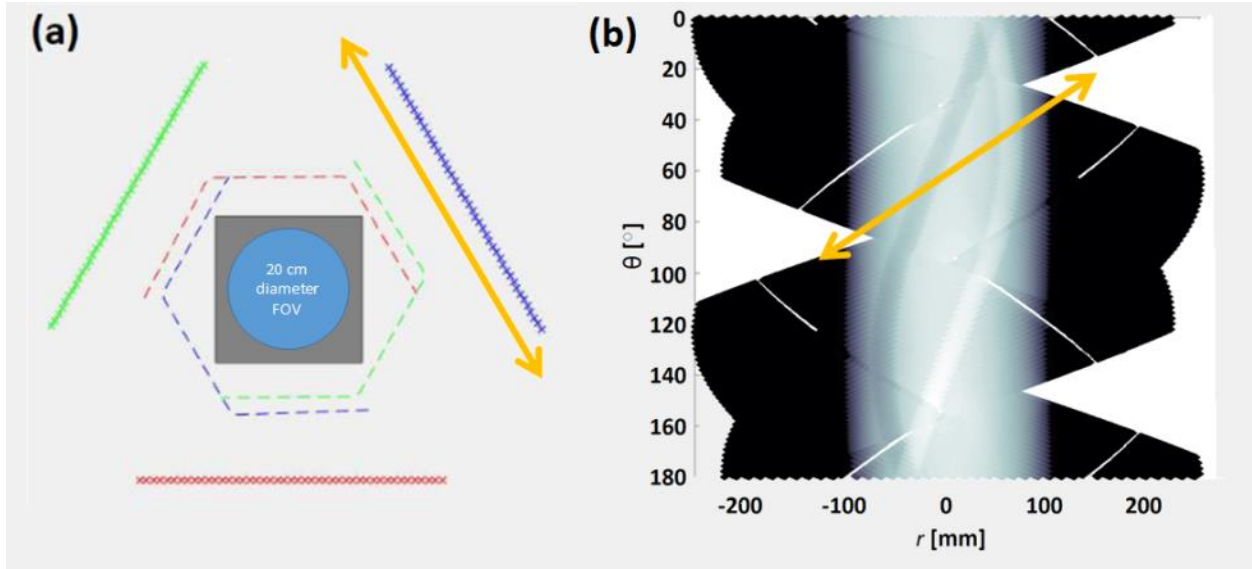
Figure 54: (a) s-HCT system geometry with suggested increase of the source array length. (b) The addition of more sources would expand the sinogram coverage to accommodate a larger FOV.

The existing source array is 528 mm in length. A longer source array would improve the gaps in coverage as indicated by the sinogram plot (Figure 54). This would allow for a wider FOV with "complete" angular coverage. However, for the ~20 cm FOV in s-HCT, the length may be sufficient for imaging inside the head if precise details along the perimeter are not required. The overall image quality may benefit more from a smaller pitch from focal spot to focal spot. The existing array has a pitch of 12 mm. As described in section 4.1, this produces 45 views with an angular range of 77° [-38.7 38.7]°, suggesting an average angular resolution of 1 view every 1.75°. The low density of views may be responsible for some streak artifacts, confirmed by simulation. Other CNT x-ray sources have been used which feature a 4 mm pitch; this would be much more ideal for reduction of those artifacts, leading to gains in SNR. Even a reduction in pitch to 8 mm would provide nearly 1 view per 1.2° and increase the total number of views of the system to ~200. It is estimated that with higher angular resolution, the SNR would be improved even with the total exposure normalized (lower mA per beam).

6.2.2   Detector Continuity

The detector portion of the s-HCT hardware could also be improved, and currently is the bottleneck for achieving better performance with the given configuration of source arrays. The first major issue with the current assembly is the presence of gaps (~5-6 mm) between detector modules. This gap is too large to fix through interpolation, and also produces noticeable regions of missing data in the sinogram plot (Figure 54b). Customization of a detector geometry with minimal gaps between modules would reduce the appearance of streaks associated with the detector gaps.

6.2.3   Detector Dynamic Range
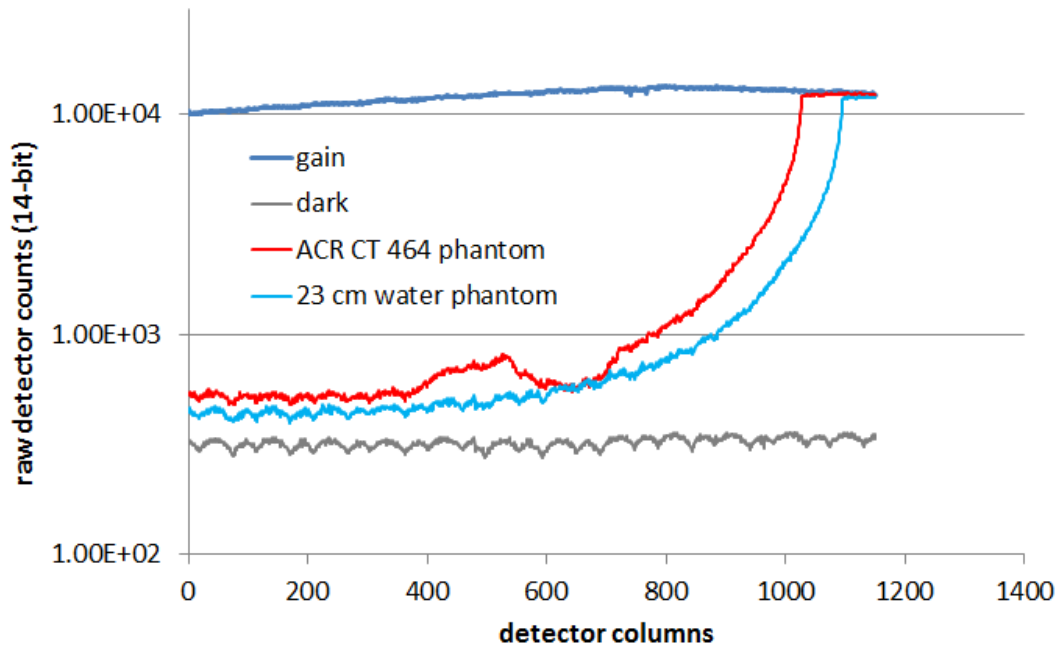
Figure 55: Line plots of the raw detector data (imaging plane 1, source #15, detector B). For large phantoms, the transmitted photon count is less than the detector dark current, indicating photon starvation at the detector.

As previously mentioned, the s-HCT is limited in the total x-ray dose used per scan. However, this is not a limitation of the source, but in the dynamic range of the detectors. The existing CsI indirect detectors are only capable of 14-bit range, or ~16000 maximum detector counts. The total range of detection is illustrated by the line plots in Figure 55. With inherent detector noise on the order of ~100 counts, this only provides 2 orders of magnitude from the dark image to flat field. In the case of large (>

20 cm diameter) phantoms, the signal reaching the detector is severely limited. The total SNR of the reconstructed image is highly dependent on the SNR at this range where the transmitted photon count is low. However, if the x-ray exposure is increased, the flat field image will saturate at 14-bit.

Higher dynamic range of the detector arrays would allow for longer x-ray exposures to increase the scanning mAs, resulting in higher SNR at the cost of scanning speed. It is estimated that 16-bit would be more appropriate for this application. Full-body CT scanners typically use 18-bit dynamic range.

6.2.4   Detector Width

The existing configuration could allow for more detector rows. This would provide more z-coverage of the object up to a cone angle of 4°, allowing for an increase in object translation speed at the cost of adding scatter and other artifacts associated with CBCT. Finally, at high scanning speeds, the afterglow effect plays a more significant role; a detector scintillator material should be chosen that is well suited for high speed imaging with quick decay time.

REFERENCES

1. Hsieh J. *Computed tomography : principles, design, artifacts, and recent advances.* Third edition. ed. Bellingham, Washington, USA: SPIE; 2015.

2. Kalender WA. X-ray computed tomography. *Phys Med Biol.* 2006;51(13):R29-43.

3. Shefer E, Altman A, Behling R, et al. State of the art of CT detectors and sources: a literature review. *Current Radiology Reports.* 2013;1(1):76-91.

4. Qian X, Tucker A, Gidcumb E, et al. High resolution stationary digital breast tomosynthesis using distributed carbon nanotube x-ray source array. *Med Phys.* 2012;39(4):2090-2099.

5. Inscoe CR, Platin E, Mauriello SM, et al. Characterization and preliminary imaging evaluation of a clinical prototype stationary intraoral tomosynthesis system. *Med Phys.* 2018;45(11):5172-5185.

6. Gunnell ET, Franceschi DK, Inscoe CR, et al. Initial clinical evaluation of stationary digital chest tomosynthesis in adult patients with cystic fibrosis. *Eur Radiol.* 2019;29(4):1665-1673.

7. Inscoe CR, Lee Y, Billingsley AJ, et al. Point-of-Care Tomosynthesis Imaging of the Wrist. *Mil Med.* 2021;186(Suppl 1):745-750.

8. Luo Y, Spronk D, Lee Y, Zhou O, Lu J. Simulation and optimization of system configuration for the stationary head CT using CNT x-ray source array: reconstruction and quality evaluation. Vol 11312: SPIE; 2020.

9. Luo Y, Spronk D, Inscoe CR, Lee Y, Zhou O, Lu J. Stationary head CT with linear CNT x-ray source arrays: image quality assessment through simulation. Paper presented at: Medical Imaging 2021: Physics of Medical Imaging2021.

10. Spronk D, Luo Y, Inscoe C, et al. Feasibility of a stationary head CT scanner using a CNT x-ray source array. Vol 11312: SPIE; 2020.

11. Spronk D, Luo Y, Inscoe CR, Zhou O, Lu J, Lee YZ. Stationary head CT scanner using CNT x-ray source arrays. Paper presented at: Medical Imaging 2021: Physics of Medical Imaging2021.

12. Spronk D, Luo Y, Inscoe CR, Lee YZ, Lu J, Zhou O. Evaluation of carbon nanotube x-ray source array for stationary head computed tomography. *Med Phys.* 2020.

13. Radon J. On the determination of functions from their integrals along certain manifolds. *Ber Verh, Sachs Akad Wiss.* 1917;69:262-277.

14. Oldendorf WH. Isolated flying spot detection of radiodensity dis-continuities-displaying the internal structural pattern of a complex object. *IRE transactions on bio-medical electronics.* 1961;8(1):68-72.

15. Cormack AM. Representation of a function by its line integrals, with some radiological applications. *Journal of applied physics.* 1963;34(9):2722-2727.

16. Bracewell RN, Riddle A. Inversion of fan-beam scans in radio astronomy. *The Astrophysical Journal.* 1967;150:427.

17. Ambrose J, Housfield G. Computerized Axial Tomography. Paper presented at: Invitational paper presented at the North American Radiological Society Meeting Chicago1972.

18. Rincon-Guio C. The role of computed tomography as a prognostic tool in traumatic brain trauma. *Hospital.* 1971.

19. Hounsfield GN. Computerized transverse axial scanning (tomography). 1. Description of system. *Br J Radiol.* 1973;46(552):1016-1022.

20. Mori I, Saito K, Asahina K. Whole-body x-ray CT scanner, TCT-900S. *Toshiba Rebyu.* 1987;42(2):80-82.

21. Yaffe M, Rowlands J. X-ray detectors for digital radiography. *Physics in Medicine & Biology.* 1997;42(1):1.

22. Schardt P, Deuringer J, Freudenberger J, et al. New x-ray tube performance in computed tomography by introducing the rotating envelope tube technology. *Medical physics.* 2004;31(9):2699-2706.

23. Flohr TG, McCollough CH, Bruder H, et al. First performance evaluation of a dual-source CT (DSCT) system. *European radiology.* 2006;16(2):256-268.

24. Baek J, De Man B, Uribe J, et al. A multi-source inverse-geometry CT system: initial results with an 8 spot x-ray source array. *Physics in Medicine & Biology.* 2014;59(5):1189.

25. FitzGerald P, Bennett J, Carr J, et al. Cardiac CT: A system architecture study. *J Xray Sci Technol.* 2016;24(1):43-65.

26. FitzGerald P, Edic P, Gao H, et al. Quest for the ultimate cardiac CT scanner. *Med Phys.* 2017;44(9):4506-4524.

27. De Man B, Basu S, Fitzgerald P, et al. Inverse geometry CT: The next-generation CT architecture? Paper presented at: 2007 IEEE Nuclear Science Symposium Conference Record2007.

28. De Man B, Uribe J, Baek J, et al. Multisource inverse-geometry CT. Part I. System concept and development. *Medical physics.* 2016;43(8Part1):4607-4616.

29. John S, Stock S, Cerejo R, et al. Brain Imaging Using Mobile CT: Current Status and Future Prospects. *J Neuroimaging.* 2016;26(1):5-15.

30. Robb RA, Hoffman EA, Sinak LJ, Harris LD, Ritman EL. High-speed three-dimensional X-ray computed tomography: The dynamic spatial reconstructor. *Proceedings of the IEEE.* 1983;71(3):308-319.

31. Boyd DP, Couch JL, Napel SA, et al. High-speed, multi-slice, x-ray computed tomography. Paper presented at: Physics and Engineering in Medical Imaging1982.

32. Cao H, Yunxiang L, Chang T, Cui Z, Zheng H. Stationary real time ct imaging system and method thereof. In: Google Patents; 2017.

33. Weisser G, Lehmann KJ, Scheck R, Coppenrath E, Georgi M. Dose and image quality of electron-beam CT compared with spiral CT. *Invest Radiol.* 1999;34(6):415-420.

34.   De Man B, Basu S, Bequé D, et al. Multi-source inverse geometry CT: a new system concept for x-ray computed tomography. Vol 6510: SPIE; 2007.

35.   Solomon E, Wilfley B, Van Lysel M, Joseph A, Heanue J. Scanning-beam digital x-ray (SBDX) system for cardiac angiography. Vol 3659: SPIE; 1999.

36.   Zhang J, Yang G, Cheng Y, et al. Stationary scanning x-ray source based on carbon nanotube field emitters. *Applied Physics Letters.* 2005;86(18):184104.

37.   Neculaes VB, Caiafa A, Cao Y, et al. Multisource inverse-geometry CT. Part II. X-ray source design and prototype. *Med Phys.* 2016;43(8):4617.

38.   Schwoebel PR, Boone JM, Shao J. Studies of a prototype linear stationary x-ray source for tomosynthesis imaging. *Phys Med Biol.* 2014;59(10):2393-2413.

39.   Gonzales B, Spronk D, Cheng Y, et al. Rectangular fixed-gantry CT prototype: combining CNT X-ray sources and accelerated compressed sensing-based reconstruction. *IEEE Access.* 2014;2:971-981.

40.   Iijima S, Ichihashi T. Single-shell carbon nanotubes of 1-nm diameter. *nature.* 1993;363(6430):603-605.

41.   Venkataraman A, Amadi EV, Chen Y, Papadopoulos C. Carbon nanotube assembly and integration for applications. *Nanoscale research letters.* 2019;14(1):1-47.

42.   Chernozatonskii L, Gulyaev YV, Kosakovskaja ZJ, et al. Electron field emission from nanofilament carbon films. *Chemical Physics Letters.* 1995;233(1-2):63-68.

43.   Sugie H, Tanemura M, Filip V, Iwata K, Takahashi K, Okuyama F. Carbon nanotubes as electron source in an x-ray tube. *Applied physics letters.* 2001;78(17):2578-2580.

44.   Thomson JJ. The roentgen rays. *Nature.* 1896;53(1374):391-392.

45.   Bushong SC, Facmp SF. *Radiologic Science for Technologists E-Book: Physics, Biology, and Protection.* Mosby; 2020.

46.   Coolidge W. The development of modern roentgen-ray generating apparatus. *Am J Roentgenology.* 1930;24:605-620.

47.   Brodie I, Spindt C. Vacuum microelectronics. *Advances in electronics and electron physics.* 1992;83:1-106.

48.   Knight LV, Pew HK, Reyes A, Liu H. Field emission x-ray tube for mammography. Paper presented at: Biomedical Photonics and Optoelectronic Imaging2000.

49.   Rangsten P, Ribbing C, Strandman C, Hök B, Smith L. Field-emitting structures intended for a miniature X-ray source. *Sensors and Actuators A: Physical.* 2000;82(1-3):24-29.

50.   Baptist R. X-ray tube comprising an electron source with microtips and magnetic guiding means. In: Google Patents; 2001.

51.   Spindt C, Holland C, Schwoebel P, Brodie I. Field-emitter-array development for microwave applications. *Journal of Vacuum Science & Technology B: Microelectronics and Nanometer Structures Processing, Measurement, and Phenomena.* 1996;14(3):1986-1989.

52. Gaertner G, Knapp W. Spindt Cathodes and Other Field Emitter Arrays. *Modern Developments in Vacuum Electron Sources.* 2020:547-579.

53. Cao X, Zhang G, Zhao Y, et al. Fully vacuum-sealed addressable nanowire cold cathode flat-panel X-ray source. *Applied Physics Letters.* 2021;119(5):053501.

54. Yue G, Qiu Q, Gao B, et al. Generation of continuous and pulsed diagnostic imaging x-ray radiation using a carbon-nanotube-based field-emission cathode. *Applied Physics Letters.* 2002;81(2):355-357.

55. Cheng Y, Zhang J, Lee Y, et al. Dynamic radiography using a carbon-nanotube-based field-emission x-ray source. *Review of scientific instruments.* 2004;75(10):3264-3267.

56. Zhou OZ, Lu J. X-ray generating mechanism using electron field emission cathode. In: Google Patents; 2005.

57. Zhang J, Cheng Y, Lee Y, et al. A nanotube-based field emission x-ray source for microcomputed tomography. *Review of scientific instruments.* 2005;76(9):094301.

58. Cao G, Lee YZ, Peng R, et al. A dynamic micro-CT scanner based on a carbon nanotube field emission x-ray source. *Phys Med Biol.* 2009;54(8):2323-2340.

59. Cao G, Burk LM, Lee YZ, et al. Prospective-gated cardiac micro-CT imaging of free-breathing mice using carbon nanotube field emission x-ray. *Med Phys.* 2010;37(10):5306-5312.

60. Grant DG. Tomosynthesis: a three-dimensional radiographic imaging technique. *IEEE Transactions on Biomedical Engineering.* 1972(1):20-28.

61. Niklason LT, Christian BT, Niklason LE, et al. Digital tomosynthesis in breast imaging. *Radiology.* 1997;205(2):399-406.

62. Park JM, Franken Jr EA, Garg M, Fajardo LL, Niklason LT. Breast tomosynthesis: present considerations and future applications. *Radiographics.* 2007;27(suppl_1):S231-S240.

63. Zhou O, Calderon-Colon X, Saito Y. Carbon nanotube-based field emission X-ray technology. In: *Carbon Nanotube and Related Field Emitters: Fundamentals and Applications.* Wiley; 2010:417-438.

64. Rigauts H, Marchal G, Baert AL, Hupke R. Initial experience with volume CT scanning. *J Comput Assist Tomogr.* 1990;14(4):675-682.

65. Rumboldt Z, Huda W, All JW. Review of portable CT with assessment of a dedicated head CT scanner. *AJNR Am J Neuroradiol.* 2009;30(9):1630-1636.

66. Samson K. A Mobile Stroke CT Unit Cuts tPA Administration Times By One-Third: Would It Work in the US? *Neurology Today.* 2012;12(24):1-16.

67. Walter S, Kostpopoulos P, Haass A, et al. Bringing the hospital to the patient: first treatment of stroke patients at the emergency site. *PLoS One.* 2010;5(10):e13758.

68. Weber JE, Ebinger M, Rozanski M, et al. Prehospital thrombolysis in acute stroke: results of the PHANTOM-S pilot study. *Neurology.* 2013;80(2):163-168.

69. Virani SS, Alonso A, Benjamin EJ, et al. Heart Disease and Stroke Statistics-2020 Update: A Report From the American Heart Association. *Circulation.* 2020;141(9):e139-e596.

70. Peterson AB, Xu L, Daugherty J, Breiding MJ. Surveillance report of traumatic brain injury-related emergency department visits, hospitalizations, and deaths, United States, 2014. 2019.

71. Carlson AP. The benefits of a portable head CT scanner. 2011.

72. Gunnarsson T, Theodorsson A, Karlsson P, et al. Mobile computerized tomography scanning in the neurosurgery intensive care unit: increase in patient safety and reduction of staff workload. *J Neurosurg.* 2000;93(3):432-436.

73. Gunnarsson T, Hillman J. Clinical usefulness of bedside intracranial morphological monitoring: mobile computerized tomography in the neurosurgery intensive care unit. Report of three cases. *Neurosurg Focus.* 2000;9(5):e5.

74. Carlson AP, Phelps J, Yonas H. Alterations in surgical plan based on intraoperative portable head computed tomography imaging. *J Neuroimaging.* 2012;22(4):324-328.

75. Robb RA, Lent AH, Gilbert BK, Chu A. The dynamic spatial reconstructor: a computed tomography system for high-speed simultaneous scanning of multiple cross sections of the heart. *J Med Syst.* 1980;4(2):253-288.

76. Budoff MJ, Shinbane JS. *Cardiac CT imaging: diagnosis of cardiovascular disease.* Springer; 2016.

77. Krauss B, Schmidt B, Flohr TG. Dual source CT. In: *Dual energy CT in clinical practice.* Springer; 2011:11-20.

78. Gong C, Zeng L, Wang C, Ran L. Design and Simulation Study of a CNT-Based Multisource Cubical CT System for Dynamic Objects. *Scanning.* 2018;2018:6985698.

79. Duan Y, Cheng H, Wang K, Mou X. A Novel Stationary CT Scheme Based on High-Density X-Ray Sources Device. *IEEE Access.* 2020;8:112910-112921.

80. Zhang T, Xing Y, Zhang L, Jin X, Gao H, Chen Z. Stationary computed tomography with source and detector in linear symmetric geometry: Direct filtered backprojection reconstruction. *Medical physics.* 2020;47(5):2222-2236.

81. Yang Q, Gjesteby L, Cong W, et al. "Trinity" CT Architecture–A Stationary CT System.

82. Yao Y, Li L, Chen Z. A Novel Static CT System: The Design of Triple Planes CT and its Multi-Energy Simulation Results. *Frontiers in Physics.* 2021;9:213.

83. Cramer A, Hecla J, Wu D, et al. Stationary Computed Tomography for Space and other Resource-constrained Environments. *Sci Rep.* 2018;8(1):14195.

84. Jorgensen JS, Sidky EY, Pan X. Quantifying admissible undersampling for sparsity-exploiting iterative image reconstruction in X-ray CT. *IEEE Trans Med Imaging.* 2013;32(2):460-473.

85. Zhang Z, Liang X, Dong X, Xie Y, Cao G. A sparse-view CT reconstruction method based on combination of DenseNet and deconvolution. *IEEE transactions on medical imaging.* 2018;37(6):1407-1417.

86. Kim H, Anirudh R, Mohan KA, Champley K. Extreme few-view ct reconstruction using deep inference. *arXiv preprint arXiv:191005375.* 2019.

87. Han Y, Kang J, Ye JC. Deep learning reconstruction for 9-view dual energy CT baggage scanner. *arXiv preprint arXiv:180101258.* 2018.

88. Moser S, Nau S, Salk M, Thoma K. In situ flash X-ray high-speed computed tomography for the quantitative analysis of highly dynamic processes. *Measurement Science and Technology.* 2014;25(2):025009.

89. Steven Tilley I, Zbijewski W, Stayman JW. High-Fidelity Modeling of Shift-Variant Focal-Spot Blur for High-Resolution CT. *Int'l Mtg Fully 3D Image Recon in Radiology and Nuc Med.*

90. Hernandez AM, Wu P, Mahesh M, Siewerdsen JH, Boone JM. Location and direction dependence in the 3D MTF for a high-resolution CT system. *Med Phys.* 2021;48(6):2760-2771.

91. Neculaes VB, Edic PM, Frontera M, Caiafa A, Wang G, De Man B. Multisource X-ray and CT: Lessons learned and future outlook. *IEEE Access.* 2014;2:1568-1585.

92. Becker AE, Hernandez AM, Boone JM, Schwoebel PR. A prototype Multi-X-ray-source array (MXA) for digital breast tomosynthesis. *Physics in Medicine & Biology.* 2020;65(23):235033.

93. Mobile computed tomography evaluation of the NeuroLogica CereTom. *Health Devices.* 2008;37(11):325-342.

94. Rosskopf J, Braun M, Beer M, Schmitz BL. Improving resolution of head and neck CTA using the small x-ray tube focal spot. *Neuroradiology.* 2019;61(8):953-956.

95. Oh LC, Lau KK, Devapalasundaram A, Buchan K, Kuganesan A, Huynh M. Efficacy of fine focal spot technique in CT angiography of neck. *Br J Radiol.* 2019;92(1100):20190083.

96. Li X, Zhang D, Liu B. A practical approach to estimate the weighted CT dose index over an infinite integration length. *Phys Med Biol.* 2011;56(18):5789-5803.

97. Tomic N, Papaconstadopoulos P, Aldelaijan S, Rajala J, Seuntjens J, Devic S. Image quality for radiotherapy CT simulators with different scanner bore size. *Phys Med.* 2018;45:65-71.

98. Van Daatselaar A, Van der Stelt P, Weenen J. Effect of number of projections on image quality of local CT. *Dentomaxillofacial Radiology.* 2004;33(6):361-369.

99. La Riviere PJ, Vargas P. Correction for resolution nonuniformities caused by anode angulation in computed tomography. *IEEE Trans Med Imaging.* 2008;27(9):1333-1341.

100. Braun H, Kyriakou Y, Kachelriess M, Kalender WA. The influence of the heel effect in cone-beam computed tomography: artifacts in standard and novel geometries and their correction. *Phys Med Biol.* 2010;55(19):6005-6021.

101. Oosterkamp W. Philips Res. *Rep.* 1948;3:303.

102. Calliste J, Wu G, Laganis PE, et al. Second generation stationary digital breast tomosynthesis system with faster scan time and wider angular span. *Med Phys.* 2017;44(9):4482-4495.

103. Feldkamp LA, Davis LC, Kress JW. Practical cone-beam algorithm. *Josa a.* 1984;1(6):612-619.

104. Quan EM, Lalush DS. Three-dimensional imaging properties of rotation-free square and hexagonal micro-CT systems. *IEEE transactions on medical imaging.* 2010;29(3):916-923.

105. Panetta D, Belcari N, Del Guerra A, Moehrs S. An optimization-based method for geometrical calibration in cone-beam CT without dedicated phantoms. *Phys Med Biol.* 2008;53(14):3841-3861.

106. Jiang R, Li G, Gu N, Chen G, Luo S. A wire scanning based method for geometric calibration of high resolution CT system. Paper presented at: Medical Imaging 2015: Physics of Medical Imaging2015.

107. Chen Z, Jin X, Li L, Wang G. A limited-angle CT reconstruction method based on anisotropic TV minimization. *Phys Med Biol.* 2013;58(7):2119-2141.

108. Ritschl L, Bergner F, Fleischmann C, Kachelriess M. Improved total variation-based CT image reconstruction applied to clinical data. *Phys Med Biol.* 2011;56(6):1545-1561.

109. Gong C, Zeng L, Guo Y, Wang C, Wang S. Multiple limited-angles computed tomography reconstruction based on multi-direction total variation minimization. *Rev Sci Instrum.* 2018;89(12):125121.

110. Geyer LL, Schoepf UJ, Meinel FG, et al. State of the Art: Iterative CT Reconstruction Techniques. *Radiology.* 2015;276(2):339-357.

111. van Aarle W, Palenstijn WJ, Cant J, et al. Fast and flexible X-ray tomography using the ASTRA toolbox. *Opt Express.* 2016;24(22):25129-25147.

112. Luo Y, Spronk D, Lee YZ, Zhou O, Lu J. Simulation on system configuration for stationary head CT using linear carbon nanotube x-ray source arrays. *Journal of Medical Imaging.* 2021;8(5):052114.

113. McCollough CH, Bruesewitz MR, McNitt-Gray MF, et al. The phantom portion of the American College of Radiology (ACR) computed tomography (CT) accreditation program: practical tips, artifact examples, and pitfalls to avoid. *Medical physics.* 2004;31(9):2423-2442.

114. Altunbas C, Park Y, Yu Z, Gopal A. A unified scatter rejection and correction method for cone beam computed tomography. *Med Phys.* 2021;48(3):1211-1225.

115. Baghani HR. Image quality parameters in brain imaging with fan-beam collimator: a Monte Carlo study on radiation scattering effects. *Radiol Phys Technol.* 2019;12(2):194-200.

116. Becker AE, Hernandez AM, Schwoebel PR, Boone JM. Cone beam CT multisource configurations: evaluating image quality, scatter, and dose using phantom imaging and Monte Carlo simulations. *Phys Med Biol.* 2020;65(23):235032.

117. Liang X, Jiang Y, Zhao W, et al. Scatter correction for a clinical cone-beam CT system using an optimized stationary beam blocker in a single scan. *Med Phys.* 2019;46(7):3165-3179.

118. Hunter AK, McDavid WD. Characterization and correction of cupping effect artefacts in cone beam CT. *Dentomaxillofac Radiol.* 2012;41(3):217-223.

119. Makins SR. Artifacts interfering with interpretation of cone beam computed tomography images. *Dent Clin North Am.* 2014;58(3):485-495.

120.   Adibhatla A. Latest developments in liquid metal jet technology x-ray sources. Paper presented at: Advances in X-Ray/EUV Optics and Components XVI2021.